UNIVERSITY OF SOUTHAMPTON

MICROWAVE SPECTROSCOPY OF NEAR-DISSOCIATION MOLECULAR IONS

Josephine Clare Pabari
(née Page) B.Sc. GRSC GradInstP

A thesis submitted for the degree of
Doctor of Philosophy

DEPARTMENT OF CHEMISTRY

February 2001

UNIVERSITY OF SOUTHAMPTON

ABSTRACT

FACULTY OF SCIENCE

CHEMISTRY

Doctor of Philosophy

MICROWAVE SPECTROSCOPY OF NEAR-DISSOCIATION MOLECULAR IONS

by Josephine Clare Pabari

Microwave spectroscopy has been used in conjunction with the technique of electric field dissociation to study the near-dissociation energy levels of two molecular ions: Ne_2^+ and Ar_2^+. The analyses of these spectra have provided a significant challenge for the methods of theoretical chemistry, and furthered the understanding of long-range intermolecular forces.

278 microwave transitions have been recorded in Ne_2^+ and 73 % of these have been assigned using a combination of double resonance experiments and Zeeman studies. Thus, an experimental energy level diagram of 102 levels has been formed, all of which lie within 10.3 cm^{-1} of the first dissociation limit and have values of $J \leq 21/2$.

From the measured g-factors, it may be concluded that the levels are best described by Hund's case (c) coupling at low J, but as J increases a transition to case (e) is observed. Coupled-channel calculations have been used to describe the experimentally observed energy levels and have also provided predictions for many of the remaining unassigned transitions.

69 transitions have been observed in Ar_2^+, and whilst nine connectivities have been confirmed, it has not been possible to utilise the Zeeman effect and so none of the transitions have been assigned with certainty. It is shown that it is highly probable that the Ar_2^+ ions have been formed by the breakdown of larger clusters, leading to high rotational temperatures and thus preventing resolved Zeeman spectra to be recorded. One Zeeman spectrum has been simulated and is assigned as $J = 27/2$ to $J = 29/2$.

Contents

Acknowledgements

Many thanks to:

My supervisor, Alan Carrington, who provided me with the opportunity at Southampton (and Peter Sarre for suggesting it) and many wonderful stories about his beloved cat Paddy! Also to the other members of the group, Andrew Shaw, Susie Taylor and David Gammie. In particular, to Susie and David – thanks for *all* the support, proof-reading and nagging! Many thanks also to the EPSRC for keeping my bank balance above water for three years.

The support staff in the Department, with a special mention to Jill and Sue for always providing a friendly safe-haven, Anita for the frequent use of a Bunsen burner, all the lads in the workshop for numerous O-rings and lots of muscle when I didn't have enough, and Anne for providing copious cups of coffee (even if it wasn't Nescafé!).

My many friends in the Department, with a special mention for Doctor Roo (not forgetting the orange hair of course!). To **PARADOCS** – well at least we tried! Also to Jeremy for always providing a happy smiling face (how's your wish list coming on?), and to George for all the support, especially when times got tough.

All my friends who have never failed to ask "how's the thesis?", to which I always replied "getting there". Well now it really has! To all those at work in Croydon – I can finally be sociable and come out with you in the evenings!

My greatest thanks go to all those who never lost faith (they know who they are) – I will never forget it. Just don't forget Manoj – it's your turn next!! (P.S. Can I go on holiday now please?!)

Chapter 1 - Introduction

1.1 Introduction

Spectroscopy is the experimental study of the absorption, emission or scattering of electromagnetic radiation by atoms or molecules. The many uses for this branch of physical science include determination of atomic and molecular structures, chemical analysis and identification of the composition of celestial bodies. All these avenues of study vary considerably in both the approach taken to glean results and, not surprisingly, the types of results obtained.

The work in this thesis is devoted to the high-resolution study of small molecular ions. The *majority* of this type of experimental spectroscopy is focussed on the region near a potential minimum and only when that region is fully understood do the studies develop to include areas of the potential away from equilibrium. Similarly, *ab initio* calculations tend to concentrate on equilibrium properties, often reporting only the details of a potential close to its minimum and rarely describing molecular properties near to the dissociation limit.

Whilst this approach is the traditional one and often the easiest to understand, it is not the only method. The work reported *here* approaches spectroscopy from a more unconventional direction: it starts at the dissociation limit and works down the potential well. In the pages that follow, it will be seen that this unusual method challenges many of the normal experimental assumptions.

Microwave spectroscopy is employed to study the structure of weakly bound molecular ions: experimental observations are confined to within *ca.* 10 cm^{-1} of a dissociation limit. Molecules in these energy states correspond to a nearly broken bond and therefore this region is most relevant to reaction dynamics and ion transport and solvation phenomena. Long-range molecules may also conceivably exist naturally, for example in interstellar gas clouds. Further, the information that is likely to be collected in the study of long-range molecules (such as precise dissociation energies and potential curves) is also of direct relevance in the development of excimer-type high power lasers.

In the majority of spectroscopic studies, the molecular vibrations and rotations may be described quite accurately by the Born-Oppenheimer approximation. However in the region close to a dissociation limit, the validity of the separation of nuclear and electronic motions, and even the conventional separation of nuclear motions into vibrational and rotational components must be questioned.

Microwave spectroscopy is usually concerned with the study of the rotational levels of molecules. However, the work presented here breaks this convention: as a result of anharmonicity, the spacings between vibrational levels near to the dissociation limit decrease and so vibrational transitions may occur at microwave frequencies. Further, when more than one electronic state corresponds to a particular dissociation limit, they will (by definition) be degenerate at dissociation (*i.e.* infinite internuclear distance). At large internuclear distances, transitions between such electronic states occur in the microwave region. Consequently, this work can be expected to involve electronic, vibrational or rotational transitions, or a combination of all three. Indeed, all of the transitions reported here are electronic in nature. It should be noted that the radiation used in this work is in the frequency range 6–170 GHz and should therefore be described as microwave and millimeter-wave radiation. However for convenience, this will be referred to as microwave radiation throughout this thesis.

There have been a number of spectroscopic investigations of high-lying vibrational levels, most of which concern neutral species. The most studied molecules are probably the alkali metal dimers. Stwalley and co-workers have carried out a number of studies of the "pure long-range" states in the homonuclear dimers Li_2 [1, 2], Na_2 [3, 4] and K_2 [5 - 7] using photoassociative spectroscopy, and similar experiments have been undertaken by Lett *et al.* [8]. Knöckel *et al.* [9] have identified vibrational levels covering 99.9997 % of the potential well of Na_2, the highest observed level lying only 0.025 cm^{-1} below dissociation. K_2 has been studied extensively by Amiot *et al.* [10] who observed vibrations up to $v = 81$, corresponding to an internuclear distance of 15.4 Å and to 99.96 % of the potential well depth. Of the heteronuclear alkali metal dimers, NaK appears to be the most extensively studied (for example refs. [11, 12]), and one of the more recent studies is that of Ishikawa *et al.* [13]. They used optical-optical double resonance spectroscopy to observe levels up to $v = 16$ of the $^3\Sigma^+$ state, calculated to be 2.8 cm^{-1} below dissociation. Other studies of heteronuclear alkali dimers include NaLi

[14] and RbCs [15] and there have also been some investigations of the related hydrides, LiH [16], KH [17] and CsH [18].

A second set of molecules that have been investigated near to dissociation are the diatomic halogens, in particular I_2 (for example refs. [19 - 22]). Ashmore *et al.* [21] also studied Cl_2, and Western *et al.* [23] studied the heteronuclear species ICl. Their results are expressed in an interesting and illustrative manner: they observed levels up to $v = 34$ in $I^{35}Cl$, which is "just below dissociation". This level has an amplitude greater than 3 Å and the probability that the internuclear separation is greater than the sum of the two van der Waals radii (3.73 Å) is 91 %.

The long-range atom-ion interaction has not been so fully investigated, partially due to the fact that the charge / induced-dipole interaction gives rise to a much higher density of near-dissociation levels than is found for comparable neutral species. Studies include those of Pilgrim *et al.* [24], who studied the $Mg^{+}\cdots Rg$ (Rg = Ar, Kr and Xe) complexes using photodissociation spectroscopy and those of Panov *et al.* [25] who studied $Ba^{+}\cdots Ar$.

However, by far the most extensive studies of molecular ions near dissociation are those using the technique of electric field dissociation (see Section 1.2.1). This method was first used in 1986 by Bjerre and Keiding [26] to investigate the long-range states of O_2^{+}, and subsequently used by Carrington and co-workers to investigate a number of long-range systems [27]. One of the first systems they studied was the simplest of all molecules, H_2^{+} [28, 29]. Despite many theoretical studies, there had only been one spectroscopic investigation of this ion previous to their investigation. However they obtained high resolution spectra that when compared with the theoretical studies of Moss [30] led to an agreement between experiment and theory of better than 3 MHz, thus fully characterising the long-range charge-induced-dipole states of this molecular ion. Carrington and co-workers performed similar successful experiments for $D\cdots D^{+}$ [31, 32], $H\cdots D^{+}$ [31] and $He\cdots He^{+}$ [33] and more recently, have successfully studied and characterised the more complex systems $He\cdots Ar^{+}$ [34] and $He\cdots Kr^{+}$ [35]. Other studies have included $He\cdots N^{+}$ [36, 37], $N\cdots N^{+}$ [37] and the triatomic system $He\cdots H_2^{+}$ [38], though the spectra obtained from these systems are not yet fully understood. This thesis provides the first publication of the fully characterised study of $Ne\cdots Ne^{+}$ (Chapter 4) and new results from the recent study of $Ar\cdots Ar^{+}$ (Chapter 5).

1.2 Experimental principles

As discussed in Section 1.1, the experiments described in this thesis cannot be described as "conventional" spectroscopy. It is therefore expected that some of the experimental principles essential for the understanding of these experiments are also rather unconventional. Two key experimental principles are discussed here: the first is the methods of populating near-dissociation states (Section 1.2.1) and the second is indirect methods of detection (Section 1.2.2). A full description of the experimental apparatus and methods is given in Chapter 3.

1.2.1 The population of near-dissociation states

There are several mechanisms by which near-dissociation energy levels of a molecular ion may be populated. For complexes containing helium, Carrington and co-workers [33 - 36, 38] used electron bombardment of ground-state He atoms to result not only in direct ionisation, but also in electronic excitation to a metastable triplet state, lying 19.818 eV above the ground state. These energetic He atoms can undergo associative ionisation, either with ground state He atoms (to form He_2^+ molecular ions) or with other substrates, such as Ar or H_2. The excess energy in the excited He atoms often leads to substantial population of the levels near to dissociation. This sequence may be represented as $He^*(2\,^3S) + X \rightarrow HeX^+ + e^-$. Alternatively, Penning ionisation may result: $He^*(2\,^3S) + X \rightarrow He + X^+ + e^-$.

This utilisation of helium as an energy sink in the ion source has not yet been successfully replicated using other atoms. A different mechanism is therefore required for studies of molecular ions not containing helium. The bonding in a neutral rare-gas van der Waals dimer is generally dominated by the r^{-6} dispersion interaction term, whereas the long-range part of the corresponding ionic potential is determined by the attractive r^{-4} charge-induced-dipole interaction, which is significantly stronger. Since the ion is therefore more strongly bound than the neutral, its potential curve is shifted to smaller internuclear distances. The Franck-Condon principle assumes that since nuclei move much more slowly than electrons, electron rearrangement occurs in a virtually static nuclear framework. Thus, the bond length is the same for both of the electronic states involved, and so the transition is 'vertical'.

This is illustrated in Figure 1.1, which shows the potential curve for the Ne-Ne van der Waals dimer [39], the potentials for the four electronic states of the Ne_2^+ ion which correlate with the lowest dissociation limit [40] and a vertical transition transferring population from the neutral to near-dissociation states in the ion.

The details of the Ne_2^+ and Ar_2^+ ionic potentials are discussed in Chapters 4 and 5 respectively; the main point here is that that vertical ionisation of the neutral will produce the ion with its highest vibration-rotation levels significantly populated. Franck-Condon factors for vertical ionisation of the Ar_2 neutral dimer to the high lying levels of the ion Ar_2^+ have been calculated using the program LEVEL [41]. Franck-Condon maps connecting the $J = 0$ vibrational levels of the neutral and the $J = 0$ vibrations of the four lowest states of the ion were then constructed. By integrating over a Boltzmann vibrational distribution for neutral Ar_2, the relative populations in the ion were obtained. Figure 1.2 (a) shows the probabilities of populating the vibrational levels of the four lowest states of Ar_2^+ via vertical ionisation of Ar_2 at 50 K. Figure 1.2 (b) shows greater detail of the probabilities of population for the levels 20 cm^{-1} below dissociation – the area of the potential in which the experiments in this work are carried out. It can be seen that whilst the majority of the population is expected to go to lower-lying energy levels, the levels of interest *do* have significant population, especially the I $(1/2)_u$ state. Similar results are expected for the vertical ionisation of Ne_2 to give Ne_2^+ [42] and this technique of populating the near-dissociation states has been verified by the discovery of near-dissociation microwave resonances in Ne_2^+ and Ar_2^+ [43]. The studies of the near-dissociation spectra of Ne_2^+ and Ar_2^+ prepared in this way are described in Chapters 4 and 5 respectively.

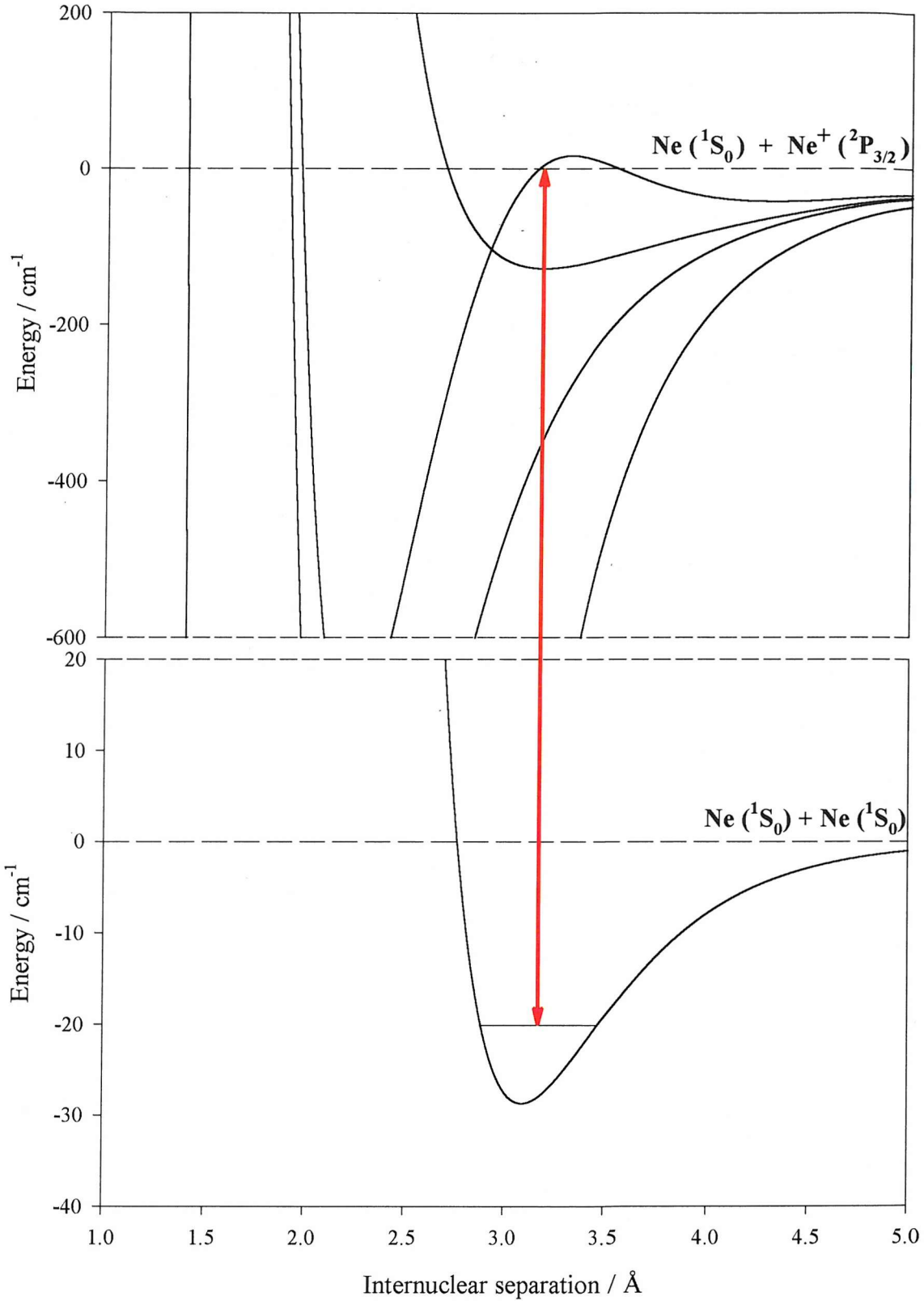

Figure 1.1: Potential energy curves illustrating the Franck-Condon electron impact ionisation of Ne_2 [39] to the four lowest-lying electronic states of Ne_2^+ [40]. Only the near-dissociation regions of the ionic states are shown.

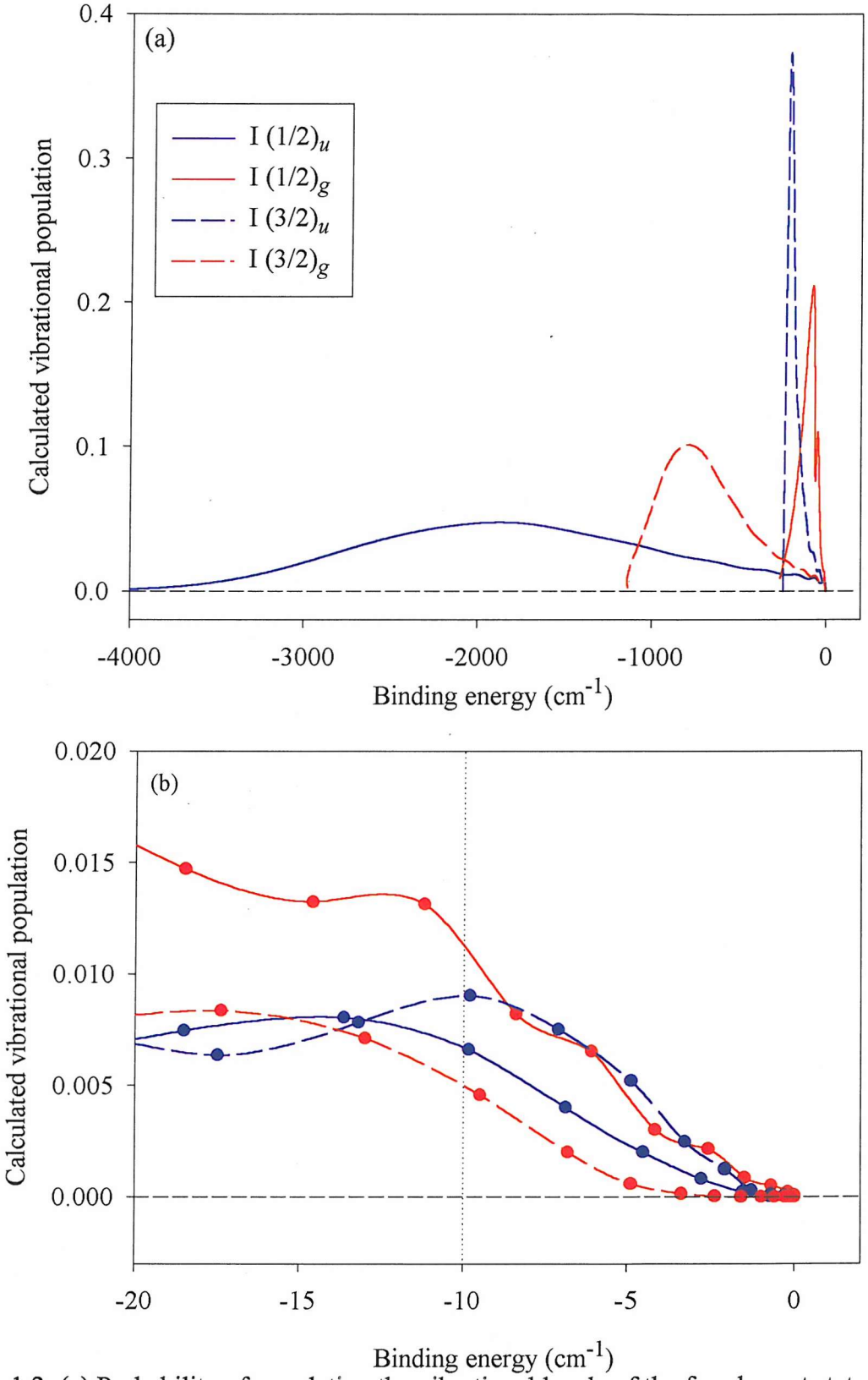

Figure 1.2: (a) Probability of populating the vibrational levels of the four lowest states of Ar_2^+ via vertical ionisation of Ar_2 at 50 K. (b) as (a), but showing greater detail of the region closest to dissociation.

1.2.2 Indirect detection of spectroscopic transitions

The parent ion beam fluxes achieved in this work are generally low: in the range 10^8 to 10^{10} ions s^{-1}, of which only 10^3 to 10^5 occupy the near-dissociation levels of interest. Even with the strongest ion beams available, it would be difficult to detect directly the absorption of electromagnetic radiation. Consequently, indirect detection methods are used, such that the absorption of photons results in population transfer and consequent changes in the number of detected ions, either parent or fragment. There are four main methods of indirect detection: charge exchange, photodissociation, predissociation and electric field dissociation, each of which will now be described.

Charge exchange

An ion such as HD^+ will undergo a charge-exchange reaction with other neutral molecules (*e.g.* H_2), and if the cross-section of the process depends significantly upon the vibrational state of the HD^+ ion, it may be used to detect population transfer arising from vibrational transitions. This method was used by Wing *et al.* [44] in their study of the $v = 1 \leftarrow 0$ vibration-rotation band of HD^+ and also by Carrington and Sarre [45] in their study of the electronic spectrum of the CO^+ ion. Although this experimental technique represented a significant step forward in the spectroscopic study of ion beams, its use is limited by poor sensitivity.

Photofragmentation

The monitoring of ion *fragments* that can be associated with a transfer of population offers a significantly more sensitive method for the detection of spectroscopic transitions. For example, Carrington *et al.* [46] were able to study the vibration-rotation spectrum of the HD^+ ion near its near-dissociation levels. They used a two-photon dissociation method in which the photofragment ions were detected, and population transfer induced by resonance with an IR carbon dioxide laser resulted in an increase in the photofragment ion current. Although this technique is much more sensitive than charge exchange, the background may still be quite large because the initial impact ionisation process populates all vibration-rotation levels of the ion, and all levels close enough to the dissociation continuum will yield photofragment ions.

Predissociation

Predissociation has been used in the majority of high-resolution ion-beam spectroscopic studies. Again, fragment ions are detected, but in this method they are formed when a transition occurs between a bound level lying below a dissociation limit and a quasibound transition level lying above it. High sensitivity is achieved if the quasibound level undergoes predissociation at an appropriate rate. The lifetime of the predissociating level is crucial to the success of this method: if it is too short the spectroscopic line will be too broad; if it is too long, predissociation will not occur in the appropriate part of the apparatus and fragments will not be detected. Despite these restrictions, predissociation has been used in many high-resolution ion-beam spectroscopic studies (for examples, see ref. [27]).

Electric field dissociation

This is perhaps the most sensitive indirect detection technique, and it is the method employed for the experiments presented in this thesis. In 1960 Hiskes [47] discussed the dissociation of diatomic molecules and molecular ions (with particular reference to H_2^+) by using electric fields. He showed, theoretically, that if an atomic or molecular system is placed in a steady electric field, the Coulomb binding forces are supplemented by an additional force that tends to separate the charges. In other words, it would be expected that a sufficiently intense electric field (*ca.* 100 $kVcm^{-1}$ for H_2^+) would lead to dissociation of the system. Experimental confirmation of Hiskes' prediction followed later the same year, when Riviere and Sweetman [48] demonstrated that the application of an electric field (of magnitude suggested by Hiskes) dissociated H_2^+ ions. Additionally, these experiments showed that as the magnitude of the electric field was increased, so the amount of dissociation also increased.

Hiskes also demonstrated theoretically that the application of an electric field along the internuclear axis perturbs the potential energy curves. It can be seen in Figure 1.3 that energy levels close to the dissociation limit may become quasibound or even unbound in the presence of the field. For the unbound case, dissociation of the ions populating that state is effected within one vibrational period, whilst quasibound states will predissociate with a lifetime dependent upon the field induced barrier width. If the field strength is increased smoothly from zero then vibration-rotation levels may be

successively dissociated, commencing with the uppermost states. This technique was used by Bjerre and Keiding [26] to study states of O_2^+. They provided the first direct determination of an ion-atom interaction potential at interatomic distances of 10-20 Å by means of electric field dissociation of selectively excited molecular ions. Transitions in O_2^+ were excited by a visible laser, and the upper of the levels involved in the transition were dissociated by an electric field and the fragment O^+ were detected.

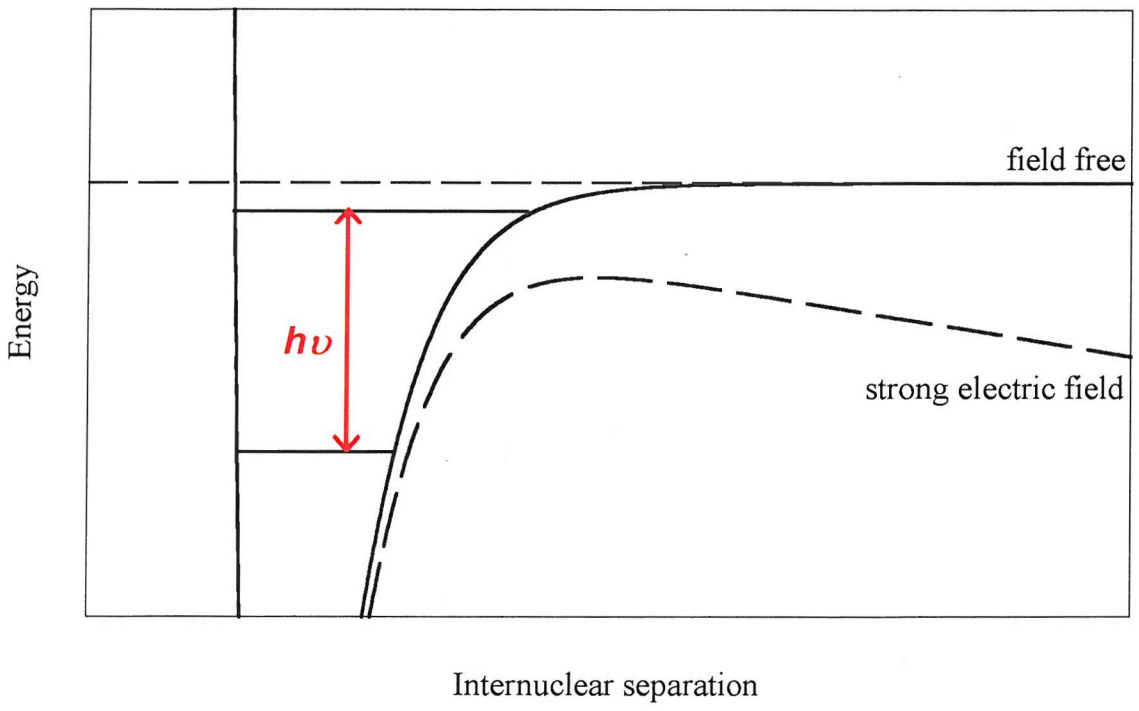

Figure 1.3: The effect of a strong electric field on a typical potential energy curve.

This work was brought to the attention of Carrington *et al.* [49] who then employed a similar technique to observe near-dissociation transitions in HD^+. Although this spectrum had been seen previously using a photodissociation technique, the electric field method resulted in a four orders-of-magnitude increase in sensitivity. As discussed in Section 1.1, Carrington and co-workers have since studied many molecular ions using the method of electric field dissociation.

Due to the design of the apparatus (Chapter 3) the fragment ions that result from the electric field dissociation process have characteristic kinetic energies that depend upon the energy of the level involved. Thus this indirect detection method has the advantage of state-selectivity, as well as a low non-resonant background. There is a restriction however: electric field dissociation can only be applied to energy levels lying very close to the dissociation limit (*i.e.* within *ca.* 10 cm^{-1}), but since this is the region of interest in this work this is not a hindrance.

1.3 Concluding remarks

The aim of the research described here is to observe and understand near-dissociation energy levels in small molecular ions, and thus characterise the long-range part of an atom-ion interaction potential. High-resolution microwave spectroscopy is employed to measure the spectra, and a combination of experimental and theoretical tools is used to fully characterise them.

Chapter 2 outlines the theory that is necessary for a full understanding of the work presented in this thesis, including the angular momentum coupling cases relevant to this work and an introduction to the Zeeman effect. A detailed description of the experimental apparatus and experimental techniques is given in Chapter 3. Chapter 4 presents the near-dissociation spectrum of Ne_2^+ and the first publication of the complete theoretical analysis of the observations. Over 275 transitions between near-dissociation levels have been recorded, and almost 75 % of these are experimentally assigned. Coupled-channel calculations guided the search for 17 of these levels (with a root-mean-squared error of 299 MHz) and assignments for a further 31 transitions are provided. The calculations have also provided accurate, experimentally determined potential curves.

Chapter 5 describes the results thus far obtained in a related study – that of the near-dissociation spectrum of Ar_2^+. Many spectral lines have been observed in this investigation, but it is found that experimental factors limit the analysis currently possible. The results are used, however, to estimate the temperature of the Ar_2^+ ions in the beam. Final conclusions and suggestions for further work are presented in Chapter 6.

Chapter 2 - Theory

2.1 Introduction

As would be expected with a study of this nature, much specialist theoretical knowledge is necessary for a full and thorough understanding. In order to provide one point of reference and to enable the experimental chapters to flow better for the reader, a number of the theoretical tools referenced in this thesis are brought together in this chapter.

The angular momentum coupling cases outlined in Section 2.2 are referenced throughout this work. The discussions of the Zeeman effect and rotational structure in homonuclear diatomics in Sections 2.3 and 2.4 respectively are useful mainly for a full understanding of Chapter 4.

2.2 Angular momentum coupling cases

Neglecting nuclear spin, there are three sources of angular momentum in diatomic molecules: **L**, the total orbital angular momentum of the electrons; **S**, the total electron spin angular momentum of the electrons; and **R**, the rotational angular momentum of the nuclei. The total angular momentum, the vector sum of these momenta, can be arrived at in a variety of different ways. Hund [50] devised four idealised angular momentum coupling schemes (cases (a), (b), (c) and (d)) which reflect the differing magnitudes of the various interactions between the angular momenta. These cases were discussed further by Mulliken [51] who introduced case (e) for completeness (which should not be confused with the Rydberg case (e) of Lefebvre-Brion [52]). The angular momentum coupling in a real molecule is rarely described by one of these pure, idealised cases: the true coupling is normally found to be between two of the ideal cases. The contamination of one of the pure Hund's cases by another is referred to as decoupling and such phenomena have been discussed very thoroughly by Herzberg [53].

Despite their limitations, the Hund's cases provide a useful starting point for the description of energy levels in diatomic molecules, and they will be referred to frequently throughout this thesis.

The dominant interaction for the near-dissociation states in this study is the coupling between the electronic spin and orbital angular momenta ("spin-orbit coupling"), and therefore a Hund's case (c) or case (e) is likely to be most appropriate. However, in the study of Ne_2^+ (Chapter 4), significant reference is made to Hund's case (a) and therefore this will also be described here.

2.2.1 Hund's case (a)

Hund's case (a) is appropriate when the electric field arising from the nuclei dominates the interactions in the molecule. This field couples the orbital angular momentum, **L**, to the internuclear axis with projection Λ. Because of the spin-orbit coupling, the spin angular momentum, **S**, is therefore also coupled to the internuclear axis, with projection Σ. The nuclear framework rotates with a momentum R that is represented by a vector **R** perpendicular to the axis. The total angular momentum of the molecule is denoted **J** and this has projection onto the internuclear axis Ω. This component is related to the components of orbital and spin angular momenta by $\Omega = \Lambda + \Sigma$. The set of quantum numbers appropriate for Hund's case (a) are therefore **L**, **S**, Λ, Σ, **J** and Ω. Hund's case (a) is shown in Figure 2.1 (a).

2.2.2 Hund's case (c)

As previously mentioned, Hund's case (c) occurs when the spin-orbit interaction dominates. The electron spin (**S**) and orbital (**L**) momenta couple to form an atomic-like total electronic angular momentum $\mathbf{J_a}$. The electrostatic coupling is sufficient for $\mathbf{J_a}$ to have a well-defined projection onto the internuclear axis, Ω. This then couples with the rotational angular momentum, **R**, to give the total angular momentum **J**. The quantum numbers used to describe Hund's case (c) are **L**, **S**, $\mathbf{J_a}$, **J** and Ω, and this case is shown in Figure 2.1 (b).

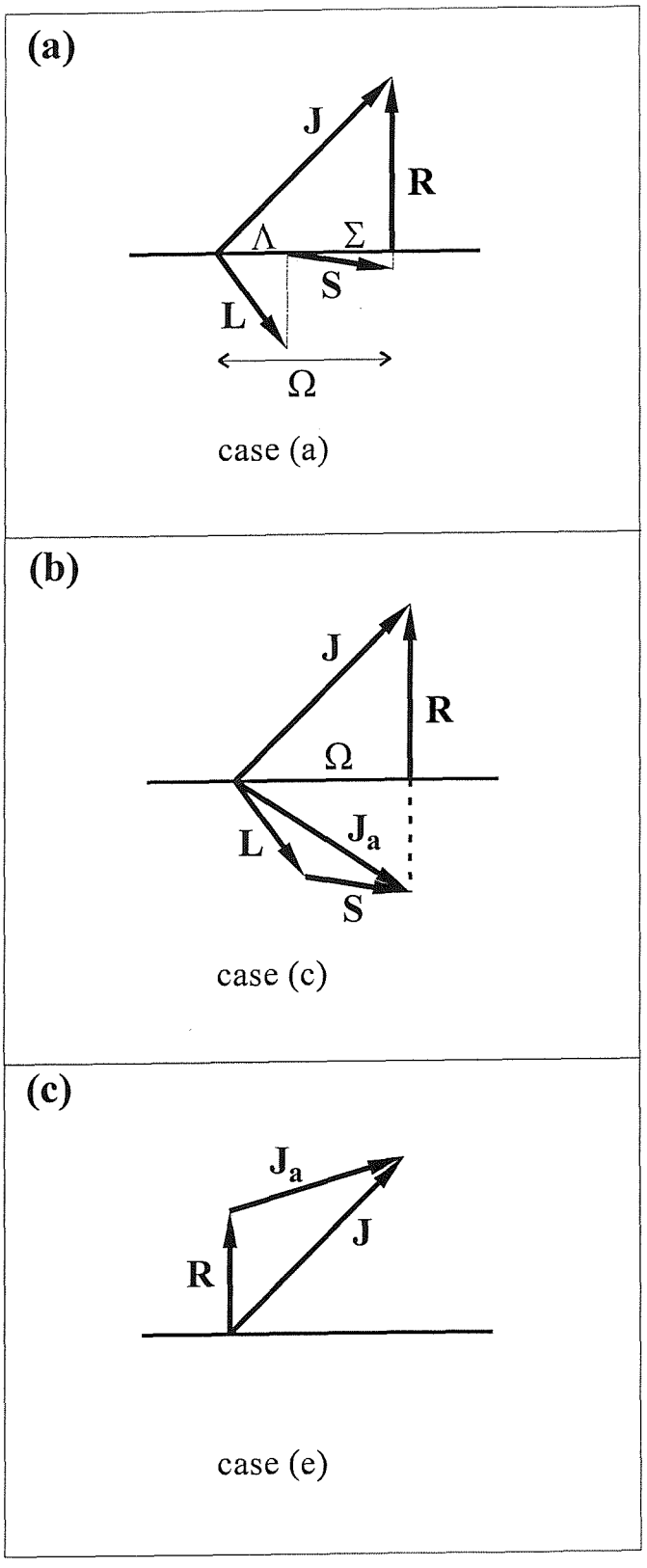

Figure 2.1: Angular momentum coupling diagrams for Hund's cases (a) and (c), and case (e).

2.2.3 case (e)

In case (e), the coupling due to the internuclear axis is *so* weak that it is not sufficient for $\mathbf{J_a}$ to have a well-defined projection on the molecular frame. Instead, $\mathbf{J_a}$ couples with the rotational angular momentum of the nuclear framework, **R**, to give the total angular momentum **J**. Case (e) is the simplest coupling case and is unique in that there are no projection quantum numbers: the quantum numbers used to describe case (e) are **L**, **S**, $\mathbf{J_a}$, **R** and **J**. This case represents the high-rotation limit of case (c), in which the coupling between rotational and electronic motions dominates, and the nuclear framework is moving so fast that the electrons are unable to follow the nuclear motions precisely, thereby invalidating the Born-Oppenheimer approximation. This case is very rarely observed; indeed the first report of this coupling case was in $He\cdots Kr^+$ by Carrington *et al.* [35] in 1996. Figure 2.1 (c) shows case (e) coupling.

2.3 Theory of the Zeeman effect

The Zeeman effect splits the magnetic sublevels of a state. Differing Zeeman effects between states results in observed splittings of spectral lines into several components. As will be discussed in Section 3.6.2, utilisation of the Zeeman effect is pertinent to the understanding of spectra obtained during this work, since analysis of such splittings often allows the determination of the J values and effective g-factors of both levels involved in a transition. Since the coupling cases most relevant to this study are cases (c) and (e), the Zeeman effect will be described in both of these cases.

The interaction of an external magnetic field (**B**) with the electron spin (**S**) and orbital (**L**) magnetic moments is represented by the Zeeman Hamiltonian, which consists of separate electron spin and orbital angular momentum terms,

$$\mathcal{H}_z = \mu_B T^1(\mathbf{B}) \cdot [g_e T^1(\mathbf{S}) + g_L T^1(\mathbf{L})], \qquad (2.1)$$

where μ_B is the electron Bohr magneton and g_e and g_L are the electron spin and orbital g-factors, with values 2.0023 and 1.000 respectively. The direction of the magnetic

field within the waveguide is defined to be the space-fixed $p = 0$ direction and so only this component of Equation 2.1 need be considered.

2.3.1 The Zeeman effect in Hund's case (c)

In Hund's case (c) the electron spin (**S**) and orbital (**L**) angular momenta are quantized in the molecular frame. To convert from the space-fixed frame to the molecule-fixed coordinate frame (q), the following transformation is used

$$T_p^{\mathrm{k}} = \sum_q D_{pq}^{\mathrm{k}*}(\omega) T_q^{\mathrm{k}}, \tag{2.2}$$

where $D_{pq}^{\mathrm{k}*}(\omega)$ represents a Wigner rotation matrix, and ω is the rotation necessary to convert from space-fixed to molecule-fixed coordinates. Equation 2.1 may therefore be rewritten

$$\mathcal{H}_{\mathrm{z}} = \mu_{\mathrm{B}} T_0^1(\mathbf{B}) \sum_q D_{0q}^{1*}(\omega)[g_{\mathrm{e}} T_q^1(\mathbf{S}) + g_{\mathrm{L}} T_q^1(\mathbf{L})]. \tag{2.3}$$

It is necessary to evaluate the matrix elements of $\mathcal{H}_{\mathrm{z}}$ within a case (c) basis, which are of the form

$$\langle \eta J_a J \Omega M_J | \mathcal{H}_{\mathrm{z}} | \eta' J_a' J' \Omega' M_J \rangle, \tag{2.4}$$

where η represents the electronic and vibrational wavefunctions. By substituting for $\mathcal{H}_{\mathrm{z}}$ in the matrix element (Equation 2.4) and factorising appropriately, one obtains

$$\begin{aligned} &\langle \eta J_a J \Omega M_J | \mathcal{H}_{\mathrm{z}} | \eta' J_a' J' \Omega' M_J \rangle = \\ &\quad \mu_{\mathrm{B}} B_0 \langle \eta | \eta' \rangle \sum_q \langle J \Omega M_J | D_{0q}^{1*}(\omega) | J' \Omega' M_J \rangle \\ &\quad \times \left[g_{\mathrm{e}} \langle L S J_a \Omega | T_q^1(\mathbf{S}) | L S J_a' \Omega' \rangle + g_{\mathrm{L}} \langle L S J_a \Omega | T_q^1(\mathbf{L}) | L S J_a' \Omega' \rangle \right], \end{aligned} \tag{2.5}$$

where $\langle \eta | \eta' \rangle$ is a vibrational overlap (Frank-Condon) integral. Equation 2.5 may be evaluated using standard spherical tensor operator algebra [54] to give matrix elements of the form

$$\begin{aligned}
&\langle \eta J_a J \Omega M_J | \mathcal{H}_z | \eta' J_a' J' \Omega' M_J \rangle = \qquad (2.6)\\
&\mu_B B_0 \langle \eta | \eta' \rangle \sum_q (-1)^{J_a+L+S-M_J+1} \left[(2J'+1)(2J+1)\right]^{1/2} \\
&\times \left[(2J_a'+1)(2J_a+1)\right]^{1/2} \begin{pmatrix} J & 1 & J' \\ -M_J & 0 & M_J \end{pmatrix} \begin{pmatrix} J & 1 & J' \\ -\Omega & q & \Omega' \end{pmatrix} \begin{pmatrix} J_a & 1 & J_a' \\ -\Omega & q & \Omega' \end{pmatrix} \\
&\times \left[g_e (-1)^{J_a} \left[S(S+1)(2S+1)\right]^{1/2} \begin{Bmatrix} S & J_a & L \\ J_a' & S & 1 \end{Bmatrix} + g_L (-1)^{J_a'} \left[L(L+1)(2L+1)\right]^{1/2} \begin{Bmatrix} L & J_a & S \\ J_a' & L & 1 \end{Bmatrix} \right].
\end{aligned}$$

To treat the Zeeman effect correctly in Hund's case (c) it is necessary to form eigenfunctions for the total parity operator $\hat{E}^*$. This is achieved by taking appropriate combinations of the primitive case (c) basis functions

$$|\eta J_a J | \Omega | \mathrm{p} \rangle = \frac{1}{\sqrt{2}} \left\{ |\eta J_a J + |\Omega| \rangle + \mathrm{p}(-1)^{J+L-J_a} |\eta J_a J - |\Omega| \rangle \right\}, \qquad (2.7)$$

where p = +1 corresponds to (+) total parity and p = -1 to (–) total parity. The required matrix element between these "parity-adapted" basis functions may be written in terms of the matrix elements involving primitive basis functions

$$\begin{aligned}
&\langle |\tfrac{1}{2}|, \mathrm{p} | \mathcal{H}_z | | \tfrac{1}{2} |, \mathrm{p} \rangle = \langle +\tfrac{1}{2} | \mathcal{H}_z | +\tfrac{1}{2} \rangle + \mathrm{p}(-1)^{J+L-J_a} \langle +\tfrac{1}{2} | \mathcal{H}_z | -\tfrac{1}{2} \rangle, \qquad (2.8)\\
&\langle |\tfrac{3}{2}|, \mathrm{p} | \mathcal{H}_z | | \tfrac{3}{2} |, \mathrm{p} \rangle = \langle +\tfrac{3}{2} | \mathcal{H}_z | +\tfrac{3}{2} \rangle, \\
&\langle |\tfrac{1}{2}|, \mathrm{p} | \mathcal{H}_z | | \tfrac{3}{2} |, \mathrm{p} \rangle = \langle +\tfrac{1}{2} | \mathcal{H}_z | +\tfrac{3}{2} \rangle.
\end{aligned}$$

To obtain pure case (c) effective g-factors it is necessary first to evaluate the matrix elements between the parity-adapted basis functions, using Equations 2.6 and 2.8 with $\eta = \eta'$, $J = J'$, $J_a = J_a'$, $|\Omega| = |\Omega'|$ and then divide by $\mu_B B_0 M_J$. For pure case (c) states the following simple results for the g-factors are obtained:

$$J_a = \frac{3}{2}, |\Omega| = \frac{1}{2}, \mathrm{p} \qquad g_{\mathrm{eff}} = \frac{(g_e + 2g_L)\left[1 + \mathrm{p}(-1)^{J-1/2}(4J+2)\right]}{12J(J+1)}, \tag{2.9}$$

$$J_a = \frac{3}{2}, |\Omega| = \frac{3}{2}, \mathrm{p} \qquad g_{\mathrm{eff}} = \frac{3(g_e + 2g_L)}{4J(J+1)},$$

$$J_a = \frac{1}{2}, |\Omega| = \frac{1}{2}, \mathrm{p} \qquad g_{\mathrm{eff}} = \frac{(4g_L - g_e)\left[1 + \mathrm{p}(-1)^{J+1/2}(2J+1)\right]}{12J(J+1)}.$$

The values obtained from these formulae have been evaluated for $J \leq 21/2$ and are shown in Table 2.1.

	$J_a = 3/2$			$J_a = 1/2$	
	$\|\Omega\|=1/2$		$\|\Omega\|=3/2$	$\|\Omega\|=1/2$	
J	g	u	g/u	g	u
1/2	2.224	-1.334	...	-0.222	0.666
3/2	-0.623	0.800	0.800	0.222	-0.133
5/2	0.496	-0.419	0.343	-0.095	0.133
7/2	-0.318	0.360	0.191	0.095	-0.074
9/2	0.283	-0.256	0.121	-0.061	0.074
11/2	-0.215	0.233	0.084	0.061	-0.051
13/2	0.198	-0.185	0.062	-0.044	0.051
15/2	-0.162	0.173	0.047	0.044	-0.039
17/2	0.153	-0.145	0.037	-0.035	0.039
19/2	-0.130	0.137	0.030	0.035	-0.032
21/2	0.124	-0.119	0.025	-0.029	0.032

Table 2.1: Limiting g-factors for pure Hund's case (c).

2.3.2 The Zeeman effect in case (e)

Since the electron spin and orbital angular momenta are defined in the space frame for case (e) the evaluation of the matrix elements of the Zeeman Hamiltonian is considerably simpler than for Hund's case (c).

The matrix elements of the Zeeman Hamiltonian (Equation 2.2), again setting $p = 0$, are given by

$$\left\langle \eta R J_a J M_J \middle| \mu_B T^1_0(\mathbf{B}) \left[g_e T^1_0(\mathbf{S}) + g_L T^1_0(\mathbf{L}) \right] \middle| \eta' R J_a' J' M_J \right\rangle = \tag{2.10}$$

$$\mu_B B_0 \langle \eta | \eta' \rangle (-1)^{2J+J_a'+R+L+S-M_J} \left[(2J'+1)(2J+1) \right]^{1/2} \left[(2J_a'+1)(2J_a+1) \right]^{1/2}$$

$$\times \begin{pmatrix} J & 1 & J' \\ -M_J & 0 & M_J \end{pmatrix} \begin{Bmatrix} J_a & J & R \\ J' & J_a' & 1 \end{Bmatrix} \left[g_e (-1)^{J_a} \left[S(S+1)(2S+1) \right]^{1/2} \begin{Bmatrix} S & J_a & L \\ J_a' & S & 1 \end{Bmatrix} \right.$$

$$\left. + g_L (-1)^{J_a'} \left[L(L+1)(2L+1) \right]^{1/2} \begin{Bmatrix} L & J_a & S \\ J_a' & L & 1 \end{Bmatrix} \right].$$

Again, the pure case (e) effective g-factors are obtained by evaluating Equation 2.10 with $\eta = \eta'$, $J = J'$ and $J_a = J_a'$ and then dividing by $\mu_B B_0 M_J$,

$$J_a = \frac{3}{2} \quad g_{\text{eff}} = \frac{(g_e + 2g_L)\left[J(J+1) - R(R+1) + \frac{15}{4} \right]}{6J(J+1)}, \tag{2.11}$$

$$J_a = \frac{1}{2} \quad g_{\text{eff}} = \frac{(4g_L - g_e)\left[J(J+1) - R(R+1) + \frac{3}{4} \right]}{6J(J+1)}.$$

These expressions have been evaluated for $J \leq 21/2$ and are presented in Table 2.2. Note that the limiting g-factors for the $J_a = 1/2$ dissociation limit are the same, irrespective of whether the coupling case is Hund's case (c) or case (e) due to lack of Ω-mixing.

	$J_a = 3/2$				$J_a = 1/2$	
J	R	g	R	u	g	u
1/2	1	2.224	2	-1.334	-0.222	0.666
3/2	1	0.978	0	1.334	0.222	-0.133
	3	-0.800	2	0.267		
5/2	1	0.800	2	0.496	-0.095	0.133
	3	0.038	4	-0.572		
7/2	3	0.318	2	0.572	0.095	-0.074
	5	-0.445	4	-0.021		
9/2	3	0.445	4	0.229	-0.061	0.074
	5	-0.040	6	-0.364		
11/2	5	0.177	4	0.364	0.061	-0.051
	7	-0.308	6	-0.047		
13/2	5	0.308	6	0.144	-0.044	0.051
	7	-0.048	8	-0.267		
15/2	7	0.120	6	0.267	0.044	-0.039
	9	-0.235	8	-0.047		
17/2	7	0.235	8	0.103	-0.035	0.039
	9	-0.045	10	-0.211		
19/2	9	0.090	8	0.211	0.035	-0.032
	11	-0.191	10	-0.043		
21/2	9	0.191	10	0.080	-0.029	0.032
	11	-0.041	12	-0.174		

Table 2.2: Limiting g-factors for pure case (e).

2.4 Rotational structure in homonuclear diatomic molecules

The success of the experimental work in this study relies heavily on a thorough understanding of the theoretical patterns of rotational energy levels expected in the molecules under investigation. Such an understanding is imperative, in order both to analyse preliminary results and to provide guidance whilst searching for new energy levels later in the study. A detailed explanation of the rotational structure expected for $^{20}Ne_2^+$ is now given, although the discussion applies equally to $^{40}Ar_2^+$.

2.4.1 Symmetry effects of nuclear spin statistics

The Pauli principle requires that the total wavefunction including nuclear spin must be symmetric with respect to interchange of two identical nuclei for bosons and antisymmetric for fermions. The permutation operator $\hat{P}_{12}$ denotes this interchange and since ^{20}Ne is a boson (nuclear spin $I = 0$), then the total wavefunction (Ψ_{total}) stays the same on permutation of the two identical nuclei, *i.e.*

$$\hat{P}_{12}\Psi_{\text{total}} = +\Psi_{\text{total}}. \tag{2.12}$$

The nuclear spin wavefunction can be factored from the total wavefunction, thus

$$\Psi_{\text{total}} = \Psi_{\text{nuc}}\Psi_{\text{evr}}, \tag{2.13}$$

where Ψ_{nuc} is the nuclear spin wavefunction and Ψ_{evr} represents the remainder of the wavefunction (rovibronic). Since $I = 0$, Ψ_{nuc} is symmetric with respect to the permutation $\hat{P}_{12}$ and therefore to satisfy Equation 2.12 it is required that Ψ_{evr} is also symmetric with respect to $\hat{P}_{12}$ (*i.e. s* symmetry),

$$\hat{P}_{12}\Psi_{\text{evr}} = +\Psi_{\text{evr}}. \tag{2.14}$$

It may be shown that [55]

$$\hat{P}_{12}\,\Psi_{\text{evr}} \equiv \hat{\imath}\,\hat{E}^{*}\,\Psi_{\text{evr}}\,, \tag{2.15}$$

where $\hat{\imath}$ is the electron inversion operator (this has eigenvalues with labels g and u and applies only to *homonuclear* diatomics since it inverts through the centre of symmetry) and $\hat{E}^{*}$ is the total parity operator which inverts the coordinates of both the nuclei and electrons through the centre of mass (has eigenvlaues with labels + and –). The rovibronic wavefunction Ψ_{evr} is classified as follows

$$\hat{\imath}\,\Psi_{\text{evr}} = +\,\Psi_{\text{evr}} \text{ for } g \text{ states} \tag{2.16}$$
$$\hat{\imath}\,\Psi_{\text{evr}} = -\,\Psi_{\text{evr}} \text{ for } u \text{ states}$$

and

$$\hat{E}^{*}\Psi_{\text{evr}} = +\Psi_{\text{evr}} \text{ for (+) parity states} \tag{2.17}$$
$$\hat{E}^{*}\Psi_{\text{evr}} = -\Psi_{\text{evr}} \text{ for (–) parity states.}$$

Consequently, to satisfy Equation 2.14, the rovibronic wavefunction Ψ_{evr} must have either g symmetry and (+) total parity, or u symmetry and (–) total parity. The combinations g with (–) and u with (+) are of antisymmetric symmetry, a, and so for $^{20}Ne_2^{+}$ these levels do not exist and thus half of the rotational levels are "missing" from each electronic state.

2.4.2 Rotational Hamiltonian in Hund's case (c)

The rotational Hamiltonian may be written as

$$\mathcal{H}_{\text{R}} = \frac{\hbar^2}{2\mu r^2}\mathbf{R}^2\,, \tag{2.18}$$

where μ is the reduced mass and r is the internuclear separation. $\mathbf{R}$ is the rotation of the nuclear framework and $\mathbf{R}^2$ may be rewritten (in case (c))

$$\mathbf{R}^2 = (\mathbf{J}^2 + \mathbf{J}_a^2 - 2\mathbf{J}\cdot\mathbf{J}_a). \tag{2.19}$$

Thus Equation 2.18 becomes

$$\mathcal{H}_R = B_v(\mathbf{J}^2 + \mathbf{J}_a^2 - 2\mathbf{J}\cdot\mathbf{J}_a), \tag{2.20}$$

where the term of particular interest, $-2B_v\mathbf{J}\cdot\mathbf{J}_a$, represents a coupling between the electronic and rotational motions ("rotational-electronic coupling"). This then breaks the Born-Oppenheimer approximation since it mixes electronic states with a difference in Ω of unity (*e.g.* Ω = 1/2 and 3/2). It is also responsible for a transition from Hund's case (c) towards case (e), a point that will be discussed in detail in Section 4.3.1.

The matrix elements of the operator $-2B_v\mathbf{J}\cdot\mathbf{J}_a$ are of the form [56]

$$\langle qv\Omega J|-2B\mathbf{J}\cdot\mathbf{J}_a|q'v'\Omega-1J\rangle = -P(B)[(J+\Omega)(J-\Omega+1)]^{1/2}, \tag{2.21}$$

with $P(B)$ defined by

$$P(B) = B[(J_a+\Omega)(J_a-\Omega+1)]^{1/2} \tag{2.22}$$

in an idealised case for which $\mathbf{J}_a^2$ can be ascribed the quantised value $J_a(J_a+1)$. The energies can then be obtained, and are

$$\begin{aligned}
\langle \tfrac{1}{2}|\mathcal{H}|\tfrac{1}{2}\rangle &= T_{1/2} + B_{1/2}\left[J(J+1)-\tfrac{1}{2}\right] - p(-1)^{J-1/2}P(J+\tfrac{1}{2}) \\
\langle \tfrac{3}{2}|\mathcal{H}|\tfrac{3}{2}\rangle &= T_{3/2} + B_{3/2}\left[J(J+1)-\tfrac{9}{2}\right] \\
\langle \tfrac{1}{2}|\mathcal{H}|\tfrac{3}{2}\rangle &= -Q\left[(J-\tfrac{1}{2})(J+\tfrac{3}{2})\right]^{1/2},
\end{aligned} \tag{2.23}$$

where $T_{1/2}$ and $T_{3/2}$ represent the electronic and vibrational energy term values, Q is a parameter which allows for mixing between Ω = 1/2 and Ω = 3/2 states and P allows for an effect known as "Ω-doubling", which will now be described.

The term $p(-1)^{J-1/2} P(J+\frac{1}{2})$ in Equation 2.23 is responsible for the removal of the degeneracy for $\Omega = 1/2$ states of different total parity, *i.e.* the J dependence of the phase factor $p(-1)^{J-1/2}$ will cause alternate positive and negative P contributions to the energies of levels within a given electronic state. This pattern will be especially noticeable since half the levels will be "missing" (Section 2.4.1). The dependence of the phase factor on the total parity (p) predicts that in the g states, the $|\Omega| = 1/2$, $J = 3/2$ level will be less strongly bound than the $|\Omega| = 1/2$, $J = 1/2$ level, whereas the opposite will be true for the u states. The form of the $|\Omega| = 3/2$ states (Equation 2.23) is much simpler and thus these states will not exhibit this Ω-doubling effect, except as a result of mixing with $|\Omega| = 1/2$ states. It will be seen in Section 4.3 that these patterns are clearly observed in the near-dissociation states of Ne_2^+.

2.5 Concluding Remarks

Although not exhaustive, this Chapter outlines some of the key theoretical tools required for an understanding of the work presented in this thesis. The angular momentum coupling cases, in particular cases (c) and (e) are used throughout this work. The Zeeman effect is utilised in both Chapters 4 and 5, though due to experimental restrictions (as will be discussed in the relevant places) the use in each of these Chapters is remarkably different.

Chapter 3 - Experimental apparatus and techniques

3.1 Introduction

The ion beam apparatus used in this work is a modified Vacuum Generators ZAB 1F reverse-geometry tandem mass spectrometer, the main features of which are shown in Figure 3.1. Positively charged ions are generated in an electron impact source (Section 3.2), accelerated to a large positive potential (typically 3–8 kV) and the resulting ion beam is mass-to-charge analysed by means of a magnetic sector (55 °, 0.30 m radius). The chosen beam then enters the microwave interaction region (Section 3.3) which consists of a length of rectangular copper waveguide (0.40 m) encased in a solenoid coil which enables the application of an external magnetic field for use in studies of the Zeeman effect.

The ion beam then enters the electric field lens (Section 3.4), where electric fields of up to 20 $kVcm^{-1}$ result in the fragmentation of molecules populated in near-dissociation energy levels. The fragment ions produced have characteristic kinetic energies and are energy-analysed by means of an electrostatic sector (81.5 °, 0.38 m radius). The ions are normally detected with an off-axis electron multiplier, although accurate measurements of the parent ion beam current may be made with a Faraday cup. Focusing and deflection plates that are located immediately after the source and between the waveguide and electric field lens expedite accurate focusing of the ion beam. When the frequency of the microwave photon is resonant with a transition in the molecule, the resulting population change between near-dissociation energy levels is detected indirectly as a change in the electric field induced fragment ion current.

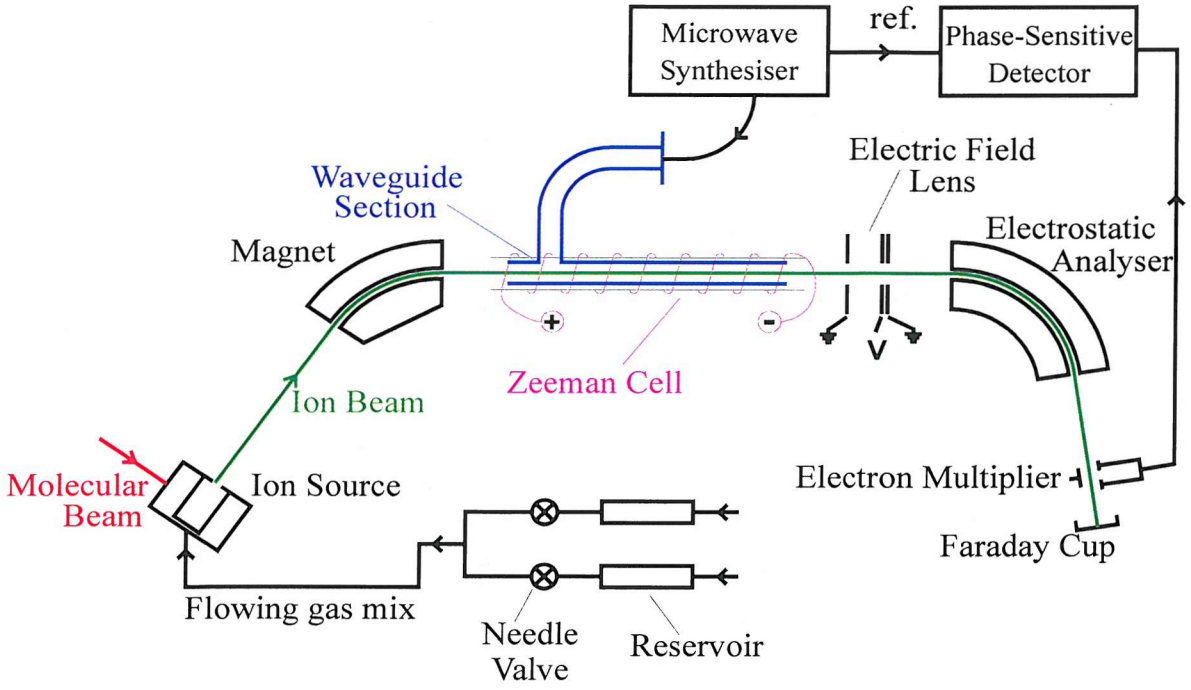

Figure 3.1: Schematic diagram of the apparatus.

3.2 The molecular beam chamber and ion source

As discussed in Section 1.2.1, Carrington and co-workers have utilised two methods of forming molecular ion beams with significant population in levels near to dissociation. The molecular ions discussed in this thesis (Ne_2^+ and Ar_2^+), are produced via electron impact ionisation of neutral van der Waal molecules. This method will now be described.

Pure neon or pure argon gas is passed through a nozzle and expanded through a small aperture to form a supersonic molecular beam. For the Ne_2^+ study, the neon is at a backing pressure of 10 bar, but for the Ar_2^+ study the backing pressure of the argon is limited to 3.5 bar. This is because (as will be discussed in Section 5.3.1) argon has a high tendency to cluster, and at pressures higher than 3.5 bar it is found to condense in the apparatus and thus the diffusion pumps are unable to work efficiently.

The effects of changing nozzle aperture size (10–70 μm) were investigated for the study of both Ne_2^+ and Ar_2^+. In the case of Ne_2^+ it was found that the larger

apertures provided increased Ne_2^+ beam currents, at the expense of rapid gas consumption, but with no significant increase in transition signal-to-noise ratios. An aperture of 20 μm was found to provide the best balance between these factors and so was employed throughout the study. For the same reasons, the majority of the Ar_2^+ work was also carried out using a 20 μm aperture. However, it was found that not all transitions were observable with this aperture in place and so a significant amount of work was therefore also carried out using aperture sizes of 10 μm and 50 μm.

The nozzle is mounted on a manipulator to permit fine adjustment of its position with respect to the skimmer and the ion source. It is possible to cool the nozzle with either liquid nitrogen or solid carbon dioxide, but since neither was found to have a detectable effect on a sample set of transitions the nozzle was operated at room temperature.

The isentropic region of the expansion is sampled by a skimmer positioned 10–20 mm from the nozzle and the molecular beam passes through it into the differentially pumped ion source chamber. The entrance to the ion source is approximately 20 mm from the exit of the skimmer; this is as close as possible to maximise the molecular beam intensity. Typical pressures in the nozzle chamber are 7×10^{-5} mbar for Ne_2^+ and 4×10^{-4} mbar for Ar_2^+. The pressure in the ionisation chamber is $< 10^{-6}$ mbar for both systems, giving a reasonable degree of differential pumping and a relatively collision-free environment.

The ion source has a hole (10 mm) drilled in the source block, through which the molecular beam can enter (Figure 3.2). Electrons are emitted from a heated tungsten or thoriated iridium filament perpendicular to the molecular beam and accelerated to energies in the range 50–150 eV. Electron impact ionisation results in the formation of molecular ions which are accelerated to a large positive potential (normally 6 kV) to form an ion beam. The electric field gradient used to extract ions from the source will depopulate near-dissociation levels in the same manner as the electric field lens ("stripping"), so a reduced source potential of 3 kV is used for the study of extremely weakly bound levels.

As discussed in Section 1.2.1, there is a second method of populating molecular ions in states near dissociation, a method used by Carrington and co-workers for the majority of their studies to date. This method utilises the excess

energy stored in excited helium atoms and uses a slightly different source to that described above.

In the 'flowing gas' ion source (which has not been utilised for the work described in this thesis but none-the-less provides an interesting comparison), a mixture of gases flows through a glass capillary (inside diameter 0.2 mm) and into an enclosed source block where it undergoes bombardment by electrons. The pressure inside this source block cannot be measured directly, but it is expected to be *ca.* 2 orders of magnitude higher than the surrounding source pressure (typically 10^{-4} mbar for HeH_2^+, for example). For the ion beam to have a suitable population distribution the total pressure and mixing ratio of the gases must be correct. The gases for mixing (*e.g.* H_2 and He) are therefore stored in separate reservoirs, each fed continuously from a cylinder. The amount of each gas and hence the mixing ratio and total pressure is controlled by needle valves attached to each reservoir. The correct conditions are determined by monitoring the fragment current arising from electric field dissociation and adjusting the valves to maximise this.

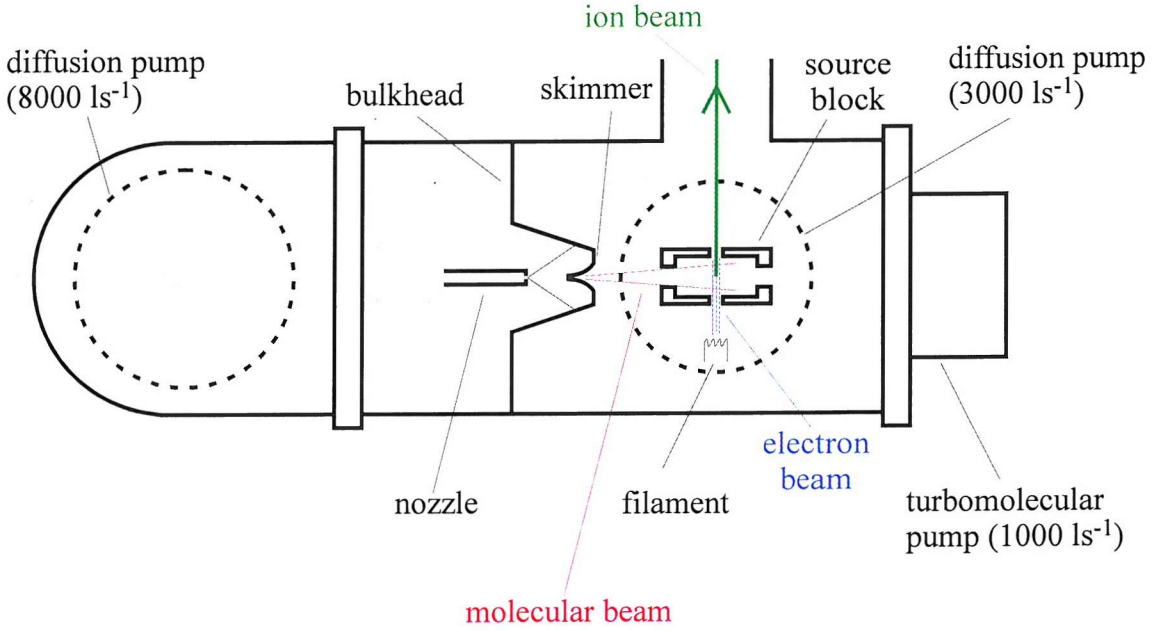

Figure 3.2: Schematic diagram of the molecular beam system.

3.3 Microwave methods

The primary sources of microwave radiation are two Wiltron frequency synthesisers, models 6753B-10 (2–26.5 GHz) and 6769B (0.01–40 GHz). Amplification in the region 2–40 GHz is made possible by using Hewlett Packard amplifiers; it is also possible to attenuate the power. A range of passive and active Millitech frequency multipliers allow the generation of frequencies up to 170 GHz. The specifications for this microwave equipment are summarised in Table 3.1.

The microwave radiation is introduced into a length of open-ended rectangular waveguide (0.40 m) by means of a simple E-plane T-piece situated close to the entry position of the ion beam (Figure 3.1). For an electromagnetic wave to propagate within the waveguide, it must have either a magnetic or an electric field component in the direction of propagation (z). A wave with a component of the magnetic field in the direction of propagation and its electric field in a plane perpendicular to this (x, y) is described as a transverse electric (TE) wave. Transverse magnetic (TM) waves have a component of the electric field in the direction of propagation and the magnetic field perpendicular to this.

Component	Model	Power output / mW	Frequency range / GHz
Synthesiser	6753B-10	≤ 40	2.0–26.5
Synthesiser	6769B	≤ 40	0.01–40.0
Amplifier	HP8349B	> 100	2.0–20.0
Amplifier	HP8348A	> 300	2.0–26.5
Amplifier	HP8346A	> 300	26.5–40.0
Doubler	MUD-28-4	≤ 4.0	22.0–42.0
Doubler	MUD-22-4	≤ 2.0	27.0–54.0
Doubler	MUD-15-40	≤ 1.5	50.0–75.0
Tripler	MUT-10-4	≤ 1.0	75.0–110.0
Sextupler	FEX-06-3-125-3	≤ 1.5	110.0–140.0
Sextupler	FEX-06-3-155-4	≤ 1.3	140.0–170.0

Table 3.1: Microwave equipment used.

For a wave to propagate, it must have an integral number of half-wave lengths in each transverse direction (x, y). These different field configurations are denoted by TE_{mn} or TM_{mn}, where m and n are the number of half-wave variations in the x- and y-direction respectively. The waveguide behaves like a high-pass filter and so each mode has a cutoff frequency, below which waves cannot propagate. Therefore there will be an optimum frequency range over which a single, dominant mode (TE_{10}) propagates; above this multiple modes will be present.

Each mode propagates at a different phase-velocity (although TE_{mn} and $TM_{m'n'}$ have identical velocities if $m = m'$ and $n = n'$) and as a consequence of the high velocity of the ion beam there is a characteristic Doppler shift associated with each mode. Additionally, radiation is reflected from the open ends of the waveguide, resulting in microwave propagation both parallel and antiparallel to the direction of the ion beam. Consequently, at frequencies where more than one mode can propagate, a single resonance may be split into several components, corresponding to

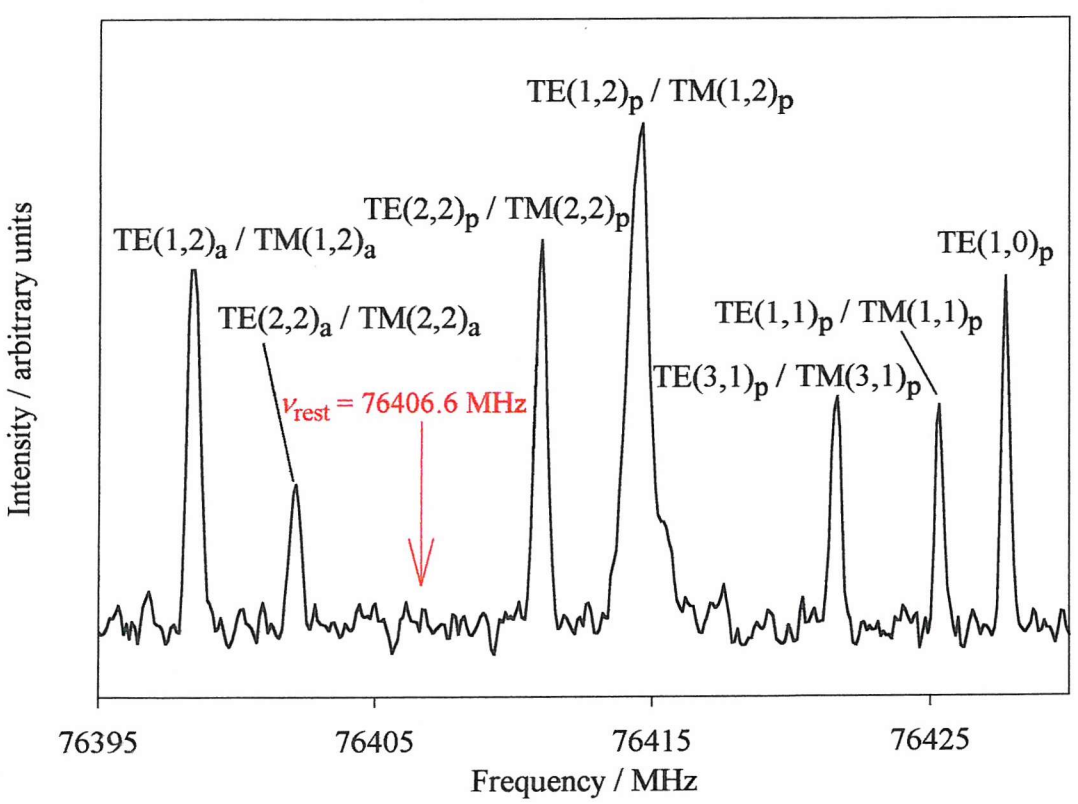

Figure 3.3: Recording of the 76406.6 MHz transition in Ar_2^+ showing multiple modes propagating parallel (p) and antiparallel (a) with respect to the ion beam.

the parallel and antiparallel propagation of multimodes. These patterns are easily understood from standard microwave theory [57] and so may be used to determine accurate rest frequencies. A typical mode pattern is shown in Figure 3.3. It can be seen from Figure 3.3 that the microwave power is not distributed evenly amongst the different modes (indeed certain microwave modes are never observed). Furthermore the physical arrangement of the waveguide with respect to the beam results in significantly more microwave power in the parallel branch (shifted to high frequency) than in the antiparallel branch (shifted to low frequency). If high levels of microwave power are employed, transitions are broadened and ultimately show Rabi oscillations [58].

Whilst it would be possible to ensure that only a single mode (TE_{10}) propagates by using waveguide appropriate to the frequency range being studied, this would require the use of waveguide with decreasing cross-section as the frequency increased. For frequencies above 40 GHz, the small cross-section of the required waveguide would result in unacceptable attenuation of the ion beam and therefore experiments are performed only with the waveguides listed in Table 3.2. The beam attenuation when using WR-28 is approximately 50 % and consequently WR-42 is used for the majority of scanning. Transitions above 26.5 GHz are therefore usually observed with multiple modes which often proves advantageous since each mode that is observed is, in effect, a measurement from which the rest frequency can be determined. There are, however, occasions when the presence of multiple modes complicates the determination of rest frequencies, *e.g.* a transition displaying hyperfine effects. In such cases an ambiguous mode assignment may be clarified by adjusting the source potential and observing the resulting changes in Doppler shifts.

Waveguide designation	**Optimal range for TE_{10} mode / GHz**	**Low frequency cutoff / GHz**	**Inside dimensions ($x \times y$) / mm**
WR-90	8.20–12.40	6.56	22.860 × 10.160
WR-42	18.00–26.50	14.10	10.668 × 4.318
WR-28	26.50–40.00	21.10	7.112 × 3.556

Table 3.2: Microwave waveguides used in this work.

An extremely important technique for establishing transition connectivities is microwave-microwave double resonance, which involves launching microwaves of two different frequencies into the waveguide simultaneously. This technique is described in detail in Section 3.6.1.

The Zeeman effect has also been used extensively in this work. The discussion here is limited to the details of the apparatus; more details of the experimental technique are described in Section 3.6.1 and a full theoretical treatment was given in Section 2.3. The waveguide is encased in a Teflon® cylinder (0.45 m long, 35 mm diameter), which forms the mount for a solenoid coil wound of insulated copper wire. Passing a current through the coil produces a homogeneous magnetic field collinear with the ion beam; end-effects are reduced by extending the coil past the ends of the waveguide. The maximum magnetic field currently available is 44 G (4.4×10^{-3} T), produced by applying a current of 4.0 A. Applying a current greater than this will heat the plastic casing, resulting in significant outgassing and disruption of the vacuum in the spectrometer. Attempts have been made previously to increase the maximum applicable field by constructing a triple-wound solenoid around a half-length of waveguide, but results from this were disappointing. In principle it would be possible to replace the Teflon® cylinder with a metal tube, thus avoiding the problem of heating effects. This would mean, however, that the waveguide assembly would require significant modification to support the additional weight and problems of insulation would be introduced.

3.4 Electric field lens

The electric field dissociation lens consists of three plates separated by ceramic spacers. Each plate has an aperture (2×5 mm) to allow for transmission of the ion beam. The first and last plates are kept at earth potential and a positive potential (up to 4.5 kV) is applied to the central plate. This second plate is located 10 mm from the first plate and 1 mm from the third plate, resulting in a large electric field gradient between the second and third plates (up to 20 $kVcm^{-1}$) [59].

The electric field lens induces fragmentation of parent ions to produce fragment ions with a range of kinetic energies. A typical fragment energy analysis is

shown in Figure 3.4; as well as the electric field peak, also shown is the "earth" fragment peak, which arises from spontaneous and collision-induced dissociation processes occurring outside the electric field lens. Whilst, in principle, it would be possible to monitor the dissociation of a particular level by careful choice of electric field strength and electrostatic analyser (ESA) voltage, the energies of the fragment ions are not separated sufficiently well to provide this selectivity. Consequently, by monitoring the top of the electric field dissociation peak, it is possible to detect fragments arising from most energy levels. It should be noted that whilst full state-selectivity cannot be achieved, it is often possible to find the optimum experimental conditions for detection of a particular transition.

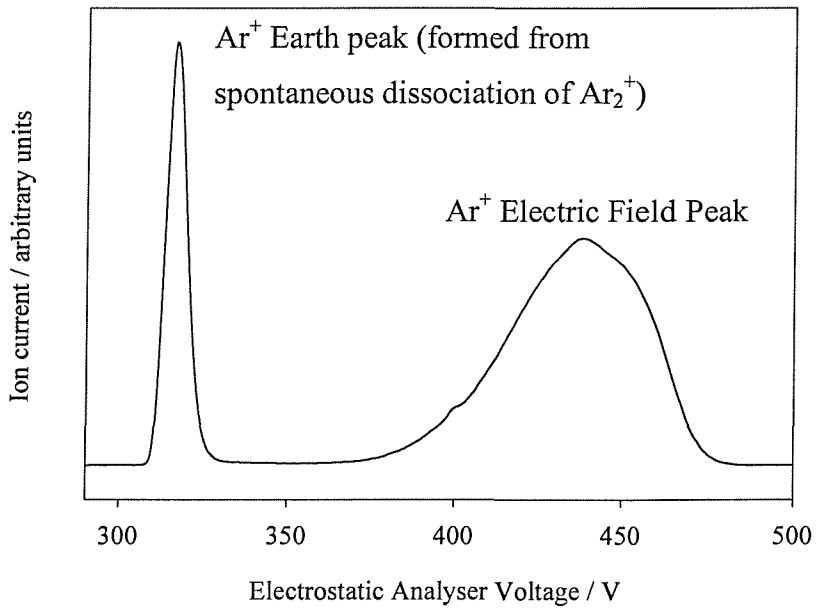

Figure 3.4: Ar^+ fragment kinetic energy spectrum obtained by scanning the ESA voltage with an electric field of 3.5 kV applied to the electric field lens.

3.5 Signal detection and recording

Energy-selected fragment ions are deflected onto an off-axis electron multiplier (Thorn EMI EM119), the output of which is pre-amplified (Stanford Research Systems, SR570) and passed to a phase-sensitive lock-in amplifier (Stanford Research Systems, SR830). The microwave radiation is 100 % amplitude modulated (period 150 μs) to facilitate the detection of a small change in fragment current against the relatively large background. The phase-sensitive detection method is required for the vast majority of the transitions observed in this work, although a few may be observed with DC detection.

Frequency scanning and signal recording is controlled by a 486 PC via an IEEE-488 bus and a Microlink (D/A, A/D) converter. The combination of automatic data collection and a relatively stable ion beam allows scanning to be performed automatically for periods of 24 hours or more. This aids both the search for new transitions and signal averaging of weak resonances. The search for transitions in a new molecular system is performed by scanning at a rate of 1 MHz every three seconds, or 1.2 GHz h^{-1}. The microwave radiation is frequency modulated (typically at 4 MHz) to broaden artificially any transitions, thereby increasing their chance of detection. To sample different bands of energy levels within a molecule both the source potential and the electric field lens potential must be varied. Therefore an extensive scan, involving full frequency coverage (6–140 GHz) at eight combinations of source and electric field potentials, requires approximately one and a half months of continuous scanning. This illustrates the advantage of the ability to detect fragments arising from most near-dissociation energy levels, simply by monitoring the top of the electric field peak: if a number of positions on the electric field peak had to be monitored, the time needed to search for new transitions would be greatly increased.

Once a transition is detected by this "blindscanning" method, it must then be measured accurately. For this, the detection conditions are optimised by monitoring the signal strength as a function of electrostatic analyser potential. Figure 3.5 is a typical optimisation scan showing both a positive and a negative change in fragment current, corresponding to fragments arising from each of the levels involved in the transition.

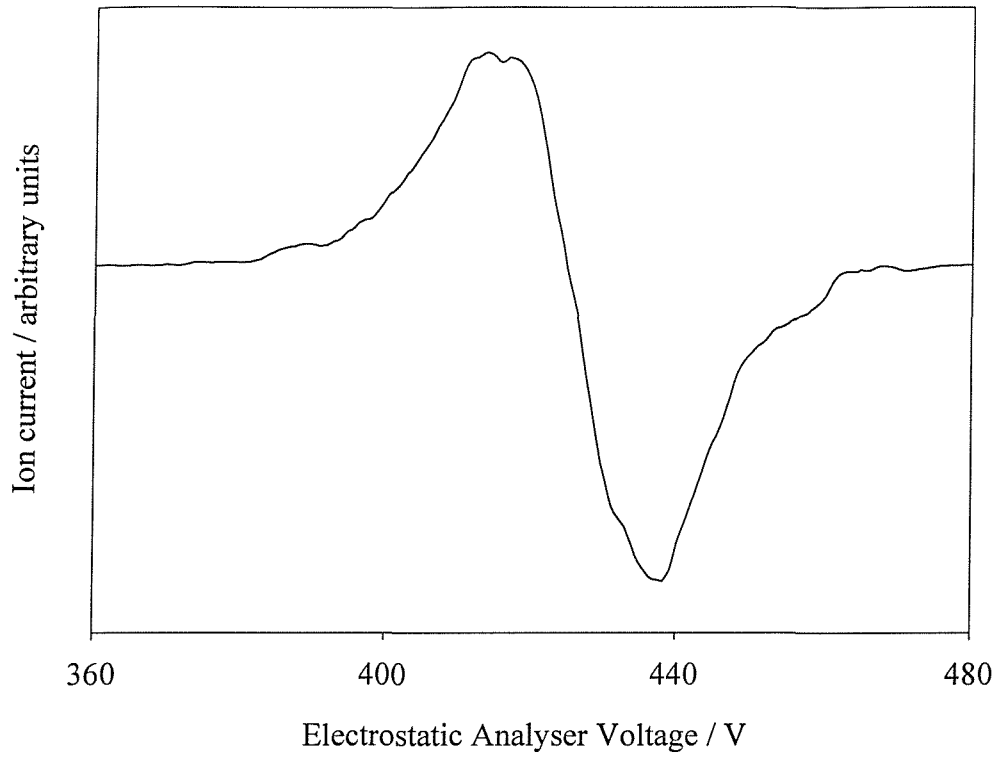

Figure 3.5: An electrostatic analyser optimisation scan of the 15591.1 MHz transition in Ne_2^+, showing both an increase and decrease in fragment current.

The frequency modulation is then removed and the transition scanned at a resolution of 0.1 MHz per point. The microwave power must often be adjusted to achieve the best resolution recording of the transition. The rest frequency is then determined from the resulting microwave mode pattern (typical accuracy ± 0.5 MHz).

3.6 Additional experimental techniques

Single photon experiments such as those detailed in Section 3.5 provide an excellent method for the detection and measurement of new transitions but they provide no information about the assignment of transitions that do not display hyperfine structure. For this reason, two further experimental techniques are employed; microwave-microwave double resonance and study of the Zeeman effect. These important techniques are described in detail in Sections 3.6.1 and 3.6.2 respectively.

3.6.1 Microwave-microwave double resonance experiments

The technique of double resonance has two main uses: firstly, to establish if two known transitions share a common energy level and secondly, to search for new transitions. The latter is performed using a "blindscan" method similar to that described in Section 3.5. In the case of Ne_2^+ especially, this has been found to be the most efficient way to connect transitions to an existing experimental network.

Microwave double resonance experiments are performed by simultaneously launching two different microwave frequencies into the waveguide via a four port E- and H-plane magic-T. The efficiency of a magic-T above its optimum frequency range is highly variable and in general it is easier to perform low frequency double resonance experiments than those involving high frequencies. It must also be noted that due to limitations in the microwave equipment, some double resonance experiments are not possible.

In these experiments the frequency of one of the synthesisers is fixed to "pump" a known transition (AM), whilst the second synthesiser is used to scan the desired frequency range (CW). A typical double resonance scan showing that the transitions 61066.2 MHz and 19107.2 MHz in Ne_2^+ share a common level is shown in Figure 3.6: The baseline is high since the 61066.2 MHz transition is being constantly driven. The 19107.2 MHz transition is then scanned with the second synthesiser and at the frequencies of the antiparallel and parallel a change in population of the level linking the two transitions is observed. If these two transitions did *not* share a common level, the baseline would have been flat. This double resonance technique involves a delicate balance of populations and microwave power levels. If either of these is unfavourable, then what *should* be a positive result is sometimes not observed. For this reason, only positive information (*i.e.* the observation of double resonance) may be utilised.

Despite the limitations of this technique, it has proved to be invaluable for establishing experimental assignments. The conventional use of this technique is to determine connectivities between transitions, but it also has at least two other valuable uses. Firstly, to probe further down the well than is possible with a single photon: the maximum field that may be applied to the electric field lens limits the depth down the well that may be accessed by a single photon.

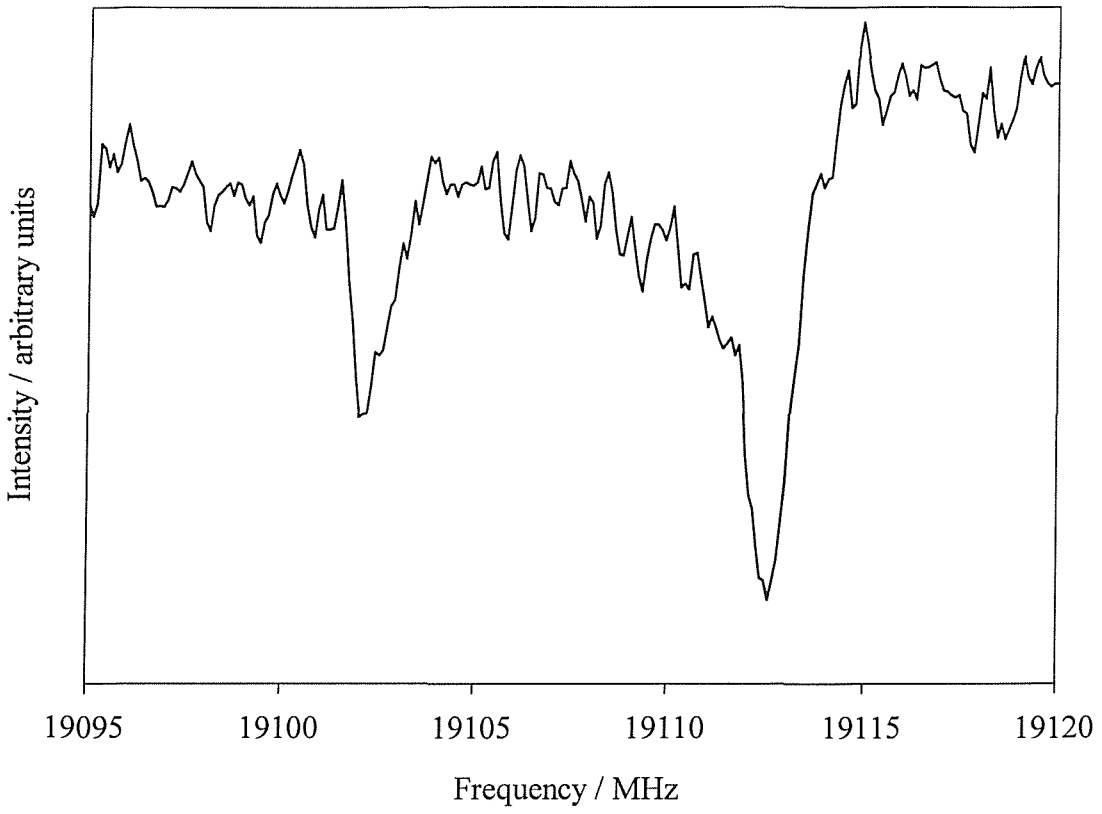

Figure 3.6: Example of a double resonance scan in Ne_2^+ (see text for explanation).

For example, in Ne_2^+ it has been possible to dissociate levels that lie *ca.* 7 cm^{-1} below the dissociation limit, and using double resonance it is possible to access levels that are bound by a further 5 cm^{-1}. Secondly, if the absolute populations of two levels are very small or if their population difference is small, then this situation can be resolved by "pumping" to one of the levels. This transfers population and thus may enable the observation of a level that may not be seen using a single photon. Double resonance used in this way has been vital in the observation of some transitions involving levels that both lie very close to the dissociation limit.

3.6.2 The Zeeman effect

As outlined in Section 2.3, an applied magnetic field interacts with the magnetic moments arising from the electron spin and orbital angular momenta. This causes an energy level with total angular momentum, J, to split into its M_J components, where

M_J defines the projection of J with reference to the laboratory fixed z-axis. The resulting pattern of Zeeman components may be interpreted in terms of the total angular momentum quantum numbers and the effective g-factors of both levels involved in the transition. The effective g-factors provide useful labels for the energy levels (see Section 2.3 and Tables 2.1 and 2.2), indicating the nature of the angular momentum coupling in the system. They may also be used to guide double resonance experiments, since if two transitions both involve a level with a given J-value and g-factor, then it is quite likely that they are connected.

The Zeeman splitting produced by an axial magnetic field can depend upon which microwave mode is chosen for study. In the simplest cases, when only the fundamental TE_{10} is propagated (TM_{10} does not exist), the microwave electric field and axial dc magnetic field are perpendicular. This means that Zeeman components obey the selection rule $\Delta M_J = \pm 1$, where M_J is the component of J in the external magnetic field direction. If, however, a resonance resulting from a more intense higher-order mode is chosen, the selection rule depends upon the distribution of the microwave power between the degenerate TE and TM modes. In nearly all cases it is found that the observed Zeeman patterns conform solely to the $\Delta M_J = 0$ selection rule. This suggests that the power is propagated predominantly in the TM mode, the interaction occurring mainly in the centre of the waveguide where the electric field is parallel to the external magnetic field. Wherever possible it is advantageous to study the Zeeman pattern of a TE_{10} mode since this yields g-factors for both levels involved in a transition; $\Delta M_J = 0$ transitions only reveal Δg.

The effect of applying an external field to the transition in Ne_2^+ with a rest frequency of 29354.2 MHz is clearly shown in Figure 3.7. The mode under study is a TE_{10} mode, and it exhibits two branches (which overlap) when an external magnetic field is applied. The two branches are a result of the $\Delta M_J = \pm 1$ selection rule applicable to this microwave mode. This Zeeman spectrum is analysed easily and shows that this transition is $J = 5/2$, $g = -0.071$ to $J = 3/2$, $g = -0.511$. Figure 3.8 shows the theoretical reconstruction of this transition.

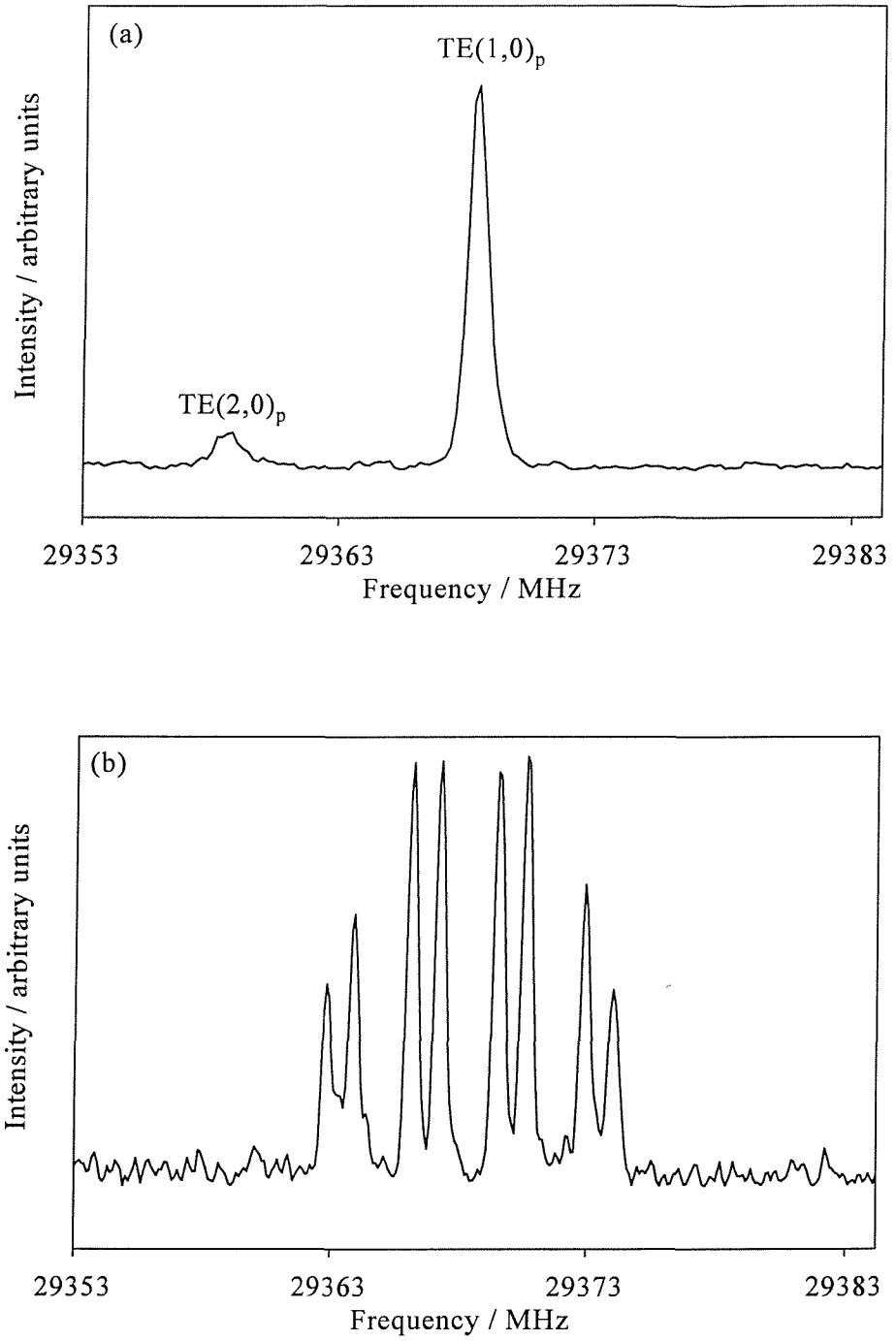

Figure 3.7: (a) The 29345.2 MHz transition of Ne_2^+ at zero field. (b) The Zeeman pattern of the same transition in a magnetic field of 5.55 G, recorded at a slightly lower microwave power to eliminate contamination from the $TE(2,0)_p$ mode. The transition is $J = 3/2 \leftrightarrow J = 5/2$ and the g-factors are determined to be -0.511 and -0.071 for the $J = 3/2$ and $J = 5/2$ levels, respectively.

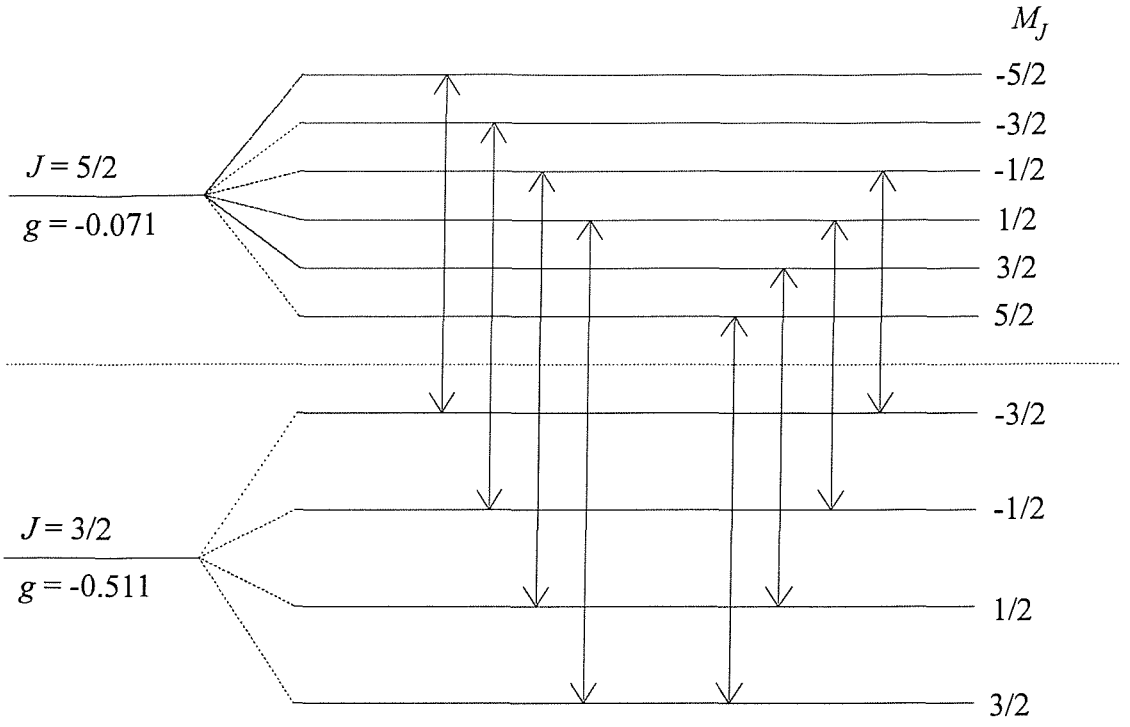

Figure 3.8: Theoretical reconstruction of the Zeeman pattern shown in Figure 3.7.

3.7 Concluding remarks

The experiments described here provide an extremely sensitive method for probing the near-dissociation energy levels of molecular ions. Much of this sensitivity arises from the use of the electric field dissociation technique, which effectively converts absorbed microwave photons into easily detectable fragment ions. Once detected, transitions may be analysed further by study of the Zeeman effect. Microwave-microwave double resonance experiments establish connectivities between the transitions and also determine the relative positions of the levels in the molecular ion. The combination of these two powerful techniques allows the construction of detailed experimental energy level diagrams that describe near-dissociation states of molecular ions.

Chapter 4 - The microwave electronic spectrum of Ne_2^+

4.1 Introduction

A considerable amount of work has been devoted to both the experimental and theoretical study of the inert gas dimer ions. In the 1970s much of this work was directed toward investigating the role that the electronic excitation of these ions may play in excimer lasers, where it has been proposed that such a process could influence the absorption properties of the laser medium [60]. More recently there has been extensive debate, particularly with reference to Ar_n^+, as to whether Rg_2^+ or Rg_3^+ forms the central core in higher order clusters, Rg_n^+. (The reader is referred to Section 5.1 for a detailed discussion on this point). Clearly a detailed knowledge of the energy levels in the diatomic ions would help to improve the understanding of the rare-gas cluster ions.

Carrington and co-workers successfully studied the near-dissociation states of He_2^+ [33], $HeAr^+$ [34] and $HeKr^+$ [35], forming the ions by excitation of the helium atom, followed by an autoionisation reaction with He, Ar and Kr respectively. The excess energy of the excited helium atoms was sufficient to populate all ground state vibration-rotation levels of the ion, up to the dissociation limit. Since it is not possible to use this method for the study of rare-gas diatomic ions that do not contain helium, another mechanism was needed to populate the near-dissociation states of other rare-gas ions.

As discussed in Section 1.2.1, it is expected that the vertical ionisation of a neutral van der Waals dimer will result in significant population of near-dissociation states in the ion. The molecular beam chamber described in Section 3.2 was built to exploit this process [43], and the first molecular ion to be made using this method was $Ar\cdots Ar^+$. The main reasons for this were that it was easy to make a large beam of Ar_2^+, it displayed a large, well-defined electric field peak and argon is relatively inexpensive. Additionally, Ar_2^+ is the most well studied of the rare-gas dimer ions and so it was therefore natural to study Ar_2^+ first. However, the initial search yielded only 25 transitions, and it was soon found that although an applied magnetic field

affected all of the transitions, none of them produced a Zeeman spectrum with resolved components. This observation suggested that these transitions involved states of high rotational quantum number, J, indicating a high rotational temperature in the beam (possibly caused by the breakdown of higher order clusters, Ar_n^+ ($n \geq 3$)).

Attention therefore focused on the study of $^{20}Ne_2^+$, because neon clusters much less readily than argon, thereby reducing the probability of forming higher clusters that could break down to "contaminate" the Ne_2^+ beam. The number of larger clusters formed can be observed in the mass spectra: for argon, all ionic clusters up to Ar_{13}^+ (which corresponds to the maximum available magnet current) were seen in significant quantities, whereas for neon the predominant cluster was Ne_2^+ with only a very small amount of Ne_3^+ (relative intensity ratio 20:1) and no observable higher clusters.

There have been a number of experimental and theoretical investigations of Ne_2^+, but previous to this work there had been no direct observation of resonant transitions in the ion. The earliest estimate of the dissociation energy of Ne_2^+ was from ion molecule scattering experiments of Mason and Vanderslice [61], who estimated it to be anything between 0.33 and 0.71 eV. Munson *et al.* [62] reported the dissociation energy to be 0.69 ± 0.2 eV by an electron impact technique that suffered from poor energy resolution and poor threshold sensitivity. It is widely accepted that both of these studies were susceptible to large errors and seriously underestimated the true dissociation energy. Kebarle *et al.* [63] studied the positive ions (Ne^+, Ne_2^+) obtained from alpha-particle irradiation of neon. Measuring the recombination energy of Ne_2^+ enabled them to estimate the dissociation energy of Ne_2^+ to be between 1.6 and 2.0 eV.

Throughout the 1960s, Biondi and co-workers carried out many studies of dissociative recombination in the afterglow of noble gases [64]: Connor and Biondi [65] published the first reliable estimate of the dissociation energy (D_0) of Ne_2^+ to be approximately 1.4 eV and this value was later refined by Frommhold and Biondi [66] who obtained $D_0 = 1.35 \pm 0.07$ eV. More recently, Ciurylo *et al.* [67] obtained the velocities of superthermal dissociative recombination products by fitting the Doppler broadened profiles of emission lines in a neon plasma afterglow. Their study yielded a value of $D_0 = 1.20 \pm 0.08$ eV which is directly comparable with a similar, more

recent study by Ramos *et al.* [68] who determined the dissociation energy to be 1.26 ± 0.02 eV. The scattering experiments of Mittman and Weise [69] gave a dissociation energy of $D_e = 1.30 \pm 0.1$ eV.

The photodissociation cross-sections of the homonuclear rare-gas dimer ions were studied by Lee and Smith [70]. They presented little data for Ne_2^+ since the weak spin-orbit coupling caused the absorption cross-section in the visible region to be too small to be measured. A later theoretical study of absorption cross-sections by Wadt [71] validates this experimental observation. Trevor *et al.* [72] studied the photoionisation of neon dimers and the lower bound to the dissociation energy of Ne_2^+ was determined to be 1.24 ± 0.08 eV. This is in excellent agreement with a more recent study by Broström *et al.* [73] who measured the dissociation energy of Ne_2^+ as 1.35 ± 0.1 eV by means of photofragment spectroscopy of the molecular ions in a crossed laser / fast ion beam configuration.

Perhaps the best experimental data available for the ground electronic state of the ion comes from a threshold photoelectron study by Hall *et al.* [74], who observed transitions from the neutral dimer to 20 vibrational levels of the ion. However, there is some uncertainty in the absolute vibrational assignment due to the unfavourable Frank-Condon factors for the excitation to the low-lying levels of the ion. These levels are only observed as a result of autoionising effects and it is conceivable that a number of more strongly bound levels are not detected. Their favoured assignment assumes that the first observed level corresponds to $v = 2$. Using this assumption the dissociation energy is determined to be 1.291 ± 0.01 eV. Similarly, the vibrational constants are determined to be $\omega_e = 569.4 \pm 3.2$ cm^{-1} and $\omega_e x_e = 7.4 \pm 0.2$ cm^{-1}. A supplementary investigation was undertaken by Kim *et al.* [75] who observed the vibrational structure of Ne_2^+ in Rydberg studies of the neutral Ne_2 converging on $X^2\Sigma_u^+$, $v^+ = 0$–2 of the ion. Their studies yielded estimates for the vibrational constants of the ground electronic state of $\omega_e = 586.0 \pm 2.0$ cm^{-1} and $\omega_e x_e = 5.4 \pm 0.8$ cm^{-1}.

These experimental studies only provide information on the ground state of Ne_2^+ ($X^2\Sigma_{1/2\,u}^+$) and in most cases this information is limited to an estimate of the dissociation energy. There are however numerous theoretical studies of Ne_2^+ [73, 76 - 83], many of which provide useful information on the excited states of Ne_2^+. A

summary of the experimental and theoretical studies of the ground state of Ne_2^+ is provided in Table 4.1.

Previous to this work the best potential curves for Ne_2^+ are the high level *ab initio* calculations of Naumkin and Wales [83]. These potentials were used as a basis for a diatomics-in-molecules study of the structure of larger singly-charged neon clusters, Ne_n^+. Their curves, calculated without spin-orbit coupling, are shown in Figure 4.1. The interaction of $Ne(^1S)$ and $Ne^+(^2P)$ gives rise to four states, $^2\Sigma_u^+$, $^2\Pi_g$, $^2\Pi_u$ and $^2\Sigma_g^+$ which are degenerate at dissociation. However, the inclusion of spin-orbit coupling splits the atomic ion into two states ($^2P_{3/2}$, $^2P_{1/2}$) separated by 782 cm^{-1} [84] and consequently $Ne(^1S) + Ne^+(^2P)$ has two dissociation limits, split by this amount. The effect of spin-orbit coupling on the potentials is to mix Σ and Π states of the same *g/u* symmetry; each of the Π states are split into two, giving a total of six states. The lowest dissociation limit (I) is $Ne(^1S) + Ne^+(^2P_{3/2})$, to which four electronic states converge. In a Hund's case (c) nomenclature, these are I $(1/2)_u$, I $(3/2)_u$, I $(1/2)_g$ and I $(3/2)_g$, where (1/2) and (3/2) denote the respective components ($|\Omega|$) of the electronic angular momentum J_a for the atomic ion along the internuclear axis (Section 2.2.2). Two states correlate with the next highest dissociation limit ($Ne(^1S) + Ne^+(^2P_{1/2})$) and are labelled II $(1/2)_u$ and II $(1/2)_g$. Near to the dissociation limit the use of Hund's case (c) labels is more appropriate than case (a) or case (b) since the magnitude of the spin-orbit coupling is greater than the chemical forces involved.

The ground state (I $(1/2)_u$) becomes slightly shallower as a result of spin-orbit coupling, due to the mixing of the strongly attractive $^2\Sigma_u^+$ state with the predominantly repulsive $^2\Pi_u$ state; the II $(1/2)_u$ state becomes deeper accordingly. It must also be noted that the spin-orbit coupling creates a state that possesses a double minimum, the I $(1/2)_g$. This arises from an interesting interaction between the $^2\Sigma_g^+$ and $^2\Pi_g$ potentials: at large values of internuclear distance, r, the two states are strongly mixed, but as r decreases, the Σ orbitals overlap before the Π orbitals. Consequently, the Σ state begins to be repulsive at a larger r than where the Π state starts to become attractive, resulting in an increased energy of the mixed state (the maximum). At shorter r the state becomes nearly pure Π (*i.e.* bonding), and thus

there is a relatively deep inner well. Later in this Chapter it will be seen that this double minimum has an interesting and significant effect on the observed spectrum.

The best characterisation of the potential curves for these six states are those of the present work. They are shown in Figure 4.2 and a full description of how these curves are constructed will be given in Section 4.4.4.

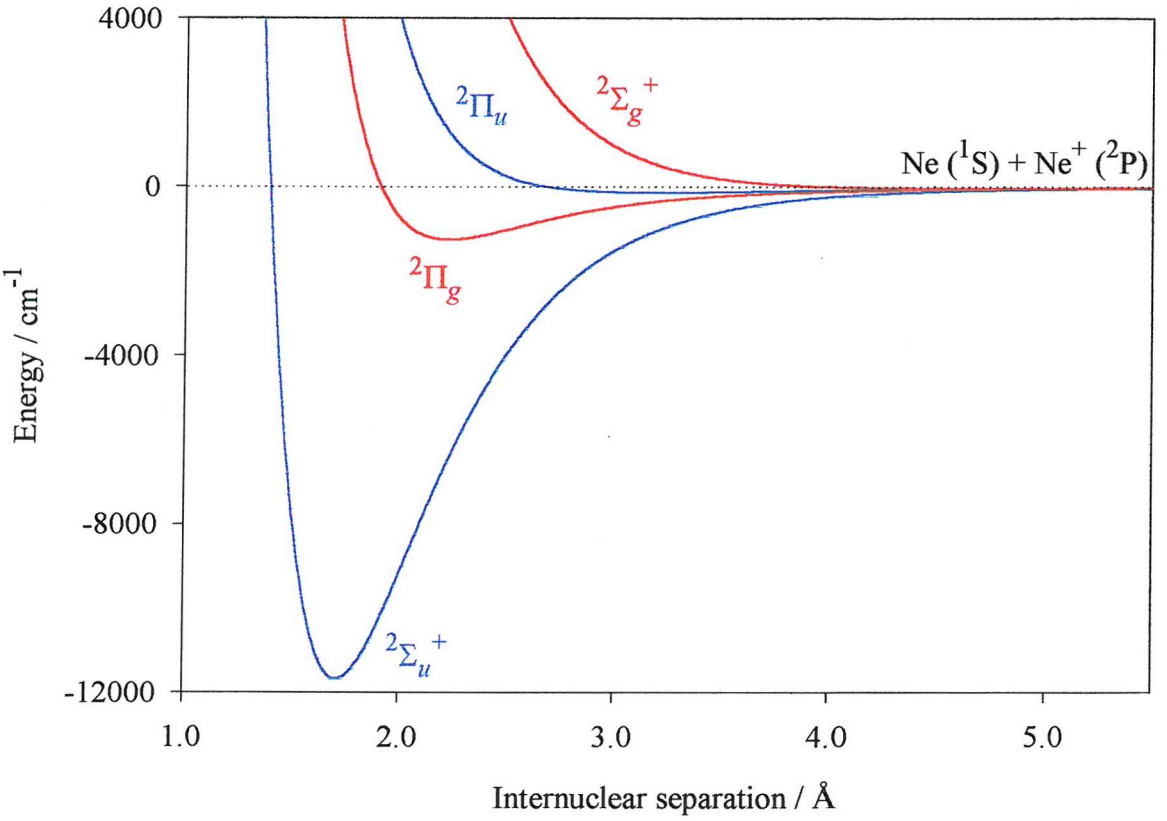

Figure 4.1: The Ne_2^+ potential energy curves of Naumkin and Wales [83], without spin-orbit coupling.

Table 4.1: Experimental and theoretical studies of Ne_2^+ ($X\,^2\Sigma_{1/2u}^+$). * See glossary on page 146 for list of abbreviations used.

Method	D_0 / eV	ω_e / cm^{-1}	$\omega_e x_e$ / cm^{-1}	Reference (year)
EXPERIMENT				
Dissociative Recombination	1.35 ± 0.07	-	-	Frommhold and Biondi (1969) [66]
Rainbow Scattering	1.30 ± 0.1 (D_e)	-	-	Mittman and Weise (1974) [69]
Vacuum UV Photoionisation Spectroscopy	1.24 ± 0.08	-	-	Trevor *et al.* (1984) [72]
Photofragment Spectroscopy	1.35 ± 0.1	-	-	Broström *et al.* (1991) [73]
Study of Rydberg States	-	586.0 ± 2.0	5.4 ± 0.8	Kim *et al.* (1992) [75]
Dissociative Recombination	1.20 ± 0.08 (D_e)	-	-	Ciurylo *et al.* (1994) [67]
Photoelectron Spectroscopy	1.291 ± 0.01	569.4 ± 3.2	7.4 ± 0.2	Hall *et al.* (1995) [74]
Dissociative Recombination	1.26 ± 0.02	-	-	Ramos *et al.* (1997) [68]
THEORY *				
SCF	1.61	660	-	Gilbert and Wahl (1971) [76]
CI	1.20	550.1	7.1	Cohen and Schneider (1974) [77]
Density functional method	1.310	597.0	6.1	Michels *et al.* (1978) [78]
UMP4	1.258	-	-	Frenking *et al.* (1989) [79]
MRCCI + Q	1.32	598.5	8.2	Broström *et al.* (1991) [73]
QCISD(t)	1.376 (D_e)	591	-	López (1995) [80]
MR MBPT	1.283	588.3	8.7	Mášik *et al.* (1997) [81]
Calculated on the basis of experimental data	1.341	-	-	Chen *et al.* (1997) [82]
RCCSD-T	1.376	605.2	8.0	Naumkin and Wales (1998) [83]

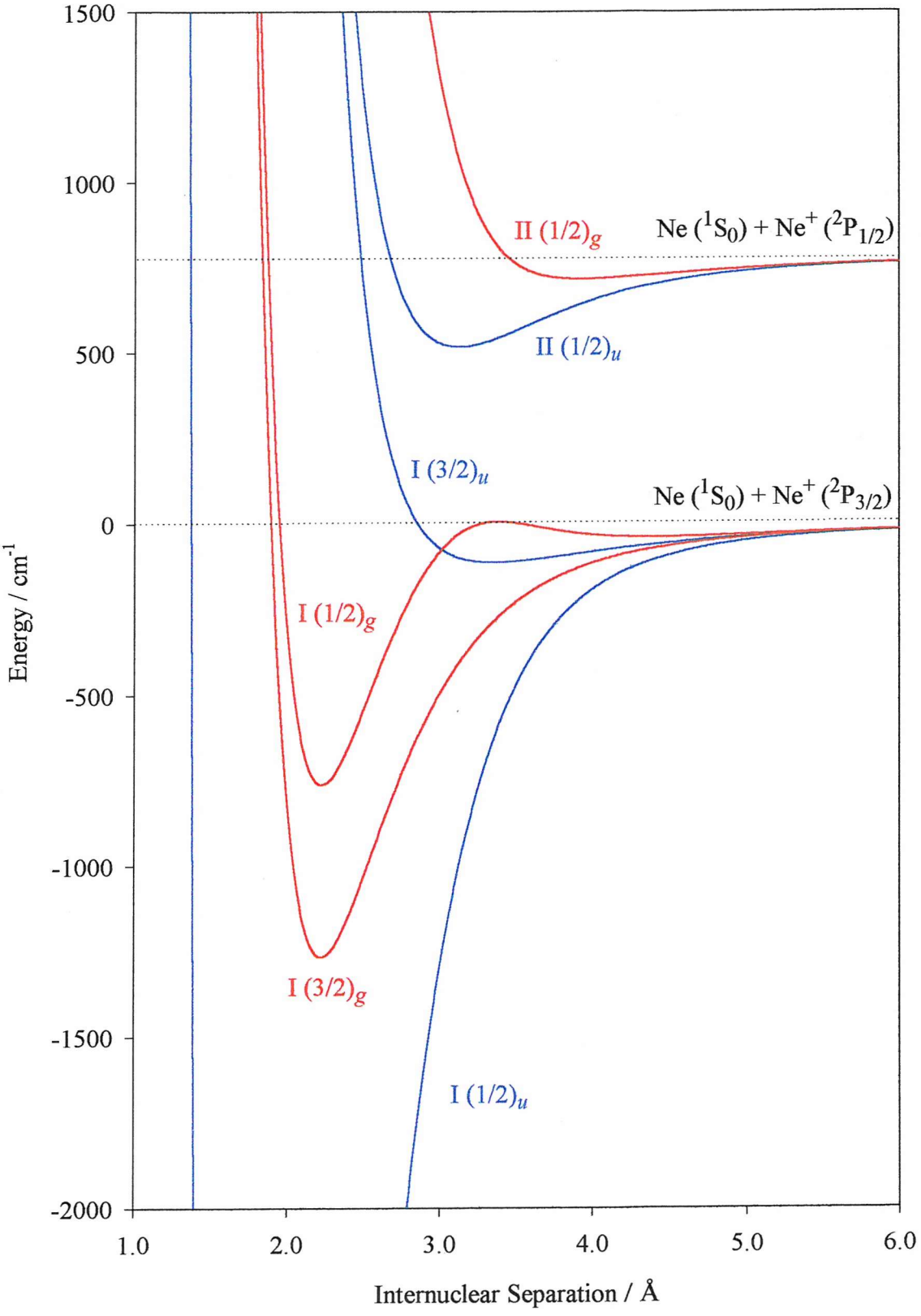

Figure 4.2: The Ne_2^+ potential curves of this work, including spin-orbit coupling. See Section 4.4 for their derivation.

4.2 Experimental

The initial search for near-dissociation microwave transitions in Ne_2^+ (using a source voltage of 6 kV and a number of different electric field voltages) yielded many well-resolved transitions in the frequency range 6–170 GHz, although there were no discernible patterns in this spectrum. Unlike most experimental spectra, in this work no information may be gleaned from the intensity of each resonance: the transition intensities depend on a number of factors in addition to the electric dipole intensity. Such factors include the population difference between the levels involved in a transition and the detection efficiency, which is neither optimal nor constant from one transition to another. In the case of frequencies > 40 GHz it is not possible to measure the power delivered to the waveguide and it cannot be guaranteed that the waveguide is always optimally aligned since the position changes every time the waveguide is changed. There are also other experimental factors, such as the condition of the source and filament that cause differences in the recorded intensity of transitions on a day-to-day basis.

If just the frequency information had been available it is doubtful whether any progress could have been made in assigning the observed transitions. There are, however (as described in Section 3.6), two very valuable additional experimental techniques that are available to help assign transitions: microwave-microwave double resonance and study of the Zeeman effect. A third tool known as the method of quadrangles [34], is also very useful especially in the early stages of an investigation, and this method will now be explained.

If four energy levels are chosen (two of each parity) that can be interconnected by a set of four electric dipole allowed transitions, then the frequencies of these transitions (ν_1, ν_2, ν_3, ν_4) will satisfy one of the following relationships:

$$\nu_1 + \nu_4 = \nu_2 + \nu_3 \tag{4.1}$$

$$\nu_1 + \nu_2 + \nu_3 = \nu_4, \tag{4.2}$$

i.e. either the frequency sums of two pairs are equal, or one frequency is equal to the sum of the other three.

Therefore a set of four transitions from the spectrum whose frequencies satisfy either Equation 4.1 or 4.2 to within a given tolerance (usually 1.0 MHz to allow for experimental error) are *possibly* linked in one of the six ways shown in Figure 4.3. To determine if the predicted quadrangle does indeed relate to a genuine relationship between four levels in the molecular ion, a series of suitable double resonance experiments must be performed. However, as the number of observed transitions increases, the number of predicted quadrangles that are *not* genuine increases very rapidly. These spurious quadrangles hinder the experimental progress and therefore this method of predicting connectivities is useful only at the start of an experimental investigation.

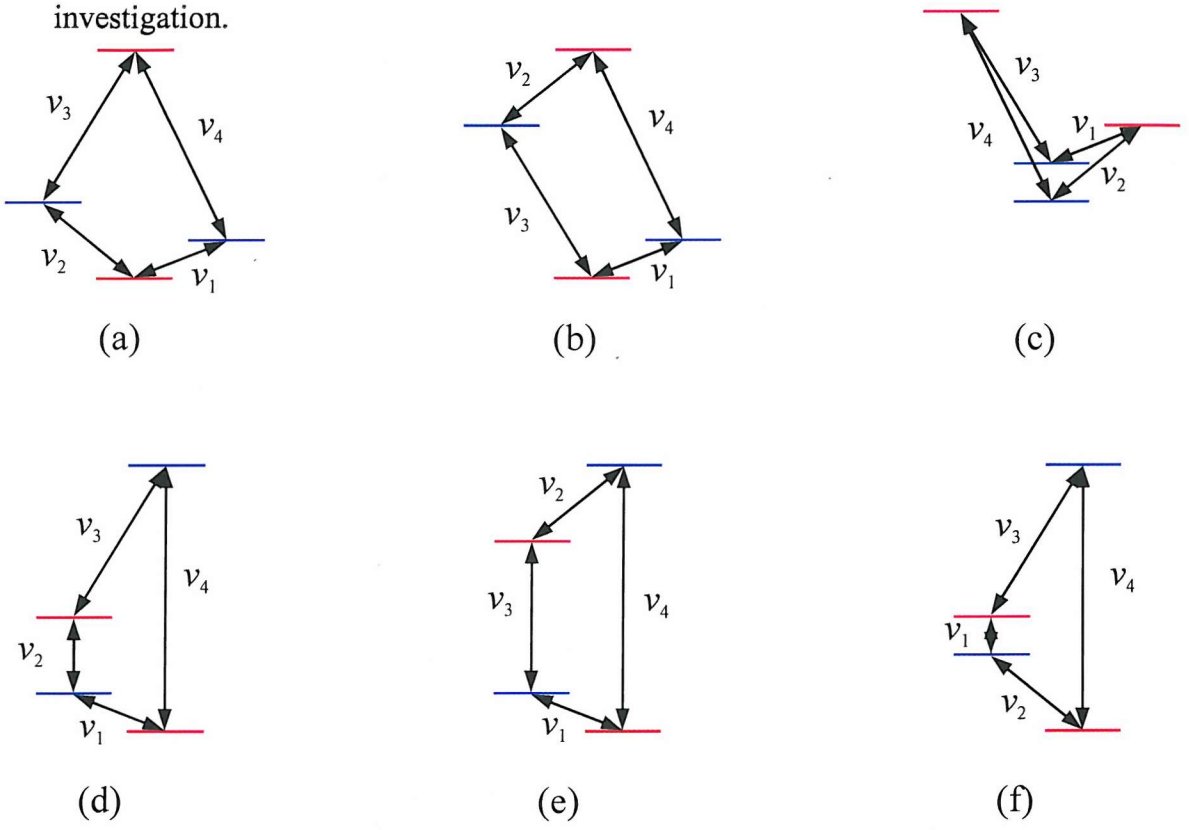

Figure 4.3: Possible connectivities for quadrangles. Arrangements (a), (b) and (c) correspond to Equation 4.1 and arrangements (d), (e) and (f) correspond to Equation 4.2. Lines of different colour are used to show energy levels of different parity, and all arrangements may be in either orientation with respect to the dissociation limit.

To construct an energy level diagram for Ne_2^+, microwave-microwave double resonance was found to be the most useful of the three experimental tools available. Figure 4.4 illustrates a method by which new levels were often added to an existing network. If it is assumed that levels (a), (b), (c) and (d) form part of an existing network, and a currently unassigned transition is known to be in double resonance with both ν_{ac} and ν_{ad}, then it can immediately be concluded that this transition is attached to level (a). For the present purpose this unassigned transition will be labelled ν_{az}. The energy of the transition linking levels (b) and (z) may therefore be predicted for both possible orientations of level (z). The transition ν_{bc} is then pumped and the two predicted frequencies are scanned. If a positive double resonance result is obtained, this result indicates the correct position of level (z) with respect to the existing network. As explained in Section 3.6.1, no conclusion may be drawn from a negative double resonance result. If neither of the double resonance experiments described above yields a positive result, then further experiments must be performed. This may not always be possible at the time, due to lack of suitable levels nearby, and so it may be impossible to confirm the position of the new level (z) until very much later in the investigation, when more information is available.

Despite the problems associated with the double resonance technique, it has proved to be an essential tool for establishing connectivities and experimental assignments within this study.

Valuable information was also gained from the study of the Zeeman effect (Section 3.6.2). For many of the transitions observed in Ne_2^+, this experimental technique provided total angular momentum quantum numbers and g-factors for the levels involved in a transition. Throughout this investigation these results were used to suggest possible connectivities of transitions and were invaluable in determining absolute assignments of J and parity.

Although the study of the Zeeman effect has been an invaluable aid to the assignment of transitions, there are a number of potential problems that may be encountered during analysis. The components of different branches often overlap such that it is not possible to count the total number of lines within each branch (and thus determine the values of J). The level of microwave power is often difficult to optimise, since too much power is likely to result in poor resolution of the peaks (and

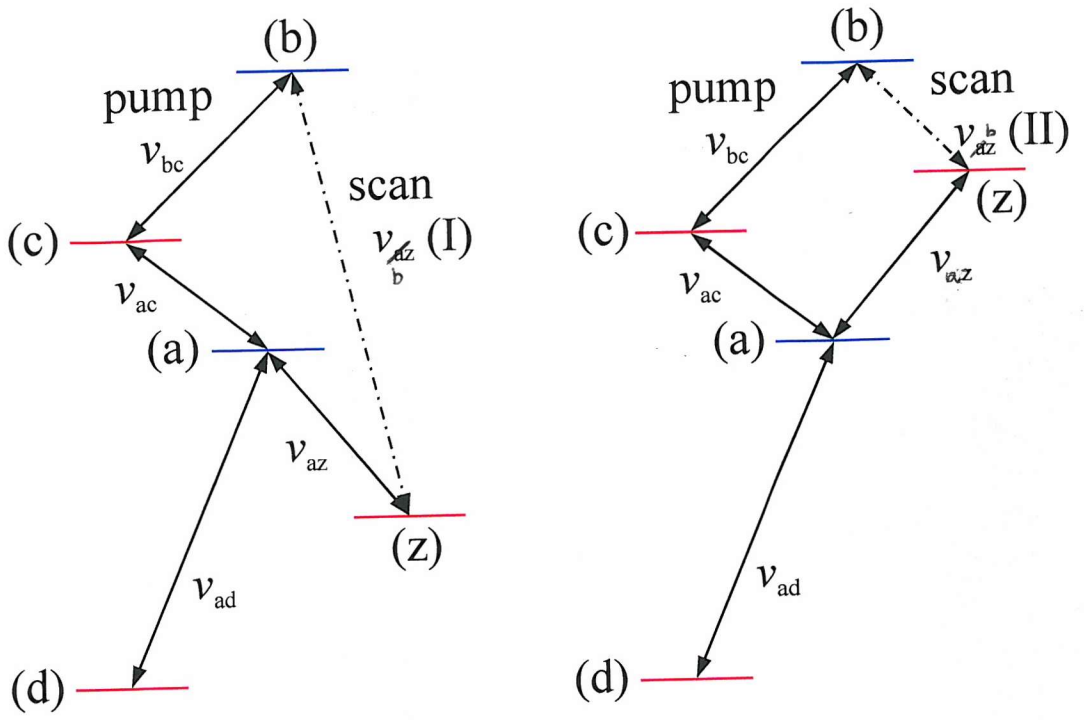

Figure 4.4: Double resonance experiment connecting a new level to an existing network of levels. See text for detailed explanation.

---

thus adds uncertainty to the number of lines and their frequency). Too little power however, may cause the weakest peaks to be unobservable thereby causing the analysis to be incorrect. For all but the very strongest transitions this problem was overcome by using a low microwave power level and signal-averaging, often overnight. Also, for transitions where more than one mode is observed, Zeeman spectra are often contaminated by the presence of these other modes. Some such transitions may still be analysed, though this was not possible for many of the transitions at the highest frequencies, where complicated multi-moding is most prevalent. Furthermore, second order Zeeman effects are observed when one or both of the levels involved in a transition is perturbed by a nearby level. It is often still possible to estimate the values of J from such a spectrum, but these cannot be relied upon without complementary evidence such as double resonance.

Once the connectivities of approximately 40 levels had been determined, further "blindscanning" was carried out using a source voltage of 3 kV and a small electric field lens potential of 0.5 kV. Using such a small electric field lens potential

had not been practicable whilst the source voltage was at 6 kV because the "earth" fragment peak and electric field dissociation peak (Section 3.4) occurred at very similar electrostatic analyser voltages and consequently the two could not be distinguished. At a source voltage of 3 kV however, the electric field dissociation peak was shifted sufficiently from the earth peak to be of practical use. The greatest advantage of lowering the source voltage was to reduce the "stripping" of levels near to dissociation (see Section 3.2), and so transitions to and between these levels were now detectable. Over 100 new transitions were found under these conditions and the number of levels in the energy level diagram approximately doubled.

The combination of these experiments initially led to the construction of an energy level diagram containing 85 levels connected by 182 transitions [85]. Towards the end of the investigation, coupled channel calculations (Section 4.4) provided excellent predictions for the "locations" of further levels. An additional 17 levels were discovered using these calculations as guidance, taking the total number of experimentally-found levels to 102, connected by 204 transitions. The complete list of the 278 microwave transitions recorded for $Ne^{\cdots}Ne^{+}$ are listed, with assignments where possible, in the Appendix. The experimental energy level diagram, which assigns 73 % of the recorded transitions, is shown in Figure 4.5. The levels are labelled arbitrarily from 1–102 and the levels are drawn with a blue line to denote u-state levels and a red line to denote g-state levels. It is clear from the g-factor measurements that all of the observed levels in Figure 4.5 correlate with the first dissociation limit, $Ne(^1S) + Ne^+(^2P_{3/2})$ ($J_a = 3/2$) and the assignment of g / u symmetry labels is based on the observation of the g-factors of the $J = 1/2$ levels. These are compared with the limiting g-factors in a Hund's case (c) (or case (e)) basis set (see Section 2.3.1) and the assignment is straightforward. However there are five levels, labelled 3, 13, 28, 49 and 65 that are drawn with a red dotted line. These levels do not conform to the expected pattern and appear to be responsible for a number of local perturbations. These levels are assigned to the inner well of the I $(1/2)_g$ state and discussed fully in Section 4.4.5.

The energies of the levels (relative to level 1) and their g-factors (where measured) are given in Table 4.2. It has not been possible to determine g-factors for some of the levels because either they have not been accessed without the assistance

of double resonance or the Zeeman spectrum was uninterpretable. Table 4.2 also includes Hund's case (c) Ω assignments and case (e) R assignments. Justification for assigning both sets of quantum numbers is detailed in Section 4.3.1.

There remain 74 transitions whose rest frequencies have been accurately determined but have not been experimentally assigned or linked to the network of energy levels shown in Figure 4.5. There are also at least a further 70 transitions that have been observed but whose rest frequencies have not been accurately determined. Clearly there are some levels missing from Figure 4.5 and it can be assumed that some of the unassigned transitions link some of these unobserved levels to the energy level diagram, although experiments performed to show this have been unsuccessful. Some of the missing levels have been searched for very thoroughly but to no avail, for example the $J = 1/2$ g-state level which is expected to be located at a slightly lower energy than the u-state level 4. Despite numerous attempts to locate this level using all possible transitions to transfer population, a transition to that level could not be observed. There are a number of other levels that similarly cannot be experimentally located, particularly those within 2 cm^{-1} of dissociation. It is almost certain that this is due to population effects from the vertical ionisation process, which selectively populates some vibration levels (controlled by Frank-Condon factors) and it is difficult to observe the transitions between all vibrational states. The reason for such failures would be equal (or zero) populations in both levels.

Some of the unassigned transitions display Zeeman spectra that suggest they connect energy levels of $J \geq 21/2$. Attempts to link such transitions or to link them to the existing energy level diagram have been futile. At least three of the unassigned transitions (23101.6, 23868.2 and 26683.3 MHz) are of low J (1/2, 3/2) and can be assigned to the upper dissociation limit $Ne(^1S) + Ne^+(^2P_{1/2})$ ($J_a = 1/2$) on the basis of their limiting g-factors. However, attempts to link these transitions together have been unsuccessful, as has searching for adjoining transitions by the double resonance "blindscanning" method described in Section 3.6.1. It is reasonable to assume, though, that more of the unassigned transitions belong to the upper dissociation limit, although these have yet to be identified.

The patterns of the energy levels are discussed in greater detail in the next section.

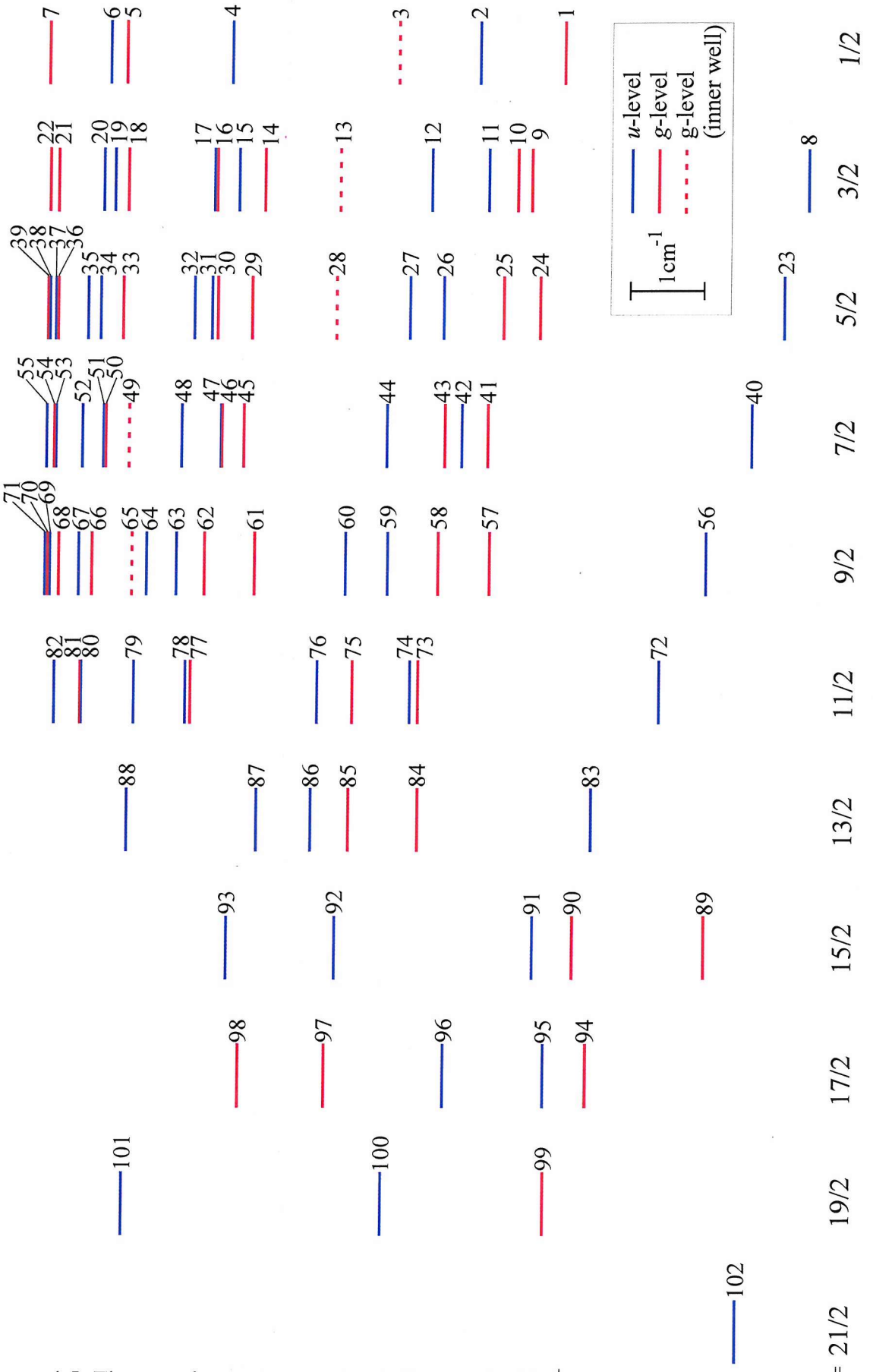

Figure 4.5: The experimental energy level diagram for Ne_2^+.

Table 4.2: Assignments of experimental energy levels. IN denotes inner-well level, *indicates value not available and † indicates assignment based on theoretical analysis (Section 4.4.4).

Level no.	J	$\|\Omega\|$	R	ε	Energy / MHz	g-factor
1	1/2	1/2	1	+	0.0 (defined)	1.945
2	1/2	1/2	2	–	34138.6	-1.340
3	1/2	IN	IN	+	66950.7	1.437
4	1/2	1/2	2	–	133878.0	-1.330
5	1/2	1/2	1	+	176360.3	2.2
6	1/2	1/2	2	–	182764.4	-1.394
7	1/2	1/2	1	+	208508.7	*
8	3/2	3/2	2	–	-98454.9	0.781
9	3/2	3/2	1	+	12893.8	0.732
10	3/2	1/2	3	+	18547.7	-0.511
11	3/2	1/2	0	–	30151.6	0.925
12	3/2	3/2	2	–	53109.6	0.676
13	3/2	IN	IN	+	90131.0	-0.424
14	3/2	3/2	1	+	120431.9	*
15	3/2	1/2	0	–	130783.5	1.043
16	3/2	1/2	3	+	139582.2	-0.655
17	3/2	3/2	2	–	140646.9	*
18	3/2	3/2	1	+	175245.4	0.980
19	3/2	1/2	0	–	180545.6	1.159
20	3/2	3/2	2	–	185037.0	0.476
21	3/2	*	*	+	203106.2	*
22	3/2	*	*	+	207276.9	*
23	5/2	3/2	4	–	-88707.0	*
24	5/2	1/2	1	+	9238.3	0.635
25	5/2	3/2	3	+	23717.4	0.181
26	5/2	1/2	2	–	47901.9	-0.071
27	5/2	3/2	4	–	61458.4	0.000
28	5/2	IN	IN	+	91207.8	0.367

Table 4.2: *(Continued)*

Level no.	J	$\|\Omega\|$	R	ε	Energy / MHz	g-factor
29	5/2	1/2†	1	+	125123.2	0.475
30	5/2	3/2†	3	+	138835.7	0.277
31	5/2	1/2	2	–	141213.9	0.322
32	5/2	3/2	4	–	148284.6	-0.397
33	5/2	1/2	1	+	176987.0	0.772
34	5/2	1/2	2	–	185869.3	0.471
35	5/2	3/2	4	–	190941.1	-0.541
36	5/2	3/2†	*	+	202888.4	*
37	5/2	1/2	2	–	203680.0	*
38	5/2	3/2	4	–	206585.0	*
39	5/2	*	*	+	207385.8	*
40	7/2	3/2	4	–	-75875.1	*
41	7/2	3/2	3	+	29715.8	0.293
42	7/2	1/2	2	–	40095.3	0.464
43	7/2	1/2	5	+	46938.2	-0.406
44	7/2	3/2	4	–	70356.9	0.090
45	7/2	3/2†	3	+	127928.4	*
46	7/2	1/2†	5	+	136750.5	-0.226
47	7/2	1/2	2	–	137190.7	0.508
48	7/2	3/2	4	–	152871.7	0.052
49	7/2	IN†	IN	+	174066.3	-0.174
50	7/2	3/2†	3	+	183417.5	0.153
51	7/2	1/2	2	–	184338.5	0.543
52	7/2	3/2	4	–	192652.0	0.000
53	7/2	1/2	2	–	203244.3	*
54	7/2	*	*	+	203446.0	*
55	7/2	3/2	4	–	206976.5	*
56	9/2	3/2	6	–	-57904.2	*
57	9/2	1/2	3	+	28604.6	0.397
58	9/2	3/2	5	+	49208.9	0.000

Table 4.2: *(Continued)*

Level no.	J	$\|\Omega\|$	R	ε	Energy / MHz	g-factor
59	9/2	1/2	4	–	69704.0	0.073
60	9/2	3/2	6	–	86628.2	-0.211
61	9/2	1/2†	3	+	123272.5	0.360
62	9/2	3/2†	5	+	143376.7	*
63	9/2	1/2	4	–	154620.9	*
64	9/2	3/2	6	–	166626.3	*
65	9/2	IN†	IN	+	172565.3	0.276
66	9/2	1/2†	3	+	188597.1	*
67	9/2	1/2	4	–	193731.2	0.204
68	9/2	*	*	+	197498.1	*
69	9/2	3/2	6	–	201760.9	*
70	9/2	1/2†	*	+	205358.4	*
71	9/2	1/2	4	–	207327.1	*
72	11/2	3/2	6	–	-39226.2	*
73	11/2	3/2	5	+	56909.5	*
74	11/2	1/2	4	–	60205.7	0.305
75	11/2	1/2	7	+	83438.8	*
76	11/2	3/2	6	–	97628.4	0.000
77	11/2	3/2†	5	+	148584.2	*
78	11/2	1/2	4	–	150579.4	0.333
79	11/2	3/2	6	–	171326.4	*
80	11/2	1/2	4	–	192369.7	*
81	11/2	3/2†	5	+	192565.3	*
82	11/2	3/2	6	–	203156.8	-0.028
83	13/2	3/2	8	–	-12583.2	*
84	13/2	1/2	5	+	56720.8	0.284
85	13/2	3/2	7	+	84639.8	*
86	13/2	1/2	6	–	99768.0	*
87	13/2	3/2	8	–	121702.7	*
88	13/2	1/2	6	–	173810.7	*

Table 4.2: *(Continued)*

Level no.	J	$\|\Omega\|$	R	ε	Energy / MHz	g-factor
89	15/2	3/2	7	+	-57867.0	*
90	15/2	1/2	9	+	-5859.6	*
91	15/2	3/2	8	–	10148.9	*
92	15/2	1/2	6	–	89806.3	*
93	15/2	3/2	8	–	133237.7	*
94	17/2	3/2	9	+	-11165.8	*
95	17/2	1/2	8	–	5399.6	*
96	17/2	3/2	10	–	45553.4	*
97	17/2	1/2	7	+	93583.6	*
98	17/2	3/2	9	+	128186.4	*
99	19/2	3/2	9	+	5077.2	*
100	19/2	3/2	10	–	70185.7	*
101	19/2	3/2	10	–	174394.0	*
102	21/2	3/2	12	–	-71416.5	*

4.3 Detailed discussion of the experimental energy level diagram

The experimentally determined energy level diagram (Figure 4.5) spans > 10.2 cm^{-1}. The correct orientation of the diagram with respect to the dissociation limit was determined using two complimentary methods – one experimental and one theoretical. It was generally found that the larger the electric field dissociation voltage needed to observe a transition, the lower down the well the transition is located. Thus transitions that link levels nearest to dissociation were seen with low electric field dissociation voltages, typically 0.5 kV, transitions in the middle manifolds were observed with 2.5 kV and those at the bottom of the diagram were recorded with dissociation voltages of 3.5 kV. This agrees with the theory of electric field dissociation as discussed in Section 1.2.2. In addition is the observation that the levels near to the top of the diagram indicate the expected convergence towards the dissociation limit of the molecule.

It has been possible to dissociate levels down to level 83. This indicates that the electric field is able to dissociate levels lying 7.37 cm^{-1} (221091.9 MHz) into the potential well, although it is not possible to measure the dissociation energies of levels directly. This compares with electric field penetrations of approximately 1.5 cm^{-1} in $HeAr^+$ [34] and 0.5 cm^{-1} in $HeKr^+$ [35].

The first part of the experimental energy level diagram to be formed was that at low J. To assign absolute parity to this network the experimentally determined g-factors of the $J = 1/2$ levels were compared with the limiting case (c) / case (e) values listed in Tables 2.1 and 2.2. As noted previously, these values are the same for both coupling cases, and therefore studying the $J = 1/2$ levels is useful only to determine the absolute parity assignment, not the coupling case. Since there are no $|\Omega| = 3/2$ levels for $J = 1/2$, $|\Omega| = 1/2$ levels to mix with, then it is reasonable to assume that the $J = 1/2$ levels will have g-factors very close to the limiting values. The three $J = 1/2$ levels labelled 2, 4 and 6 have measured g-factors -1.340, -1.330 and -1.394 respectively. Comparing these values with the two possible limiting g-factors (-1.334 for u states and 2.224 for g states) it is immediately apparent that these values are very close to the u-state limiting value. These levels must therefore be of u symmetry. It is known that the four remaining $J=1/2$ levels are of opposite parity and must therefore be of g symmetry. There are, however, major discrepancies between the expected and measured g-factors for these levels, *i.e.* levels 1, 3 and 5 have g-factors 1.945, 1.437 and 2.2 respectively, compared with the limiting value of 2.224. (Note that it has not been possible to measure the g-factor of level 7 since none of the transitions attached to it have been observed "single photon"). The reason for this discrepancy was not clear until the network was quite large and patterns had emerged. It became apparent that five levels (3, 13, 28, 49 and 65) occurred in regions of the diagram where levels were not expected. They also exhibited a distinctly different pattern to other levels in the diagram. This pattern is characteristic of a vibrational progression with a significantly larger rotational constant than neighbouring levels and the rotational structure is not characteristic of case (c). It was thus concluded that these levels correspond to a vibration with significantly shorter bond length and therefore it is likely that they belong to the inner well of the I $(1/2)_g$ state (as shown in Figure 4.2). The effect of these inner-well levels on the levels supported by the outer

well (and *vice versa*) is determined by the width and height of the barrier in the potential. It may be seen from Figure 4.5 and Table 4.2 that the inner-well levels appear to be responsible for a number of local perturbations to both the energies and the *g*-factors of nearby levels. It is therefore concluded that the outer-well level 1 has a significantly perturbed *g*-factor (1.945) due to the presence of the inner-well level 3, which itself is highly perturbed (g = 1.437) by the presence of level 1. Level 5, however, is perturbed only slightly and so its measured *g*-factor (2.2) is much closer to the limiting case value of 2.224. It is predicted that the *g*-factor of level 7 will be very close to this limiting value. The inner well will be discussed in detail in Section 4.4.5.

Comparison of the experimentally determined *g*-factors for some of the lowest J levels with the theoretical values in Tables 2.1 and 2.2 indicates that it is meaningful to make an assignment using a Hund's case (c) basis set. Table 4.2 therefore includes an $|\Omega|$ assignment for the majority of the 102 levels, however some of the *g*-state rotational progressions nearest to dissociation are not sufficiently well established to be sure of the assignment and these levels are marked *.

The *g* and *u* electronic states have similar long-range behaviour and since this is likely to dominate the bonding near dissociation, it is expected that they would exhibit similar energy level patterns. Figure 4.6 shows the five most complete experimentally observed progressions (3 *u* state and 2 *g* state), and for clarity the *u* and *g* states have been displayed separately. It may be seen from Figure 4.6 that for both *g* and *u* states the vibronic states are grouped in pairs that exhibit clear rotational progressions, as would be expected in a case (c) basis. Figure 4.6 also shows that for both the *g* and *u* states the $|\Omega| = 3/2$ progressions are simple, *i.e.* as J increases there is an increase in the levels' energies. The $|\Omega| = 1/2$ progressions have a more complicated structure, displaying an alternating increase / decrease in energy as J increases. This is a consequence of the Ω doubling that was explained in Section 2.4.2.

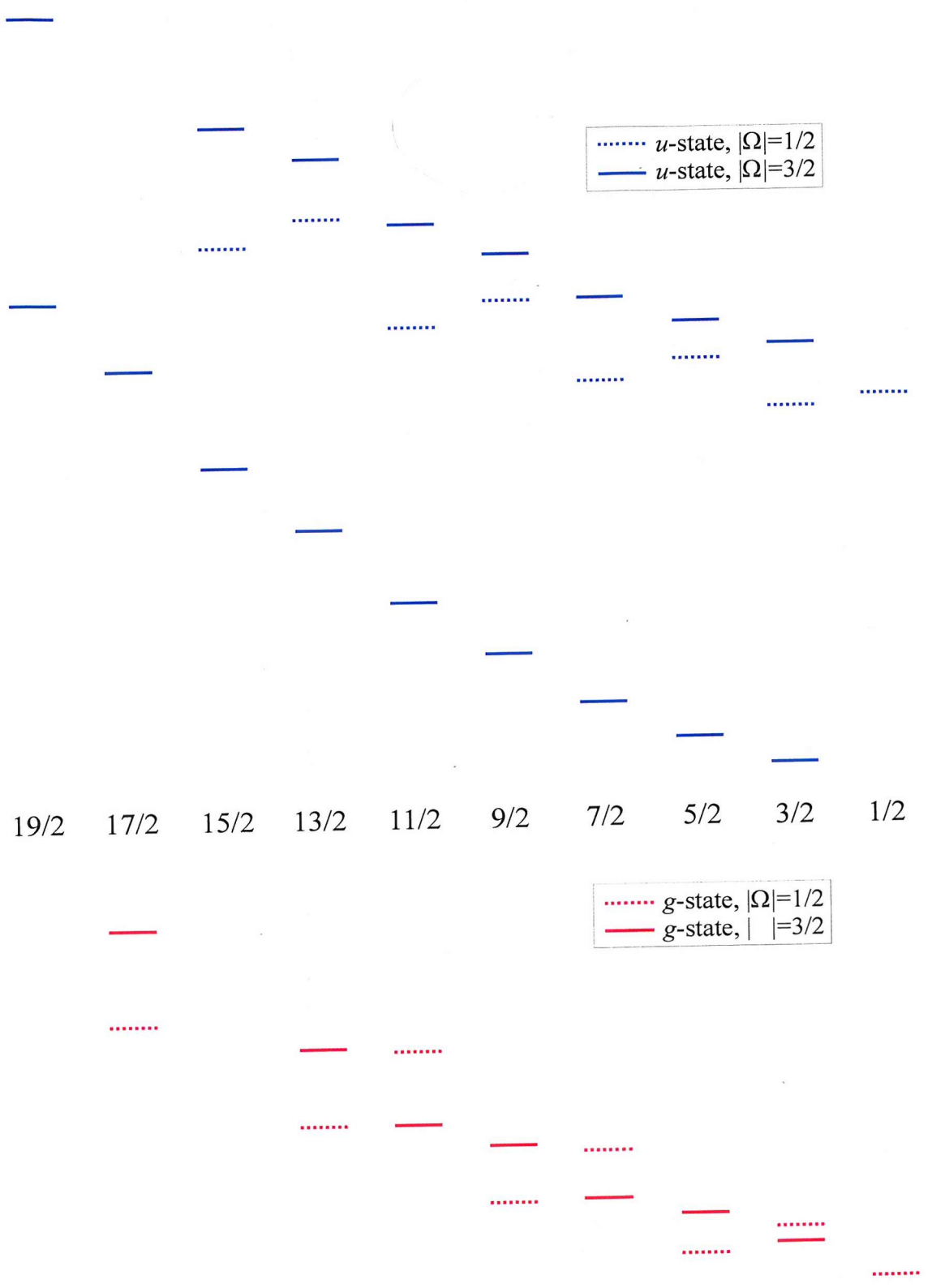

Figure 4.6: Section of the experimental energy level diagram for Ne_2^+, showing the patterns in the $|\Omega| = 1/2$ and 3/2 rotational progressions (for clarity the *g* and *u* states have been displayed separately).

4.3.1 Rotational-electronic coupling – the transition to case (e)

Whilst Hund's case (c) is the best description for the lowest J levels, inspection of the g-factors of higher J levels indicates a significant departure from case (c) and case (e) becomes a better description. Case (e) represents the high-rotation limit of case (c), in which the coupling between rotational and electronic motion dominates, and the Born-Oppenheimer approximation is no longer valid. The theory of this coupling was outlined in Section 2.4.2.

Table 4.3 compares the measured g-factors for all outer-well $J > 1/2$ levels with the relevant limiting case (c) and case (e) values. The final column quantifies the amount of case (c) / (e) character of each level, where the spread of possible g-factors between these two limiting values has been mapped onto the interval 0–1. Thus 0.00 represents pure case (c), 1.00 represents pure case (e). There are a few g state levels that have mapped values outside the range 0–1, for example levels 46 and 50. These values are attributed to perturbations by nearby inner-well levels. In general, $J = 3/2$ and $J = 5/2$ levels are closer to case (c) but levels $J > 7/2$ are generally better described by case (e). There are some exceptions to this rule, for example the $J = 3/2$ levels 18, 19 and 20 are better described by case (e) whilst the $J = 7/2$ levels 42 and 44 are slightly closer to case (c) than case (e). Thus it may be concluded that the transition to case (e) occurs not only with increased rotation, but also as dissociation is approached. This is because the levels in this area of the diagram are very close together and the mixing by the rotational Hamiltonian is significant, even though the rotational constant is small. It is expected that levels with $J > 13/2$ will have significant case (e) character. However, although some high J Zeeman patterns have been recorded, they were often high frequency transitions. As described in Section 3.6.2, this means that the microwave modes were such that only $\Delta M_J = 0$ patterns were observed, from which only Δg for the levels involved can be determined, not their absolute values.

Table 4.3: Comparison of measured *g*-factors with pure case (c) and case (e) limiting values. *Figures in bold indicate which of the coupling cases more appropriately describes that level. † See text for explanation of the final column.

Level number	J	measured *g*-factor	pure case (c)*	pure case (e)*	Mapped onto scale 0–1†
8	3/2	0.781	**0.800**	0.267	0.04
9	3/2	0.732	**0.800**	0.978	-0.38
10	3/2	-0.511	**-0.623**	-0.800	-0.69
11	3/2	0.925	**0.800**	1.334	0.23
12	3/2	0.676	**0.800**	0.267	0.23
15	3/2	1.043	**0.800**	1.334	0.46
16	3/2	-0.655	**-0.623**	-0.800	0.18
18	3/2	0.980	0.800	**0.978**	1.01
19	3/2	1.159	0.800	**1.334**	0.67
20	3/2	0.476	0.800	**0.267**	0.61
24	5/2	0.635	**0.496**	0.800	0.46
25	5/2	0.181	0.343	**0.038**	0.53
26	5/2	-0.071	**-0.419**	0.496	0.38
27	5/2	0.000	**0.343**	-0.572	0.38
29	5/2	0.475	**0.496**	0.800	-0.07
30	5/2	0.277	**0.343**	0.038	0.22
31	5/2	0.322	-0.419	**0.496**	0.81
32	5/2	-0.397	0.343	**-0.572**	0.81
33	5/2	0.772	0.496	**0.800**	0.91
34	5/2	0.471	-0.419	**0.496**	0.97
35	5/2	-0.541	0.343	**-0.572**	0.97
41	7/2	0.293	0.191	**0.318**	0.80
42	7/2	0.464	**0.360**	0.572	0.49
43	7/2	-0.406	-0.318	**-0.445**	0.69
44	7/2	0.090	**0.191**	-0.021	0.48
46	7/2	-0.226	**-0.318**	-0.445	-0.72

Table 4.3: (*Continued*)

Level number	J	measured g-factor	pure case (c)*	pure case (e)*	Mapped onto scale 0–1†
47	7/2	0.508	0.360	**0.572**	0.70
48	7/2	0.052	0.191	**-0.021**	0.66
50	7/2	0.153	**0.191**	0.318	-0.30
51	7/2	0.543	0.360	**0.572**	0.86
52	7/2	0.000	0.191	**-0.021**	0.90
57	9/2	0.397	0.283	**0.445**	0.70
58	9/2	0.000	0.121	**-0.040**	0.75
59	9/2	0.073	-0.256	**0.229**	0.68
60	9/2	-0.211	0.121	**-0.364**	0.69
61	9/2	0.360	**0.283**	0.445	0.48
67	9/2	0.204	-0.256	**0.229**	0.95
74	11/2	0.305	0.233	**0.364**	0.55
76	11/2	0.000	0.084	**-0.047**	0.64
78	11/2	0.333	0.233	**0.364**	0.76
82	11/2	-0.028	0.084	**-0.047**	0.86
84	13/2	0.284	0.198	**0.308**	0.78

The case (e) coupling case is characterised by four levels of consecutive J having the same R value and same energy (except for low J when there is only one $R = 0$ level, and three $R = 1$ levels). In a similar style to Figure 4.6, Figure 4.7 shows four experimentally observed vibrational progressions of Ne_2^+ described by the case (e) label R. For example, the four $R = 3$ levels will have J values 3/2, 5/2, 7/2 and 9/2 and, as can be seen from Figure 4.7, they have approximately the same energies. It can also be seen from Figure 4.7 that the g-states appear to show more case (e) character than the u-states; an observation also indicated in Table 4.3. This is because in the g-states the $|\Omega| = 1/2$ and $|\Omega| = 3/2$ vibrations overlap each other, whereas they remain separate in the u-states (Figure 4.6). This results in greater mixing of the rotational Hamiltonian for g states, which is therefore more like case (e).

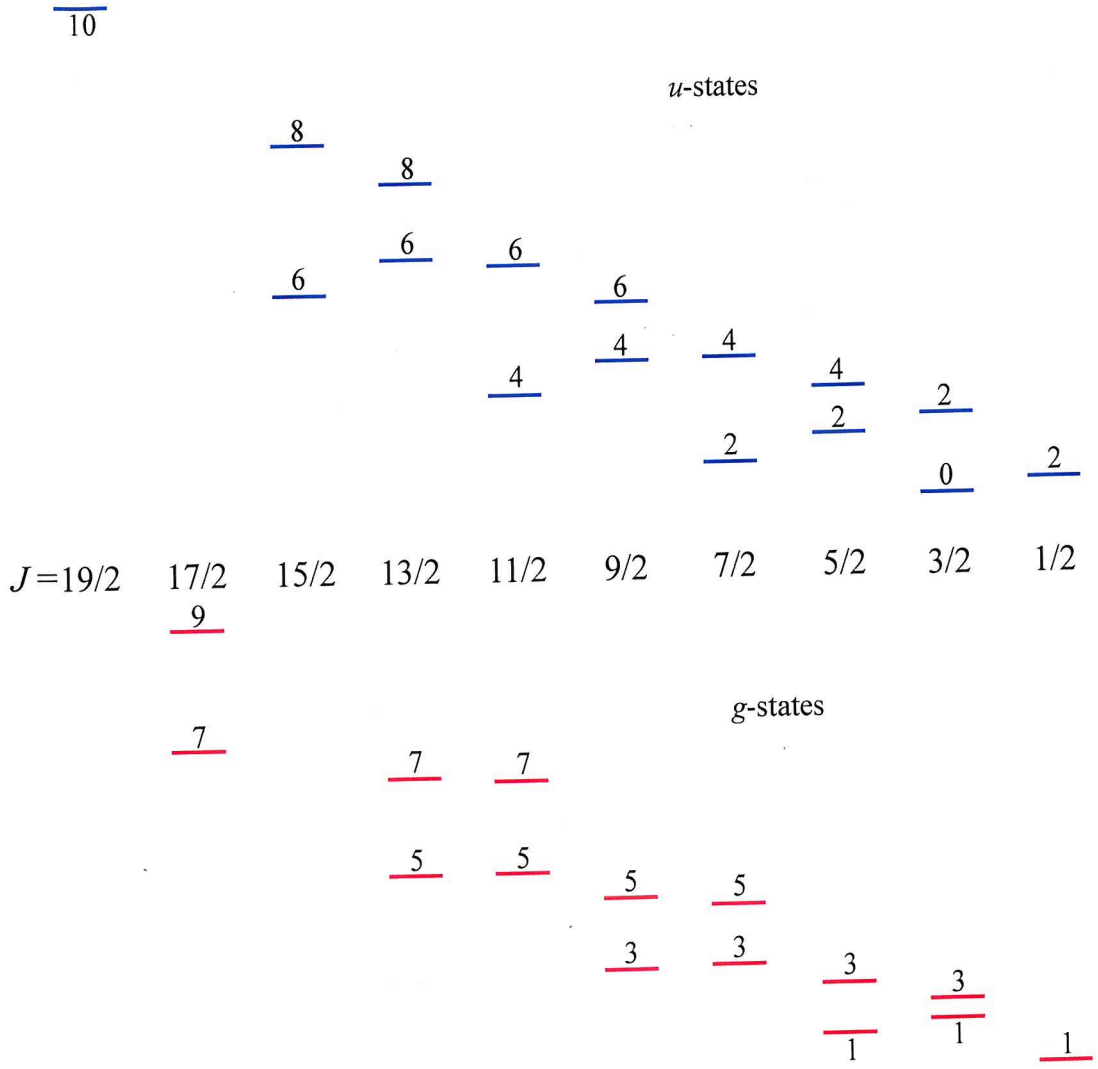

Figure 4.7: Section of the experimental energy level diagram for Ne_2^+, showing the case (e) patterns in R. Labels are values of R (for clarity the g and u states have been displayed separately).

It has been demonstrated that Figure 4.5 can be interpreted in both a case (c) and case (e) basis but in general the long-range $Ne\cdots Ne^+$ complex is intermediate between case (c) and case (e) coupling schemes. Whilst the observed states exhibit more case (e) character than the previously studied $HeAr^+$ [34], they have significantly less case (e) character than $HeKr^+$ [35]. These comparisons can be shown on a "Hund's line" [85] (Figure 4.8), which utilises the mapping procedure described above.

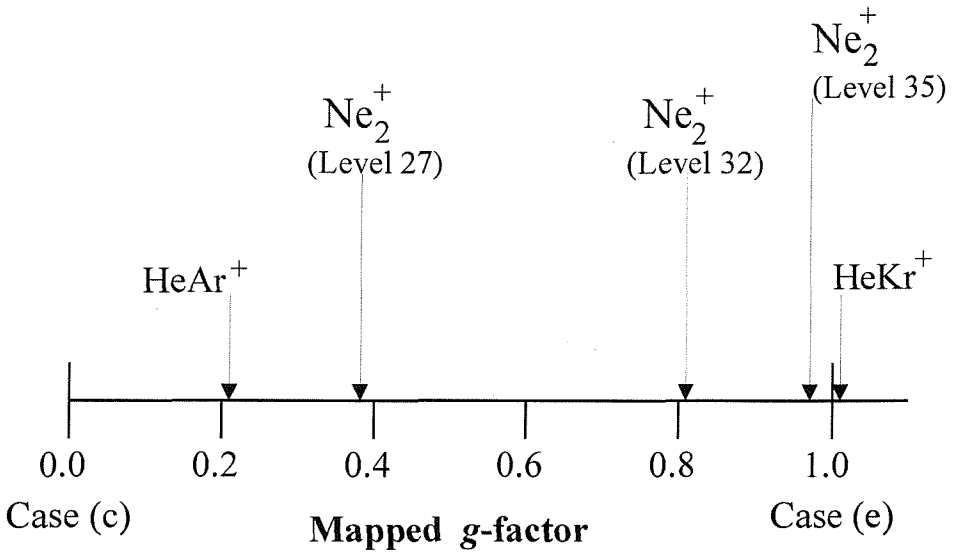

Figure 4.8: A "Hund's line" [85] comparing the case (c) / (e) character of selected negative parity $J = 5/2$ levels in $HeAr^+$, $HeKr^+$ and Ne_2^+. These levels are described by $|\Omega| = 3/2$ or $R = 4$, whichever is more appropriate.

4.4 Coupled channel calculations

Whilst the observations described in Section 4.3 are most useful and interesting, the stated ultimate aim of this study is to gain an understanding of the long-range interactions between a neon atom and a neon ion. The positions of levels near to a dissociation limit are clearly very sensitive to the behaviour of the interaction potential at long range. The energies of these levels are also (in principle) dependent on the energies of all other more strongly bound energy levels, and therefore their properties are actually sensitive to the shape of the *entire* interaction potential. A comprehensive study of states near to dissociation (*i.e.* the current study) should therefore provide enough information to enable an accurate determination of the interaction potential (at both short and long range) to be performed.

Carrington *et al.* have previously been successful at deriving the entire interaction potential for $HeAr^+$ [34] and $HeKr^+$ [35] by using spectroscopic data of the near-dissociation levels. However, the interaction potentials for these complexes are much shallower than for Ne_2^+ because the dominant long-range interaction, C_4, is

1.335 a_0^3 for Ne whereas for He it is only 0.691 a_0^3. The larger C_4 coefficient and the increased reduced mass means that the $Ne\cdots Ne^+$ potential will support a larger number of vibrations in the long-range regions and this presents a significant challenge for the coupled channel calculations which will now be described.

4.4.1 Coupled channel theory

It is possible to model the experimental energy level pattern with an effective Hamiltonian analysis [85] and whilst this approach works relatively well for the u states it was found to be very difficult to model the inner-well levels and resulting perturbations in the g-state. Additionally, this approach does not include the effects of rotational-electronic coupling, nor does it provide accurate information for vibronic states that have not been experimentally observed.

Thus although an effective Hamiltonian analysis was used during the early stages in the investigation and was useful in predicting the positions of new levels, it is preferable to use coupled channel calculations that take into account all off-diagonal matrix elements. Such calculations allow the determination of a full set of potential curves for Ne_2^+ by using a combination of experimental observations and previous theoretical knowledge.

The Hamiltonian for a molecular ion such as Ne_2^+ may be written as

$$\mathcal{H} = -\frac{\hbar^2}{2\mu} r^{-1} \frac{d^2}{dr^2} r + \frac{\hbar^2}{2\mu r^2} \mathbf{R}^2 + \mathcal{H}_{SO}(r) + V(r, \mathbf{r}_a), \qquad (4.3)$$

where the operator $\mathbf{R}^2$ is the angular momentum operator for rotation of the nuclear framework. The interaction potential $V(r, \mathbf{r}_a)$ is a function of both the internuclear distance, r, and the electron coordinates $\mathbf{r}_a$. The spin-orbit coupling operator $\mathcal{H}_{SO}$ is, in principle, a function of r.

The bound-state eigenvalues are normally found by using matrix methods in which all degrees of freedom are handled by basis set expansions. However, since the states investigated in this work lie close to the dissociation limit, it is difficult to represent the radial wavefunction using a basis set expansion. The bound state problem is therefore solved using the coupled channel approach, in which the radial

coordinate (r) is handled by direct numerical propagation on a grid and all other coordinates by a basis set expansion.

The total wavefunction for the molecular ion may be written as

$$\Psi = r^{-1} \sum_{LSJ_aR} \psi^{JM_J}_{LSJ_aR} \chi^{\in J}_{\eta;LSJ_aR}(r), \tag{4.4}$$

where $\psi^{JM_J}_{LSJ_aR}$ form a case (e) basis set and the radial channel functions, $\chi^{\in J}_{\eta;LSJ_aR}(r)$, can take any form needed to satisfy the Schrödinger equation. For the purposes of these calculations, the expansion (Equation 4.4) is truncated to include only the three electronic states that correlate with the $^2P_{3/2}$ and $^2P_{1/2}$ states of Ne_2^+, since couplings to higher electronic states are very small. In this approximation, the interaction may be written $V(r, \theta_a)$, where θ_a is the angle describing the location of the p-electron hole of the Ne^+ ion (relative to the internuclear vector). It should be noted that this two-dimensional *interaction potential* is distinct from the Hund's case (a/c) *potential curves* which are defined by the inclusion of spin-orbit coupling.

4.4.2 Representation of the interaction potential

Since ^{20}Ne does not possess nuclear spin (*i.e.* $I(^{20}Ne) = 0$), there are no terms in the molecular Hamiltonian to break the electronic symmetry. Any calculations performed to represent the interaction potential for the species $^{20}Ne_2^+$ can therefore be separated into two problems; one of g- and one of u- symmetry. The long-range coefficients for both the g- and the u- states are expected to be the same, and therefore performing two independent calculations will provide two useful estimates of these parameters.

The interaction potential for Ne_2^+ may be represented as a single two-dimensional surface, which is a function of r and θ_a. The surface may be expressed as an expansion in Legendre polynomials,

$$V(r, \theta_a) = V_0(r) + V_2(r) P_2(\cos\theta_a). \tag{4.5}$$

This representation is convenient for potential fitting since $V_0(r)$ and $V_2(r)$ have identifiably different long-range behaviour: $V_0(r)$ represents the isotropic contribution

and $V_2(r)$ the anisotropic contribution to the interaction potential. Although $V_0(r)$ and $V_2(r)$ give a good understanding of the long-range interactions, they do not allow for intuition with the short-range terms, which are critical in determining much of the potential shape. It was therefore deemed more convenient to re-parameterise the problem into the spin-free Σ and Π representations which allow greater intuitive control of the short-range terms, although the relationship between the isotropic and anisotropic long-range terms becomes more complicated. The newly parameterised representations [in a case (a) basis] are related by the simple expressions [34]:

$$V_\Sigma(r) = V_0(r) + \frac{2}{5}V_2(r) \tag{4.6}$$

$$V_\Pi(r) = V_0(r) - \frac{1}{5}V_2(r).$$

The addition of spin-orbit coupling results in the following expressions for the adiabatic spin-orbit coupling curves:

$$V_{\Sigma_{\frac{1}{2}}}(r) = \frac{V_\Sigma(r) - V_\Pi(r)}{2} + \frac{\Delta}{2} - D(r), \tag{4.7}$$

$$V_{\Pi_{\frac{3}{2}}}(r) = V_\Pi(r),$$

$$V_{\Pi_{\frac{1}{2}}}(r) = \frac{V_\Sigma(r) + V_\Pi(r)}{2} + \frac{\Delta}{2} + D(r),$$

where Δ is the splitting between the atomic spin-orbit states (782cm^{-1} [84]) and is assumed to be the same as in the molecular ion, and

$$D(r) = \frac{1}{2}\sqrt{\Delta^2 + \left[V_\Sigma(r) - V_\Pi(r)\right]^2 - \frac{2}{3}\Delta\left[V_\Sigma(r) - V_\Pi(r)\right]}. \tag{4.8}$$

Previous studies of ionic complexes by Carrington *et al.* have employed a Morse function for the representation of the short-range region of the potential, with both

isotropic and anisotropic contributions to the long-range tail (MAL – Morse + Anisotropic Long range). The same functional form was employed for the spin-free potentials for Ne_2^+:

$$V_\Lambda(r) = A_\Lambda(1-a_\Lambda)\exp[-\beta_\Lambda(r-r_{e_\Lambda})] + A_\Lambda a_\Lambda \exp[-\frac{1}{2}\beta_\Lambda(r-r_{e_\Lambda})] - \sum_{n=4,6,8,10} \frac{[C_n]_\Lambda D_{n_\Lambda}(r)}{r^n}, \quad (4.9)$$

where $D_{n_\Lambda}(r)$ are Tang-Toennies damping functions [86] that prevent the inverse power terms dominating at short range, and have the form

$$D_{n_\Lambda}(r) = 1-\exp(-\beta_\Lambda r)\sum_{m=0}^{n}\frac{(\beta_\Lambda r)^m}{m!}. \quad (4.10)$$

The subscript Λ takes the values Σ and Π as required. The parameters used in the fitting process were chosen to be intuitive (*i.e.* either experimental or theoretical knowledge constrained them to sensible values).

For large internuclear distances *r*, the interaction potential between an atom and an ion can be expressed through a multipole expansion. The dominant interaction in Ne_2^+ is the charge / induced-dipole (r^{-4}) interaction which is purely isotropic and represented by the expression $[C_4]_0$ where the subscript 0 denotes its isotropic nature. The value of this interaction is determined only by α^d_{Ne}, the dipole polarisability of the neon atom,

$$[C_4]_0 = \frac{e^2\alpha^d_{Ne}}{2} = 1.335\ e^2a_0^3, \quad (4.11)$$

where α^d_{Ne} is 2.67 a_0^3 [87]. Since the r^{-4} interaction is purely isotropic, *i.e.* $[C_4]_2 = 0$, then the value of $[C_4]$ is the same for both the Σ and Π states, *i.e.* $[C_4]_\Sigma = [C_4]_\Pi =$

1.335 $e^2a_0^3$. These constants are well established, and were therefore fixed during the fitting process.

The r^{-6} interaction has both isotropic and anisotropic components. The isotropic $[C_6]_0$ coefficient has a contribution from both the charge / induced-quadrupole and isotropic dispersion interactions,

$$[C_6]_0 = \frac{e^2\alpha^q_{\mathrm{Ne}}}{2} + [C_6]^{(0)}_{\mathrm{disp}}, \tag{4.12}$$

where the quadrupole polarisability of the neon atom, α^q_{Ne}, is known to be 6.422 a_0^5 [88]. The isotropic dispersion interaction, $[C_6]^{(0)}_{\mathrm{disp}}$ may be estimated using a simple Slater-Kirkwood calculation [89],

$$[C_6]^{(0)}_{\mathrm{disp}} = \frac{3e^2\sqrt{a_0}\,\alpha^d_{\mathrm{Ne}}\alpha^d_{\mathrm{Ne}^+}}{2\left(\sqrt{\alpha^d_{\mathrm{Ne}}/6} + \sqrt{\alpha^d_{\mathrm{Ne}^+}/5}\right)} = 4.48\ e^2a_0^5, \tag{4.13}$$

where the dipole polarisability of Ne^+, $\alpha^d_{\mathrm{Ne}^+}$, is 1.32 a_0^3 [78]. $[C_6]_0$ is therefore estimated to be 7.69 $e^2a_0^5$ and was held at this value throughout the calculations.

The r^{-6} anisotropic contribution is more difficult to estimate since it arises from two different sources. Firstly, the Ne^+ ion is in a P state, and thus has a quadrupole moment along the axis of the partially filled p orbital. The dipole moment induced on the Ne atom by the ionic charge can then interact with this quadrupole moment. The second contribution to $[C_6]_2$ arises from the fact that the polarisability of Ne^+ is different in directions parallel and perpendicular to the axis of the unpaired p orbital, so that the dispersion interaction is anisotropic. The anisotropic C_6 coefficient may be written

$$[C_6]_2 = 3e\alpha^d_{\mathrm{Ne}}\Theta_{\mathrm{Ne}^+} + [C_6]^{(2)}_{\mathrm{disp}}, \tag{4.14}$$

where Θ_{Ne^+}, the quadrupole moment of Ne^+, is known to be 1.122 ea_0^2 [90]. The anisotropic dispersion term is not known but is expected to be smaller than the induction term, and of opposite sign [34]. It is therefore possible to place an upper bound of 8.99 $e^2a_0^5$ on the anisotropic $[C_6]_2$ term. Similarly, the upper and lower bounds of the $[C_6]$ coefficients are estimated to be $7.69 < [C_6]_\Sigma < 11.29\ e^2a_0^5$ and $5.89 < [C_6]_\Pi < 7.69\ e^2a_0^5$.

Instead of being restrained, the C_8 coefficients are derived during the fitting process so as to provide the correct well depth, D_e, and equilibrium bond length, r_e. However, it is useful to estimate their values to ensure that the derived values are feasible. From the previous studies of $HeAr^+$ and $HeKr^+$ by Carrington *et al.* [34, 35], it was observed that the C_8 coefficients derived for the ion were similar to those for the corresponding neutral species. The calculations of Standard and Certain [88] suggest that the C_8 coefficients for $^{20}Ne_2$ should fall in the range $55.5 < C_8 < 96.5\ e^2a_0^7$ and it is expected that this will also be true for Ne_2^+.

Further, in the previous studies of $HeAr^+$ and $HeKr^+$ it was observed that the C_{10} coefficients are highly correlated with the other parameters in the fit and it is likely that they will be undetermined in this study also. Therefore the ratio $\gamma = C_{10} / C_8$ was held fixed at 11 a_0^2, a value predicted by the single oscillator formula of Thakkar and Smith [91],

$$\frac{C_{10}}{C_8} = \frac{49}{40}\frac{C_8}{C_6}. \qquad (4.15)$$

This uses the lower bounds of the C_6 and C_8 coefficients of Standard and Certain [88] for the neutral species Ne_2. This is a rather crude estimation, although it is likely to be sufficient for the current purpose, since the experimental data is fairly insensitive to this ratio.

4.4.3 Fitting of the experimental data

A starting point for fitting the interaction potential was achieved by fitting the functional form to the *ab initio* calculations of Naumkin and Wales [83], together with the estimation of the long-range parameters (Section 4.4.2). The bound rovibrational

levels supported by these potentials were calculated using the coupled channel theory implemented in the program BOUND [92]. It was then possible to incorporate the extensive photoelectron data of Hall *et al.* [74] by changing the values of the parameters by very small amounts. As discussed in Section 4.1, there was some uncertainty about the absolute vibrational assignment of this photoelectron data, and the authors' best estimate was that the lowest observed level was $v = 2$. However, it was found in the current work that assuming the lowest observed level to be $v = 3$ gives the best agreement with the *ab initio* results of Naumkin and Wales [83]. This reassignment alters the constants of Hall *et al.* to be $D_0 = 1.362 \pm 0.01$ eV, $\omega_e = 584.3 \pm 3.6$ cm^{-1} and $\omega_e x_e = 7.4 \pm 0.2$ cm^{-1}. These new values also give very satisfactory agreement with the Rydberg data of Kim *et al.* [75] ($\omega_e = 586.0 \pm 2.0$ cm^{-1} and $\omega_e x_e = 5.4 \pm 0.8$ cm^{-1}), the remaining discrepancy in the $\omega_e x_e$ values probably arising from the very small data set of Kim *et al.*

Thus this first set of potentials agreed with both the best experimental and theoretical work available to date. It was found, however, that there were *many* potential curves that correctly predicted the levels at the bottom of the well to within the experimental error. This was not altogether unexpected, nor was it surprising that the predicted patterns of energy levels in the 10 cm^{-1} nearest to dissociation did not replicate the experimental data of the current study. (It is for exactly this reason that the current experimental study is such a sensitive determination of accurate potential energy curves).

This initial fit was therefore used as a starting point, and the near-dissociation data from the current study was used to refine the curves further. The first challenge in this refinement is to approximately recreate the observed pattern of near-dissociation levels. This is achieved by careful manipulation of the interaction potential, generally only requiring very small changes to the $\mathscr{E}_\Lambda$, $r_{e\Lambda}$ and β_Λ parameters. However, a number of different vibrational assignments for the *u*-state gave approximate agreement with the experimental data, and ultimately each of these needed to be fully investigated to ensure the fit closest to experiment was chosen. It was considerably more difficult to find a suitable starting point for the *g*-state fit due to the added constraints of fitting the double minimum of the I $(1/2)_g$ state. However this initial difficulty transpired to be a distinct advantage, since once initial starting

points were found, only a few alternative node assignments needed to be explored. The presence of the inner-well levels therefore proved to be a very useful constraint on possible node assignments.

The experimental data that was included in the fit was chosen to have a well-balanced representation of all types of data over the entire range of J quantum numbers. For each vibrational progression, combinations of experimental energy level spacings were chosen to represent the relative vibrational level spacings, rotational spacings (including simple centrifugal terms) and terms responsible for the Ω-doubling. Previous studies have found that including g-factors in the data set is unnecessary during the initial stages of the fit.

The fits to both the g- and u- states were determined using an interactive nonlinear least-squares fitting procedure implemented in the I-NoLLS package [93]. The interactive nature of the code permits rapid and flexible control over the progress of the fit and allows the user to apply physical insight when choosing parameter steps. This results in speedy convergence to physically reasonable solutions and was found in previous studies to be a highly effective method for fitting near-dissociation spectroscopic data [34, 35].

4.4.4 The final interaction potential

Once the calculated potentials for both the g- and u-states recreated the observed patterns with fair accuracy, the two halves of the problem were integrated. It was then possible to compare predicted transition frequencies with those observed, rather than just the spacings within either the g- or the u-state. The first good fit used data from the first 85 levels discovered; this was then extended to higher J as more levels were attached to the network. The root mean squared (rms.) deviation for the transitions used to construct this initial experimental network was 297 MHz, the majority of this error arising from the poor determination of the lowest $\Omega = 3/2$ vibrational progression in the u-state. (The error in the transition frequencies to levels in this rotational progression were of the order 1 GHz). Whilst the separations between the levels (and hence the rotational spacings) were well produced by the interaction potential, the absolute binding energies were not quite correct.

The sternest test of such calculations is the ability to predict the positions of levels not yet observed and despite the significant errors, this initial fit was good enough to guide the search for new levels. A further 12 *g*- and 5 *u*-state levels were successfully predicted, their positions being confirmed by double resonance experiments. Table 4.4 shows these 17 levels and also the goodness of the fit.

There is no obvious pattern to the size of the errors in the predictions. For example, level 89 is part of a little observed vibration, yet the error in the prediction is less than that to level 98 which belongs to a very well characterised progression. Neither are the predictions to levels of one parity any better than those to the other. The root-mean-squared error of the calculations is 299 MHz.

Using an iterative process with every new level observed, it was found that one particular set of parameters gave the most consistent description of all the experimentally found levels, up to and including $J = 21/2$. This set of parameters is detailed in Table 4.5 and it may be seen that (with the exception of the a_Λ and β_{Π} parameters) the short-range parameters are well determined. For both the *g*- and the *u*-state, the parameters are highly correlated (see Table 4.6), demonstrated by the physically unreasonable sign and values of the C_8 coefficients. A detailed discussion of the long-range parameters will be given in Section 4.4.5.

Extending this fit to $J = 25/2$ predicts a unique assignment for a further 31 of the 74 unassigned transitions, with a rms. deviation of 297 MHz. It is recommended that future experiments be performed to check some of these predictions, thus providing a useful test for the quality of the fitted potential and allowing for further refinement of the potentials. Assuming these assignments to be correct, there remain 43 observed transitions for which the coupled channel calculations cannot provide unique fits. Some of these are surely attached to the experimental network of levels, although none have yet been successfully assigned.

Level no.	Energy (Experimental) / MHz	Energy (Calculated) / MHz	Difference / MHz
7	208508.7	207564.0	944.7
21	203106.2	203381.6	275.4
22	207276.9	207489.3	212.4
39	207385.8	207595.4	209.6
54	203446.0	203681.1	235.1
68	197498.1	197670.5	172.4
89	-57867.0	-57652.8	214.2
90	-5859.6	-5919.2	59.6
94	-11165.8	-11153.8	12.0
95	5399.6	4855.1	544.5
96	45553.4	45446.2	107.2
97	93583.6	93492.6	91.0
98	128186.4	128457.0	270.6
99	5077.2	5352.6	275.4
100	70185.7	69978.1	207.6
101	174394.0	174401.0	7.0
102	-71416.5	-71383.7	32.8

Table 4.4: Levels found with the aid of the calculations – experimental and calculated.

		g states		*u* states	
Parameter	Units	Value	95 % conf.	Value	95 % conf.
ε_Σ	mE_h	0.128117	0.000365	51.997130	0.674786
ε_π	mE_h	5.792196	0.014511	0.510428	0.032491
$r_{e\Sigma}$	a_0	9.212993	0.006860	3.195730	0.07218
$r_{e\Pi}$	a_0	4.193729	0.004235	6.315226	0.111942
β_Σ	a_0^{-1}	2.417502	0.00827	2.305779	0.048446
β_Π	a_0^{-1}	2.476164	0.022252	2.549226	0.599878
a_Σ	-	1.0	Fixed	1.87816	0.671526
a_Π	-	4.846694	3.070511	0.879177	0.169900
$[C_4]_\Sigma$	$e^2a_0^3$	1.335	Fixed	1.335	Fixed
$[C_4]_\Pi$	$e^2a_0^3$	1.335	Fixed	1.335	Fixed
$[C_6]_\Sigma$	$e^2a_0^5$	9.112339	1.569079	11.371651	6.998988
$[C_6]_\Pi$	$e^2a_0^5$	5.955124	0.907559	6.25788	3.323900
$[C_{10}]_\Sigma$ / $[C_8]_\Sigma$	a_0^2	11.0	Fixed	11.0	Fixed
$[C_{10}]_\Pi$ / $[C_8]_\Pi$	a_0^2	11.0	Fixed	11.0	Fixed
A_Σ	mE_h	0.081623	Derived	-5.291854	Derived
A_Π	mE_h	-1.184987	Derived	0.499013	Derived
$[C_8]_\Sigma$	$e^2a_0^7$	438.7067	Derived	-419.6579	Derived
$[C_8]_\Pi$	$e^2a_0^7$	-56.2157	Derived	203.3153	Derived

Table 4.5: Potential parameters for the final fit to the Ne_2^+ data.

	ε_Σ	ε_Π	$r_{e\Sigma}$	$r_{e\Pi}$	β_Σ	β_Π	$[C_6]_\Sigma$	$[C_6]_\Pi$	a_Σ	a_Π
ε_Σ		*-0.601*	*-0.035*	*0.348*	*0.277*	*0.323*	*-0.439*	*0.511*	-	*-0.490*
ε_Π	**0.515**		*-0.569*	*-0.280*	*0.422*	*0.061*	*-0.226*	*-0.104*	-	*0.368*
$r_{e\Sigma}$	**0.691**	**0.595**		*0.392*	*-0.772*	*-0.213*	*0.566*	*-0.011*	-	*-0.011*
$r_{e\Pi}$	**-0.942**	**-0.692**	**-0.660**		*0.209*	*-0.235*	*0.016*	*0.035*	-	*0.067*
β_Σ	**0.691**	**0.644**	**0.978**	**-0.700**		*-0.091*	*-0.782*	*-0.090*	-	*0.261*
β_Π	**-0.417**	**0.525**	**0.037**	**0.236**	**0.049**		*0.072*	*0.941*	-	*-0.876*
$[C_6]_\Sigma$	**-0.747**	**-0.514**	**-0.846**	**0.724**	**-0.801**	**0.105**		*-0.003*	-	*-0.297*
$[C_6]_\Pi$	**-0.400**	**-0.208**	**-0.079**	**0.463**	**0.128**	**0.162**	**0.243**		-	*-0.865*
a_Σ	**-0.506**	**-0.596**	**-0.959**	**0.529**	**-0.967**	**-0.200**	**0.777**	**-0.235**		-
a_Π	**-0.885**	**-0.167**	**-0.408**	**0.813**	**-0.431**	**0.751**	**0.523**	**0.379**	**0.219**	

Table 4.6: Correlation matrices associated with the fitted parameters in Table 4.5: *u*-state in **bold**, *g*-state in *italic*.

All the levels calculated by BOUND to lie within *ca.* 15 cm^{-1} of the first dissociation limit are shown in Figure 4.9. Experimentally observed levels are shown in blue (*u*) and red (*g*), whilst predicted (but currently unobserved) levels are shown as black solid (*u*) and black dashed lines (*g*). The calculated dissociation limit is also shown (by a long dotted line). This diagram shows the predicted positions of some of the levels that were expected to be observed, but have not been; most noticeably the two $J = 1/2$ *g*-state levels. The figure clearly shows the vibrations converging as dissociation is approached, and also (particularly for $J = 1/2$, 3/2 and 5/2) the marked difference in pattern between the I $(1/2)_g$ inner-well levels and the surrounding vibrations.

As mentioned in Section 4.2, the recorded Zeeman pattern for three of the unassigned transitions suggests they correlate with the upper dissociation limit and it is highly likely that other unassigned transitions do likewise. The paramaterisation presented here defines the potentials correlating with the upper dissociation limit, but BOUND is unable to locate the associated levels because they are not bound with respect to the lowest dissociation limit.

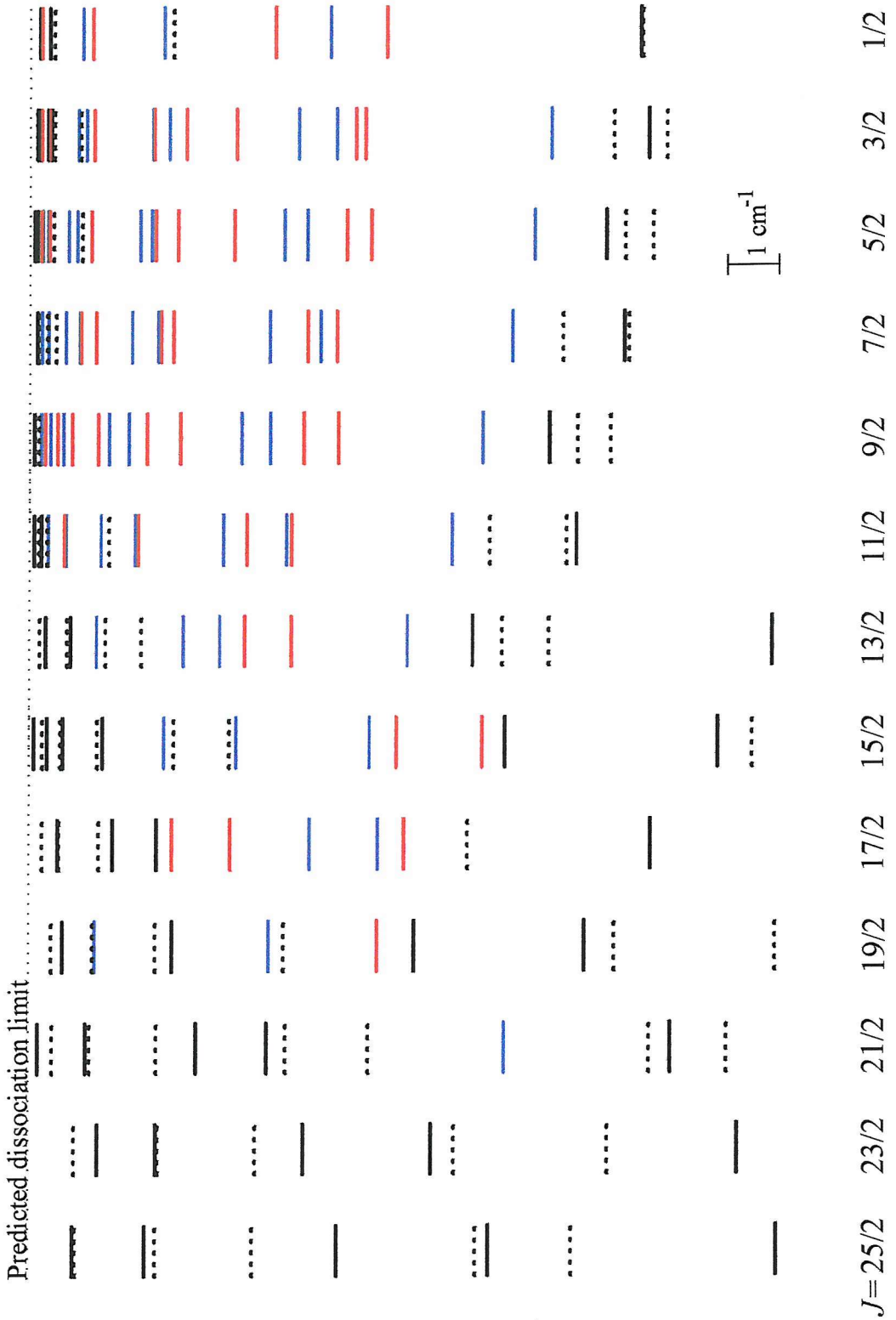

Figure 4.9: Pattern of levels (within *ca.* 15 cm^{-1} of the first dissociation limit) predicted by the BOUND calculations on the final interaction potentials of Ne_2^+. Observed levels are shown in red (*g*-states) and blue (*u*-states). Predicted levels are in black (*u*-states solid, *g*-states dashed).

4.4.5 Discussion of coupled channel results

Deriving the interaction potentials of both the *g*- and the *u*-state at all internuclear distances allows the properties of each state to be determined. The properties of the electronic states are shown in Table 4.7 and it is most interesting to compare them with previously published work. D_0 for the ground electronic state is calculated to be 1.346 eV. This is directly comparable with the earliest work on Ne_2^+ by Frommhold and Biondi [66] ($D_0 = 1.35 \pm 0.07$ eV), the scattering experiments of Mittman and Weise [69] ($D_e = 1.30 \pm 0.1$ eV) and the results of Broström *et al.* [73] (1.35 ± 0.1 eV). Most importantly, it also agrees well with the reassigned data of Hall *et al.* [74] ($D_0 = 1.362 \pm 0.01$ eV), although this is not altogether unsurprising, since the fit used this data to constrain the bottom of the potential. It is also worthwhile comparing the values of ω_e and $\omega_e x_e$ of the current work with those previously published. The current work calculates these constants to be 587.8 cm^{-1} and 7.71 cm^{-1} respectively. This value of ω_e compares well with the values of Kim *et al.* [75] (586.0 ± 2.0 cm^{-1}) and the reassigned value of Hall *et al.* (584.3 ± 3.6 cm^{-1}). However, there remains a significant discrepancy between the three calculated values of $\omega_e x_e$ (Kim *et al.* $\omega_e x_e = 5.4 \pm 0.8$ cm^{-1}, Hall *et al.* $\omega_e x_e = 7.4 \pm 0.2$ cm^{-1}). This difference may arise because (despite the large data set used for the fitting procedure) the fit to the data is not unique.

State (case (c) nomenclature)	D_e / cm^{-1}	R_e / Å	No. of bound vibrations	ω_e / cm^{-1}	B / cm^{-1} $v = 0$	$\omega_e x_e$ / cm^{-1}
I $(1/2)_u$	11244.9	1.765	44	587.8	0.5849	7.71
I $(1/2)_g$	765.3	2.212	14	194.3	0.3337	9.34
I $(3/2)_u$	112.0	3.337	10	33.8	0.1421	3.10
I $(3/2)_g$	1270.4	2.215	25	196.9	0.3351	8.46
II $(1/2)_u$	261.0	3.10	-	-	-	-
II $(1/2)_g$	63.0	3.90	-	-	-	-

Table 4.7: Characteristics of the lowest electronic states of Ne_2^+ (this work).

It is also possible to calculate the average bond length of each of the observed levels. For this study, it is most interesting to calculate this for the levels lying closest to dissociation. Level 71, the highest lying *u*-state level, has a calculated binding energy of –1.2 GHz and an average bond length of $\langle r \rangle = 12$ Å. A level with similar binding energy in the *g*-state is level 39, which has a calculated binding energy of –1.3 GHz and an average bond length of $\langle r \rangle = 29$ Å. It is interesting to compare these values with the properties calculated for level 3. This level is calculated to have binding energy of -140.86 GHz (–4.7 cm^{-1}) and an average bond length of $\langle r \rangle = 4.3$ Å, which is clearly much shorter than nearby levels. This therefore supports the evidence that this level originates from the inner well of the I $(1/2)_g$ state, a state which supports a total of 14 vibrational levels, 5 of which have considerable inner-well character. As was shown in Section 4.3.1, in the absence of local perturbation by the levels of the inner well, a Hund's case (c) or case (e) basis set best describes levels in the outer well. The inner-well levels however, are described best by a Hund's case (a) basis set ($^2\Pi_{1/2g}$). The *g*-factors of the outer-well levels are clearly perturbed by levels of a similar energy in the inner-well, and *vice versa*. The measured *g*-factors therefore provide an extremely sensitive measure of the height and width of the barrier and consequently the extent of mixing between the inner and outer well levels. The maximum height of the barrier is calculated to be 6.36 cm^{-1} at $r = 3.37$ Å. The complete I $(1/2)_g$ state potential is shown with the calculated bound states in Figure 4.10. It can be seen that the separations between the inner-well levels are relatively large and it is therefore quite a coincidence that an inner-well level occurs within the small energy range sampled by this experiment. Although at first this was seen as a hindrance to the experimental work, it was actually a rather fortunate coincidence since it provided considerable constraint to the *g*-state coupled channel calculations and also provided some very interesting data about the state which may have otherwise never been known.

The calculated interaction potentials clearly explain the majority of the experimental data, and also provide very interesting insights into the subtleties of the spectroscopic data. However, it must be remembered that one of the stated aims of this study is to understand the long-range interaction between a neon atom and a neon ion. It is therefore important to question the validity of the calculated parameters,

with particular focus on the calculated values of the C_n terms that form the multipole expansion.

Medved *et al.* [94] have recently calculated the dipole polarisabilities of ^2P systems and their quadrupole moments, enabling an estimate of the isotropic, $[C_6]_0$, and anisotropic, $[C_6]_2$, contributions to be calculated. The values obtained from the current work are compared with those of Medved *et al.* in Table 4.8.

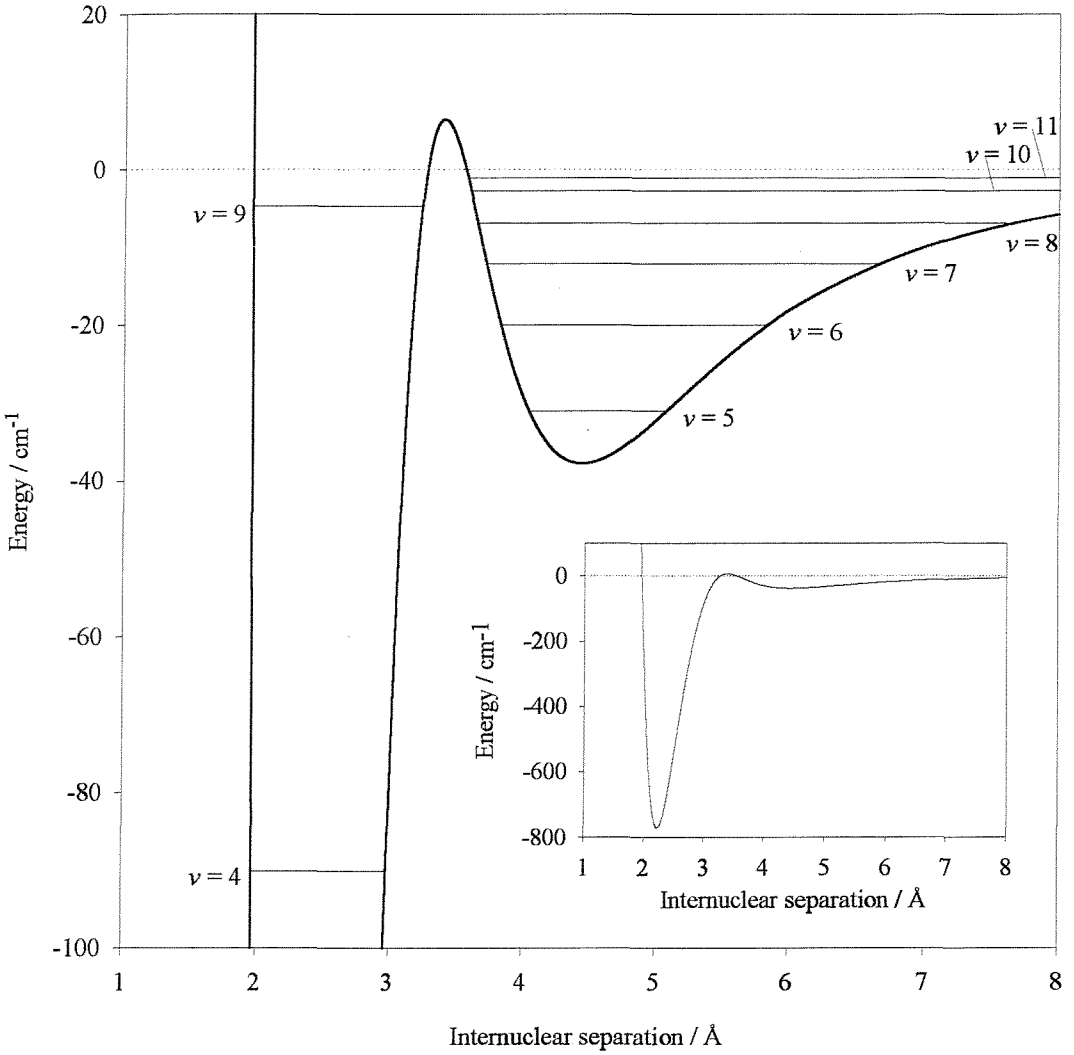

Figure 4.10: The fitted I $(1/2)_g$ double minimum potential curve of this work, indicating bound vibrational levels (calculated with $J = 1/2$). The inset shows the full extent of the inner well. The calculations predict three further vibrational states, $v =$ 12, 13 and 14. These have been omitted for clarity.

	$[C_6]_\Sigma / e^2a_0^5$	$[C_6]_\Pi / e^2a_0^5$
Medved *et al.* [94]	10.354	5.128
this work, *g*-state calculation	9.112	5.995
this work, *u*-state calculation	11.372	6.258
this work, average	10.242	6.127

Table 4.8: Comparison of recently calculated $[C_6]$ coefficients.

As stated in Section 4.4.2, using first principles the C_6 coefficients are expected to be in the ranges $7.69 < [C_6]_\Sigma < 11.29\ e^2a_0^5$ and $5.89 < [C_6]_\Pi < 7.69\ e^2a_0^5$. The calculated values do indeed fall within these ranges. It was also stated in Section 4.4.2 that one of the advantages of the coupled channel calculations used in this work is the provision of two independently calculated values of the C_6 parameters. It may be seen from Table 4.8 that the average of the two values for $[C_6]_\Sigma$ is indeed very close to that of Mevdev *et al.*, whereas both the calculated values for $[C_6]_\Pi$ are slightly higher.

It is important to make a similar analysis of the derived C_8 parameters. It was stated in Section 4.4.2 that the C_8 coefficients for $^{20}Ne_2^+$ are expected to fall in the range $55.5 < C_8 < 96.5\ e^2a_0^7$. However it has already been noted that the derived values for $[C_8]_\Lambda$ are not physically reasonable: not only do they all fall well outside this range, two of them are also negative. The reason for this is because they were derived to ensure the minima of the potentials occur in the desired positions. This approach worked well for the earlier studies of $HeAr^+$ [34] and $HeKr^+$ [35], but it appears to result in unrealistic values for a system with deep potentials such as Ne_2^+. Since the C_{10} parameters are linked by a constant factor to the C_8 coefficients, these will also be physically unrealistic.

This is an unsatisfactory situation, since an understanding of the long-range interactions was one of the primary objectives of this study. The method used here has allowed the long-range parameters to take any value necessary ("take up the slack") to constrain the short-range part of the system. It is therefore recommended that future work uses an alternative parameterisation in which the potential minimum is constrained by deriving A_Λ and a_Λ, instead of A_Λ and $[C_8]_\Lambda$. This may introduce

additional problems with parameter correlation, but the resulting estimates for the long-range parameters would be more realistic.

At short range there is significant overlap of the electronic wavefunctions and for the ground state this results in a chemical bond. A simple Morse function has been used to describe this region of the potential with Tang-Toennies damping coefficients preventing the r^{-n} expansion from dominating at short range. The damping coefficients have been calculated *ab initio* and tested on many potentials that demonstrate van der Waals minima [86]. However, these trial potentials were all of order 100 cm^{-1} and no systems with a well-depth as deep as that for Ne_2^+ have been parameterised in this way.

A further approximation used in this representation of the intermolecular potential is the choice of spin-orbit coupling constant. At all bond lengths it assumed the value for the $Ne^+(^2P)$ ion, although at short range a molecular description of the spin-orbit coupling within a chemical bond may have been more appropriate. However, an accurate determination of the *r*-dependence may prove difficult with such a highly correlated parameter set.

A new procedure recently developed by Meuwly and Hutson [95] may resolve the problems posed by the damping functions and spin-orbit coupling. They describe the "morphing" of potential energy functions, a method involving scaling functions for both the energy and the intermolecular distance. The objective of the morphing process is to achieve agreement with experimental data by making changes to the potential energy surface that are as small as possible. This has the advantage of giving a balanced representation of the interaction potential without needing to separate the long and short-range interactions.

4.5 Concluding remarks

This is the first study to utilise the molecular beam chamber and thus successfully study a long-range ion not containing helium. Due to the deep potential curves of the Ne_2^+ system, the near-dissociation microwave spectrum is very dense: a total of 278 transitions were recorded in the frequency range 6 – 170 GHz. The assignments of 204 of these have been confirmed using double resonance experiments and measurement of Zeeman spectra. A further 31 assignments are predicted and many of

the remaining 43 unassigned transitions are hypothesised to correlate with the second dissociation limit.

An accurate set of interaction potentials for the Ne_2^+ ion at all bond lengths has been calculated by means of the coupled channel method and using both the present experimental data and that of other authors. The values of the short-range constants obtained compare favourably with others published, although it is clear that re-parameterisation is necessary to derive realistic C_8 and C_{10} long-range coefficients.

Despite the short-comings of the calculated results, the work has provided detailed information on the levels lying within 10.2 cm^{-1} of the first dissociation limit, most notably those of the I $(1/2)_g$ state which possesses a potential maximum.

All the experimental and theoretical results reported here describe the most abundant isotopomer, $^{20}Ne_2^+$. However, since there is significant natural abundance of the isotope ^{22}Ne it should be possible to study $^{22}Ne_2^+$ and the mixed dimer $[^{20}Ne^{22}Ne]^+$. It *should* be trivial to predict the energy level structure of $^{22}Ne_2^+$, but since the Born-Oppenheimer is not valid for the levels under investigation, it is not simply a matter of adjusting the reduced mass in the existing calculations. For completeness, attempts have been made to study this isotopomer, but the ion flux was found too small to work with.

Some success has been achieved with the mixed dimer, although this has also been limited by small ion flux. When the apparatus was optimally aligned, four transitions were recorded, though their assignments remain unknown. The removal of *g/u* symmetry implies that transitions do not have to be purely electronic, but could also be rotational and/or vibrational. It might therefore be expected that the spectrum would be even denser than that observed in $^{20}Ne_2^+$. To complicate matters further, this molecule has four dissociation limits rather than two, correlating with (in ascending energy order) $^{20}Ne\ (^1S_0) + {}^{22}Ne^+\ (^2P_{3/2})$, $^{22}Ne\ (^1S_0) + {}^{20}Ne^+\ (^2P_{3/2})$, $^{20}Ne\ (^1S_0) + {}^{22}Ne^+\ (^2P_{1/2})$ and $^{22}Ne\ (^1S_0) + {}^{20}Ne^+\ (^2P_{1/2})$. Despite these complications, a comprehensive study of the mixed ion would add a fascinating dimension to the work presented here.

Following the success of this study, attention returned to the initial target of the long range complex $Ar\cdots Ar^+$ and this is the subject of Chapter 5.

Chapter 5 - The microwave electronic spectrum of Ar_2^+

5.1 Introduction

Following the successful study of the near-dissociation states of Ne_2^+ (Chapter 4), a second attempt was made to understand the near-dissociation spectrum of Ar_2^+, and the results of the subsequent investigation are presented in this chapter. It was felt that the theoretical knowledge and experimental skills gained from the study of Ne_2^+ (especially the extended use of microwave-microwave double resonance techniques) would mean that an understanding of the near-dissociation microwave spectrum of Ar_2^+ was achievable, despite the possibility of not observing any resolved Zeeman spectra.

The interest in cluster research has grown enormously over the past few decades since they form a link between isolated gas-phase species and the condensed phase. Knowledge of cluster properties could, therefore, contribute to our understanding of the forces responsible for nucleation phenomena.

During the last twenty years, much work has been devoted to identifying the charge bearing centres in small argon ion clusters. Since D_0^0 (Ar^+–Ar) ≈ 1.3 eV [96] and D_0^0 (Ar_2^+–Ar) ≈ 0.2 eV [97] it was initially assumed that Ar_2^+ was the charge bearing entity in these systems [98]. However, both early *ab initio* [99, 100] and diatomics-in-molecules [101 - 103] calculations suggested that Ar_3^+ is a linear symmetric molecule and consequently has the charge dispersed over three atoms instead of two. The photodissociation cross section measurements of Levinger *et al.* [104] appeared to support this interpretation since the absorption profile they observed in Ar_n^+ clusters was very similar for n = 3–15 and well removed from the Ar_2^+ photoabsorption maximum. A number of other experimental studies supported the suggestion of Ar_3^+ being the core of small argon clusters, including the photoionization work of Gantför *et al.* [105] and the photodissociation work of Chen *et al.* [106].

Even with so much corroborative evidence suggesting Ar_3^+ as the ionic core, the debate continued. There have been suggestions that either Ar^+ [107] or Ar_4^+ [108]

is the ionic core, but neither of these proposals has received much further support in the literature. Most promising however, is the proposal of an Ar_3^+ core with a double minimum configuration such as Ar_2^+·Ar: DeLuca and Johnson [109] reported a strong UV absorption for Ar_3^+ near 300 nm, similar to the strong $^2\Sigma_g^+ \leftarrow {}^2\Sigma_u^+$ absorption in the Ar_2^+ ion [110], which remains intact in the larger ($n \leq 7$) clusters. In order for this transition to be allowed in Ar_3^+ the ground state must be bent, or it must be linear but with the two bond lengths different. The *ab initio* calculations of Bowers *et al.* [111] are in strong qualitative agreement with this interpretation, and they concluded that Ar_3^+ is essentially an Ar_2^+·Ar cluster. Perhaps it is simply a question of semantics whether Ar_3^+ is considered a "new chemical species" or whether it is an Ar_2^+ ion core perturbed by an argon atom. Indeed the photodissociation data of Snodgrass *et al.* [112] and the photofragmentation results of Woodward *et al.* [113] are best explained by assuming that a strongly perturbed Ar_2^+ is the chromophore in Ar_3^+. Although these two studies agree that Ar_3^+ takes the form of a stable dimer ion and a weakly bound atom, they disagree over whether the structure is linear [112] or non-linear [113].

The power of the early calculations, particularly the diatomics-in-molecules studies, is rather limited since the diatomic input potentials were of extremely poor quality. Recently however, high accuracy *ab initio* potential energy curves for Ar_2^+ have become available [114] and Doltsinis and co-workers [115, 116] have used them as the input for new, accurate diatomics-in-molecules calculations on Ar_n^+ clusters. They have shown that the Ar_3^+ molecule is the basic building block for all clusters up to Ar_{13}^+. Since the quality of such diatomics-in-molecules calculations depends critically on the input Ar_2^+ potentials, it is the ultimate aim of this work to obtain accurate potential curves for the diatomic ion, as was demonstrated for Ne_2^+ in Chapter 4.

Over the last few decades there have been many experimental and theoretical studies of Ar_2^+ and the following discussion is not expected to be exhaustive. Prior to this work there have been no reports of experimentally observed bound to bound transitions, but many observations of transitions from the neutral dimer.

Among the first reliable estimates of the dissociation energy of Ar_2^+ were the results of rainbow scattering by Lorents *et al.* [117] and Mittman and Weise [69].

These studies gave values of D_e to be 1.25 eV and 1.34 eV respectively. In the late 1970s, a photoionisation study of Ar_2^+ by Ng *et al.* [118] gave D_0 to be 1.23 ± 0.02 eV but the photofragment results of Moseley *et al.* [110] gave a rather larger value of D_0 = 1.33 ± 0.02 eV. The photoelectron spectroscopy results of Dehmer and Dehmer [119] are in fair agreement with this larger value. In 1989 Norwood *et al.* [120] published results of their photoion-photoelectron coincidence (PIPECO) study of small argon clusters. They determined the dissociation energy of Ar_2^+ to be 1.24 ± 0.02 eV.

In 1993 Pradeep *et al.* [121] also used photoelectron spectroscopy to study the rare gas dimers and they obtained values of the spectroscopic constants for four of the six lowest electronic states of Ar_2^+. They obtained a value of D_e = 1.361 eV for the ground state.

The recent high resolution photoelectron spectroscopy results of Hall *et al.* [74] probably provide the best experimentally determined values of the spectroscopic parameters of Ar_2^+. They observed transitions from the neutral dimer to 50 vibrational levels of the ion, but since the lower vibrations are likely to be populated via autoionisation, the absolute vibrational assignment is not clear. If the first observed level is assumed to be $v = 0$, then the dissociation energy is determined to be 1.207 ± 0.005 eV, which is lower than most previous determinations. However if the lowest observed level is assumed to be $v = 3$, then the calculated dissociation energy of 1.320 ± 0.005 eV is in good agreement with both Mittman and Weise [69] and Moseley *et al.* [110]. It is this uncertainty in vibrational assignment that is probably the main reason for the large discrepancies in all the experimentally determined values quoted for the dissociation energy of Ar_2^+.

Complementary to these experimental determinations of the dissociation energy are a number of theoretical investigations [for example refs. 76, 78, 82, 100, 103, 114, 122 - 124], many of which also provide very useful information on the excited states. A summary of the experimental and theoretical studies of the ground state of Ar_2^+ is provided in Table 5.1.

The most recent *ab initio* Ar_2^+ potential curves are those of Knowles [114] and have been obtained from RCCSD-T calculations using an aug-cc-pV5Z basis set. The potential curves for Ar_2^+ have the same structure as those for Ne_2^+. The argon atom

and its ion in their ground states form four molecular states that separate into six when spin-orbit effects are included. Four of these dissociate to the lowest dissociation limit ($^2P_{3/2}$) and two to the next lowest ($^2P_{1/2}$). The spin-orbit coupling constant for Ar^+ is 1432 cm^{-1} [84], and the two lowest dissociation limits of Ar_2^+ are therefore split by this amount. A more realistic long-range tail was added to the potentials of Knowles [114] and the spin-orbit coupling was added using the computer program BOUND [92]. The resulting curves are shown in Figure 5.1.

Table 5.1: Experimental and theoretical studies of Ar_2^+ ($X\,^2\Sigma_{1/2u}^+$). * See glossary on page 146 for list of abbreviations used

Method	D_0 / eV	ω_e / cm^{-1}	$\omega_e x_e$ / cm^{-1}	Reference (year)
EXPERIMENT				
Rainbow scattering	1.25 (D_e)	-	-	Lorents *et al.* (1973) [117]
Rainbow scattering	1.34 (D_e)	-	-	Mittman & Weise (1974) [69]
Photoionisation	1.23 ± 0.02	-	-	Ng *et al.* (1977) [118]
Photofragment spectroscopy	1.33 ± 0.02	-	-	Moseley *et al.* (1977) [110]
Photoelectron spectroscopy	1.349 (D_e)	308.9	1.658	Dehmer & Dehmer (1978) [119]
Photoion-photoelectron coincidence spectroscopy	1.24 ± 0.02	-	-	Norwood *et al.* (1989) [120]
Photoelectron spectroscopy	1.361 (D_e)	-	-	Pradeep *et al.* (1993) [121]
Photoelectron spectroscopy	1.207 ± 0.005	300.8 ± 0.8	2.283 ± 0.016	Hall *et al.* (1995) [74] (assuming lowest observed level is $v = 0$)
Photoelectron spectroscopy	1.320 ± 0.005	314.6 ± 0.8	2.283 ± 0.016	Hall *et al.* (1995) [74] (assuming lowest observed level is $v = 3$)
THEORY *				
SCF	1.25	300	-	Gilbert & Wahl (1977) [76]
SCF	1.20	-	-	Stevens *et al.* (1977) [122]
POL-CI	1.19 (D_e)	293	-	Wadt (1978) [123]
Density functional method	1.304	297.9	1.7	Michels *et al.* (1978) [78]
MRD-CI	1.19 (D_e)	291	-	Böhmer & Peyerimhoff (1986) [100]
SCF-CI	1.27	-	-	Whitaker *et al.* (1990) [124]
SCF-CI	1.31 (D_e)	-	-	Ikegami *et al.* (1993) [103]
RCCSD-T	1.3657 (D_e)	-	-	Knowles (1995) [114]
Calculated on the basis of experimental data	1.384	-	-	Chen *et al.* (1997) [106]

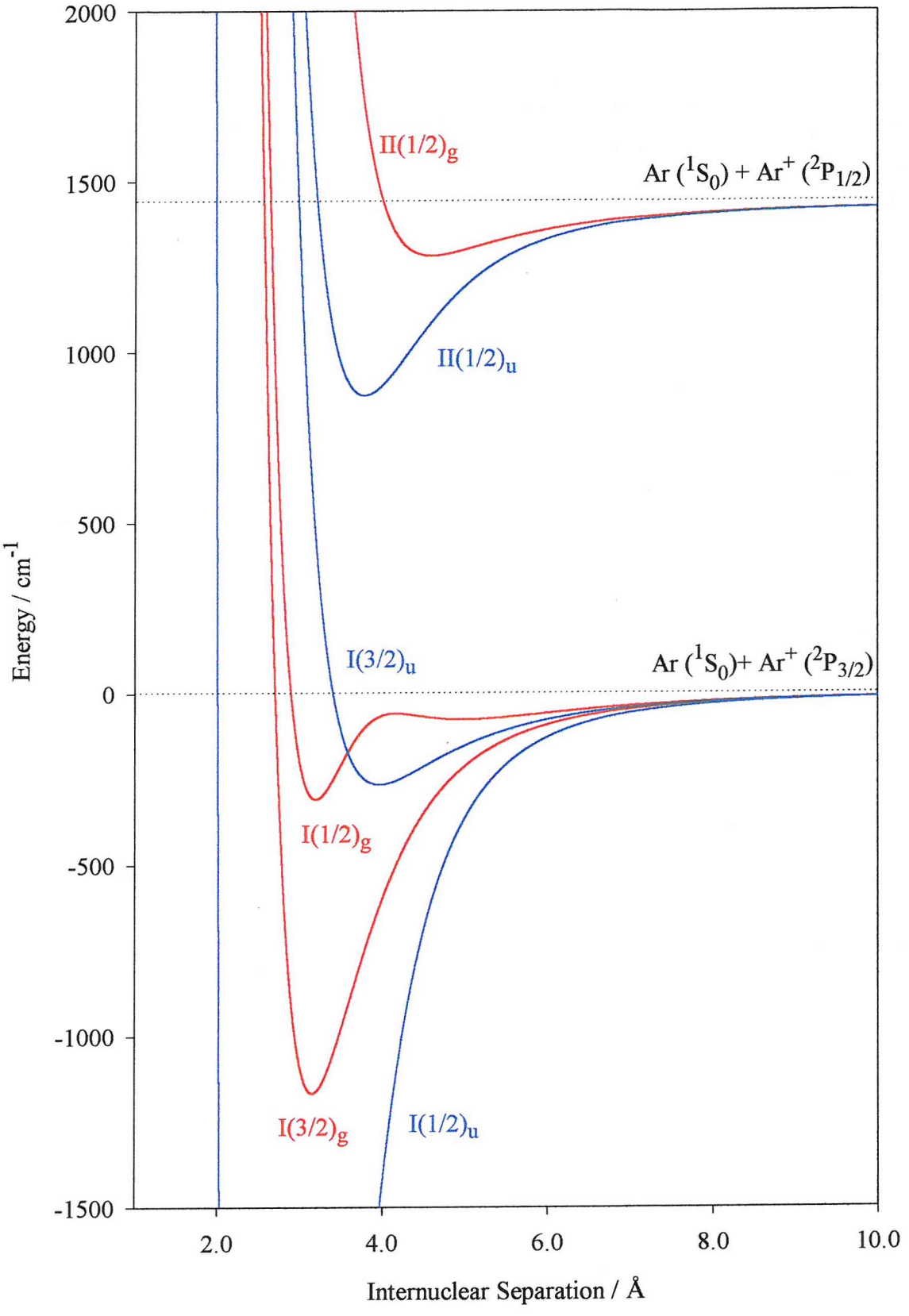

Figure 5.1: The Ar_2^+ potentials of Knowles [114] with a realistic long-range tail and spin-orbit coupling added (see text for detail).

5.2 Experimental

As expected, singly charged argon clusters larger than Ar_2^+ were detected in the apparatus; indeed all clusters up to and including Ar_{13}^+ were observed with significant intensity. Nozzle position and tuning conditions were chosen to maximise the Ar^+ peak resulting from the electric field dissociation of Ar_2^+, though it was not possible to determine whether these were the optimum conditions for producing Ar_2^+ via vertical ionisation of the neutral dimer (Section 1.2.1).

5.2.1 Observed transitions

Using a nozzle aperture of 20 μm, a comprehensive scan over the frequency range 14.1–140 GHz, with a number of combinations of source voltage and electric field lens potentials, yielded sixty-two transitions in the long-range Ar···Ar^+ ion. All of these were observed either as weak resonances (*i.e.* requiring maximum power available and/or extensive signal averaging) or as transitions with broad modes (FWHM ≥ 2 MHz compared with the 'normal' FWHM of ~0.8 MHz), an observation attributed to the Earth's magnetic field and other local residual fields. The transitions in the latter set appear to be intrinsically broad; reducing the microwave power caused them to disappear into the noise rather than sharpen. The combination of these factors, together with the problem of transmitting frequencies in the range 75–110 GHz through the magic-T, meant that only twelve of these transitions initially observed were good enough to pump. Those that were, were each used as a pump and the available frequency ranges were "blindscanned" (Section 3.5) to search for new transitions. These secondary searches yielded a further five transitions, none of which were subsequently observed single photon. Comprehensive searches were then carried out with both a 10 μm and a 50 μm nozzle aperture in place. The former yielded no new transitions, but one previously observed transition (84657.5 MHz) was observed with this aperture also. Using the 50 μm aperture was slightly more successful, yielding two new transitions. Furthermore, six of the previously observed transitions were also seen with this larger aperture in place. Neither of these new transitions was strong enough to pump. Table 5.2 summarises the 69 microwave transitions recorded in this molecular ion and also includes brief details of the transition properties, including the effect of applying an external field.

Table 5.2: Summary of the microwave transitions observed in $Ar\text{-}Ar^+$. * Where an accurate rest frequency has not been determined, it is quoted to the nearest 100 MHz.

Frequency / MHz	Nozzle aperture / μm	Source voltage / kV	Electric field lens voltage / kV	Description of transition in zero field	Effect of external magnetic field (where studied)
16187.0	20	6.0	1.0	Excellent pump	Zeeman effect studied in detail (Section 5.4)
16952.5	20	6.0	2.5	Excellent pump	Broadened, no structure
17529.1	20	3.0	0.5	Not seen single photon	
22080.3	20, 50	3.0 (6.0)	0.5 (1.5)	Excellent pump	Unresolved Zeeman study
23303.2	20	3.0	1.0	Strong pump	Unresolved Zeeman study
23715.0	20	6.0	1.5	Not seen single photon	
25423.0	20	3.0	0.5	Not seen single photon	
26804.8	20	6.0	0.5	Broad mode (FWHM 2.5 MHz). Unable to pump	
26993.1	20	3.0	1.0	Broad mode (FWHM 2.5 MHz). Unable to pump	
27735.7	20, 50	6.0	2.5	Unable to pump	Unresolved Zeeman study
27769.4	20	6.0	1.5	Not seen single photon	
28972.0	20	6.0	1.5	Unable to pump	Unresolved Zeeman study
31090.7	20	6.0	1.5	Good pump	Unresolved Zeeman study
31384.5	20	3.0	0.5	Not seen single photon	
~31400*	20	6.0	3.5	Maybe an harmonic	

Table 5.2: *(Continued)*

Frequency / MHz	Nozzle aperture / μm	Source voltage / kV	Electric field lens voltage / kV	Description of transition in zero field	Effect of external magnetic field (where studied)
31899.5	20	3.0	0.5	Unable to pump	
34936.5	20	6.0	0.5	Broad modes (FWHM 2.0 MHz). Good pump	Too much mode contamination
37831.3	20	6.0	2.5	Poorly resolved peaks	
42325.8	20	6.0	2.5	Unable to pump	
42769.5	20	3.0	0.5	Good pump	Unresolved Zeeman study
43653.8	20, 50	6.0 (3.0)	1.5 (0.5)	Unable to pump	Unresolved Zeeman study
44324.6	20	6.0	1.5	Broad modes (FWHM 2.0 MHz). Unable to pump	
46913.0	50	6.0	2.5	Broad modes (FWHM 2.5 MHz). Unable to pump	
50454.0	20, 50	6.0	2.5	See parallel modes only. Unable to pump	
54049.2	20	6.0	0.5	Unable to pump	
54253.5	20	6.0	2.5	Poorly resolved peaks	
~54700*	20	6.0	2.5	Poorly resolved peaks	
54988.6	20	6.0	0.5	Unable to pump	
~57704.0	20	6.0	0.5	Broad modes (FWHM 2.0 MHz). Unable to pump	
58686.5	20	6.0	0.5	Unable to pump	

Table 5.2: *(Continued)*

Frequency / MHz	Nozzle aperture / μm	Source voltage / kV	Electric field lens voltage / kV	Description of transition in zero field	Effect of external magnetic field (where studied)
59051.2	20	6.0	1.5	Unable to pump	
59207.1	20	6.0	2.5	Reasonable pump	Too much mode contamination
60109.7	20	6.0	0.5	Reasonable pump	Unresolved Zeeman study
60233.5	50	6.0	2.5	Unable to pump	
60513.0	20	6.0	1.5	Unable to pump	
60638.2	50	6.0	2.5	Very weak	
62643.6	20	6.0	2.5	Possible to pump, though poor resolution	
64141.6	20	6.0	0.5	Unable to pump	
69397.6	20	6.0	0.5	Unable to pump	
76406.6	20	3.0	0.5	Well resolved peaks, but very weak	
77497.9	20	3.0	0.5	Weak	
77511.0	20	3.0	0.5	Weak	
77629.8	20	6.0	2.5	Unable to pump	
77689.0	20	3.0	0.5	Unable to pump	
82451.6	20	3.0	0.5	Excellent pump	Too much mode contamination

Table 5.2: *(Continued)*

Frequency / MHz	Nozzle aperture / μm	Source voltage / kV	Electric field lens voltage / kV	Description of transition in zero field	Effect of external magnetic field (where studied)
84657.5	10, 20, 50	6.0	2.5	Broad modes (FWHM 2.0 MHz). Unable to pump, despite being a very strong transition	Unresolved Zeeman study
86276.3	20	3.0	1.0	Weak	
86616.9	20	6.0	0.5	Unable to pump	
~87000*	20	6.0	2.5	Unable to determine accurate rest frequency due to poor resolution	
89345.3	20, 50	6.0	2.5	Unable to pump, despite being a strong transition	Unresolved Zeeman study
89751.4	20	6.0	2.5	Broad modes (FWHM 2.0 MHz). See parallel modes only. Unable to pump	
93496.3	20	3.0	0.5	Weak	
94222.4	20	6.0	0.5	Weak	
97293.3	20	3.0	0.5	Weak	
99251.5	20	6.0	0.5	Broad modes (FWHM 2.0 MHz). Unable to pump	
100363.7	20	3.0	0.5	Weak	
100384.8	20	3.0	0.5	Weak	
102033.2	20	3.0	0.5	Poorly resolved peaks	
103177.2	20	6.0	0.5	Weak	
111321.7	20	6.0	0.5	Unable to pump, despite being a strong transition	

Table 5.2: *(Continued)*

Frequency / MHz	Nozzle aperture / μm	Source voltage / kV	Electric field lens voltage / kV	Description of transition in zero field	Effect of external magnetic field (where studied)
113308.0	20	3.0	1.0	Good pump	Appears to be non-magnetic, *i.e.* no observable effect when max. external field applied
114312.0	20	6.0 (3.0)	0.5 (1)	Well resolved peaks, but not strong enough to pump	
114337.0	20	3.0	1.0	Weak	
114572.5	20	6.0	2.5	Weak	
114603.3	20	6.0	2.5	Weak	
124856.7	20	6.0	2.5	Unable to pump	
126166.3	20	6.0	0.5	Weak	
128834.5	20	3.0	0.5	Poorly resolved peaks	
129315.0	20	6.0	0.5	Unable to pump	

5.2.2 Transition connectivities

In addition to using them for "double resonance blindscanning", the twelve good pump transitions were also used to investigate if any of the transitions were connected. Four positive results were obtained, giving a total of nine transition connectivities, which are listed in Table 5.3.

Pump transition / MHz	Probe transition / MHz
16187.0	23303.2
	27769.4
16952.5	28972.0
	43653.8
	62643.6
22080.3	23715.0
42769.5	25423.0
82451.6	17529.1
	31384.5

Table 5.3: Summary of transition connectivities established in Ar_2^+.

Since three transitions were confirmed to be in double resonance with the 16952.5 MHz transition, at least two of them must themselves be connected. Unfortunately it is possible to pump only one of these three transitions and scanning the other two transitions gave no positive result. Similarly, the 23303.2 MHz transition was pumped and the 27769.4 MHz transition scanned, but again a negative result was obtained. Ideally, a similar attempt would be made with the transitions attached to the 82451.6 MHz transition, but since neither of them was seen single photon, such attempts could not be made. As discussed in Section 3.6.1, the success of double resonance experiments is highly variable and no conclusions may be drawn from a negative result.

It rapidly became clear that the lack of resolved Zeeman spectra and few good pump transitions would limit progress in this investigation. The combination of resolved Zeeman spectra and positive double resonance results is essential for the

construction of a detailed near-dissociation energy level diagram. Despite variations in nozzle conditions and microwave radiation generation, neither of these techniques was found to work effectively in this study.

The focus of the study therefore changed from constructing a near-dissociation energy level diagram (and ultimately good potential energy curves) to investigating if anything could be learnt from the unresolved Zeeman spectra.

5.3 Why have none of the Zeeman spectra resolved?

To begin to understand why none of the attempted Zeeman experiments has produced a resolved spectrum, it is first necessary to consider, in detail, the mechanisms by which Ar_2^+ may have been formed in this experiment. If the ion had been formed by vertical ionisation from the neutral (as discussed in Section 1.2.1), then it is expected that the rotational cooling (as a consequence of the supersonic expansion) would be preserved in the dimer ion. This mechanism was clearly responsible for the observation of the lowest rotational levels in Ne_2^+ (Chapter 4). However, since none of the Zeeman patterns for Ar_2^+ have resolved, it is reasonable to assume that this dimer ion is rotationally hot, and therefore other mechanisms of formation must be considered.

5.3.1 Formation of argon clusters in a supersonic jet

The dominant interaction between rare gas atoms is the induced dipole - induced dipole interaction ("dispersion interaction"). The strength of this dispersion interaction depends on the dipole polarisability of both atoms and how close the two atoms can approach, thus,

$$V \propto \frac{\alpha_A^{\,2}}{R^6}, \tag{5.1}$$

where V is the potential energy of interaction of two identical atoms with polarisability volumes α_A separated by a distance R.

Neon has a dipole polarisability of 2.67 a_0^3 [87] but that of argon is much larger at 11.07 a_0^3 [87]. The polarisabilities of krypton and xenon are even greater still, but because of their size these atoms cannot get very close together. The combination of these factors causes argon to cluster very easily, and much more readily than any of the other noble gases.

For the current investigation it would be ideal to maximise the production of neutral argon dimers in the supersonic expansion, whilst simultaneously minimising the production of larger argon clusters, Ar_n ($n > 3$). The Ar_2 molecules would then be bombarded with electrons, to cause vertical ionisation to form Ar_2^+ in near-dissociation energy levels (as discussed in Section 1.2.1). This ideal situation occurred in the study of Ne_2^+ (Chapter 4), but not in the study of Ar_2^+ since argon clusters so much more readily than neon.

To overcome this problem, it is necessary to consider how to form a supersonic expansion of argon whilst minimising the formation of clusters larger than the dimer. The extent of such cluster formation depends on a number of factors, including nozzle diameter, nozzle temperature and backing pressure. An estimate for P_L, the backing pressure above which significant cluster formation might be expected, has been given by van Deursen and Ruess [125]: assuming a nozzle diameter of ≈ 26 μm and nozzle temperature of 294 K they estimated P_L to be in the range 2.1–3.2 bar. Some authors have since suggested that this estimate is too high [121, 126] and whilst these assumed nozzle conditions are not identical to those in the current investigation, this estimate serves as a useful guide to the backing pressure at which clusters larger than the dimer may be formed. In the current investigation backing pressures below 1.0 bar were tried, but the beam was found to be too small to work with. A backing pressure of 3.5 bar was found to produce the largest, most usable beam and was therefore used throughout, although it is almost certain that this pressure is greater than P_L. As the backing pressure is increased above P_L, there are two factors that may alter. These are:

1) the rotational and vibrational temperature of neutral Ar_2. Experiment and theory show that both these temperatures should fall as the backing pressure is increased [127];

2) increased nozzle pressure during the expansion of a pure gas is always accompanied by an increase in the relative intensities of clusters larger than the dimer [128]. Only at *very* small pressures can the contribution of trimers and higher clusters be neglected [126].

Buck *et al.* [129] measured the cluster formation up to cluster size $n = 6$ in supersonic expansions as a function of source pressure, p_0, and nozzle diameter, d. They found that the intensity of larger clusters increases rapidly with increasing pressure and less pronounced with nozzle diameter. The ratio of the cluster density $\rho(Ar_n)$ to the monomer density $\rho(Ar)$ is found to scale according to a power law [126, 129],

$$\frac{\rho(Ar_n)}{\rho(Ar)} \propto p_0^{\alpha_n} d^{\beta_n}, \tag{5.2}$$

where the exponents α_n and β_n for $n = 2$ to 6 are given in Table 5.4.

n	2	3	4	5	6
α_n	1.3 ± 0.2	2.4 ± 0.3	3.3 ± 0.4	4.2 ± 0.4	5.1 ± 0.5
β_n	0.6 ± 0.2	1.2 ± 0.3	1.4 ± 0.3	-	-

Table 5.4: Exponents α_n and β_n of Equation 5.2 for argon at 300 K [126, 129].

There is good evidence that $\alpha_n \approx n - 1.0$ and since the monomer density is proportional to p_0, the results of Table 5.4 indicate that the pressure dependence of Ar_n clusters for $n \leq 6$ roughly scales with the cluster size n (*i.e.* $\rho(Ar_n) \propto p^n$). The experimental results for Ar_2 formation ($\alpha_2 = 1.3$, $\beta_2 = 0.6$) agree fairly well with two theoretical calculations: $\alpha_2 = 1.67$, $\beta_2 = 0.67$ [130] and $\alpha_2 = 1.47$, $\beta_2 = 0.47$ [131].

Thus in an attempt to reduce the density of clusters in the expansion, the current experiment was attempted with a nozzle aperture of 10 μm. The beam displayed very strange tuning characteristics with this aperture in place, and it is believed that dust or other impurities in the gas supply caused a partial closure of the aperture. The beam produced with a nozzle of diameter 20 μm was not found to

suffer with the same limitations and was therefore used for the majority of the investigation.

It has been found that cluster size increases not only with increasing source pressure and increasing nozzle diameter, but also with decreasing nozzle temperature [132]. Since it is not currently possible to heat the nozzle (and thus reduce the average cluster size), it was operated at room temperature throughout the investigation.

Although it was not possible to change the geometry of the nozzle due to the constraints of the apparatus, it is worth noting that the formation of clusters is promoted by using nozzles that give a less rapid expansion, *i.e.* a long slow expansion favours the condensation process [133]. Therefore the simple aperture design used in the current work (a small hole in a piece of thin metal foil) should not encourage the clustering process.

Furthermore, the neutral cluster size distribution depends sensitively on which part of the solid angle of the expansion is being sampled [134], as separation of species occurs as a result of different perpendicular speed ratios, leading to enrichment of larger clusters on the centreline axis. This effect is enhanced by the use of a skimmer. In the current investigation, the position of the nozzle behind the skimmer was determined by maximising the Ar_2^+ parent signal, and although not verified, it is assumed that this position was very close to the centreline.

In summary, attempts have been made to minimise the amount of higher order clusters formed within the expansion, although it is not possible to directly measure the ratios of nascent products. It is expected, however, that at such a high backing pressure and with no heating of the nozzle possible, a large proportion of signal on the dimer mass is essentially due to larger clusters fragmenting rather than the desired formation by vertical ionisation. The fragmentation of these larger clusters is now discussed in detail.

5.3.2 The effect of ionisation on the argon clusters

Electron impact ionisation of a fragile inert gas cluster is a comparatively violent process [98, 135]. However, because mass spectrometric measurements can only be made on a timescale $\geq 10^{-6}$ s, knowledge of such processes is very limited. It is commonly accepted, however, that rare gas clusters fragment strongly after ionisation and this was studied by Buck and Meyer [136] in 1986. They studied the formation

of small Ar_n clusters in a supersonic expansion very similar to the one used in the current investigation and using scattering analysis they measured the subsequent fragmentation probabilities by electron impact ionisation. Table 5.5 shows some of their results.

n	f_{n1}	f_{n2}	f_{n3}
2	0.40	0.60	...
3	0.30	0.70	$< 10^{-4}$
4[a]	...	1.00	$< 5 \times 10^{-3}$
5[a]	...	0.98	0.02
6[a]	...	0.95	0.05

Table 5.5: Fragmentation probabilities of Ar_n clusters for electron bombardment at 100 eV [136]. [a] Incomplete results determined only from the ratio f_{n3} / f_{n2}, assuming $f_{n3} + f_{n2} = 1$.

It should be noted that an electron energy of 50 eV was used throughout the current investigation, however it has been shown [137] that fragmentation probabilities depend only slightly on the electron energy used (in the range 30–100 eV).

It is interesting to note that almost half of the dimers formed in the beam fragment on electron impact to form $Ar + Ar^+$. This may explain why, in the current investigation, the Ar_2^+ beam current was so small at low backing pressures, *i.e.*, it is possible that the majority of the nascent products were dimers, but 40 % of these then fragmented on ionisation. Also pertinent to the current investigation is the observation that neutral trimers formed in the beam totally fragment into monomers and dimers. Time-of-flight analysis [137] shows that any Ar_3^+ ions that *are* detected originate from parent ions with $n > 5$. Finally, note that all clusters with n from 4 to 6 fragment with a probability ≥ 0.95 to give Ar_2^+.

These observations have striking consequences for the current study:

(1) 40 % of dimers made in the supersonic expansion may fragment on electron impact;

(2) Assuming neutral trimers are formed in the expansion, 70 % of them may fragment on ionisation to give Ar_2^+, which then passes through the magnetic sector;

(3) The Ar_3^+ peak on the mass spectrum probably originates *entirely* from the fragmentation of larger clusters ($n > 5$);

(4) A significant proportion of the Ar_2^+ that passes through the magnetic sector may come from parent ions with $n = 4$, 5, 6 or higher.

It may therefore be concluded that not only is there significant cluster formation in the current investigation, but also that it is highly probable that the majority of the Ar_2^+ that passes through the magnetic sector (and thus interacts with the microwave radiation) is actually formed from the fragmentation of larger clusters.

5.3.3 Temperature of the fragments

Klots has shown [138, 139] that the unimolecular decay of clusters can be considered in terms of evaporative cooling. Providing a cluster has an internal energy, E, above the dissociation limit, ε_0, an atom will leave, carrying with it some fraction of the excess energy (E-ε_0). Eventually the cluster will cool to a point where its internal energy is $< \varepsilon_0$ and no further evaporations will occur. Scheier and Märk [140] have confirmed Klots' theoretical prediction [138] that the decay series of metastable rare gas clusters $Ar_n^{+*} \rightarrow Ar_{n-1}^{+*} \rightarrow Ar_{n-2}^{+}$ ($n \geq 7$) exists in the μs time window. It is therefore reasonable to assume that such events occur in the apparatus of the current investigation *before* the ions reach the magnetic sector.

In light of this and discussion in previous sections, it is highly probable that the Ar_2^+ ions that are interacting with the microwave radiation in the current investigation are the result of fragmentation of larger clusters. If the unresolved Zeeman spectra are to be understood, then any estimate of rotational temperature of the Ar_2^+ fragments will be useful.

Stace [141] has used a model based on phase space theory to examine the effect that multiple fragmentations from excited, weakly bound argon cluster ions have on the final rotational temperatures of the reaction products. It is not immediately obvious from Klots' approach to cluster decay [138, 139] how the

rotational energy (temperature) behaves. Although constrained by the total energy available, angular momentum conservation will be an important consideration in determining how the rotational temperature changes during evaporation. Another critical factor in determining the temporal evolution of cluster ions is the technique by which they are prepared: ions formed by electron impact (vertical) ionisation of neutral clusters will leave the ions with residual internal energy that will be dissipated through evaporation. In contrast, cluster ions formed via adiabatic expansion in the presence of an electron beam are likely to be much colder and therefore less susceptible to evaporation.

The effect that evaporation has on the rotational temperatures of cluster ions of differing original size (but same initial rotational temperature) is shown in Figure 5.2 [141]. It can be seen that the larger cluster ions (*i.e.* Ar_{40}^+ and Ar_{50}^+) undergo rotational cooling as they lose atoms. For the current investigation it is perhaps more interesting to note the results for the smaller clusters. To conserve angular momentum, the rotational constant, B, increases as the clusters become smaller (just as an ice skater rotates faster as the arms are pulled in). Thus Ar_{10}^+, for example, undergoes quite considerable rotational *heating* as the result of evaporation. This heating effect is not observed in the larger clusters because each atom lost represents a smaller percentage of the mass and the effect of evaporational cooling is greater.

The rotational temperature of Ar_2^+ ions that are formed by direct ionisation of Ar_2 will reflect the temperature of the neutral dimer, *i.e.* ≈ 36 K [142]. The average rotational angular momentum appropriate for such direct ionisation is marked in Figure 5.3. The majority of the Ar_2^+ in the beam is expected to be somewhat hotter, since it comes from larger cluster ions that fragment. Figure 5.3 suggests there should be two components to the Ar_2^+ rotational state population; a "cold" fraction from direct ionisation and a "hot" fraction coming from the decay of larger cluster ions. According to Stace's calculations [141, 143], this fraction may have a rotational temperature > 1000 K.

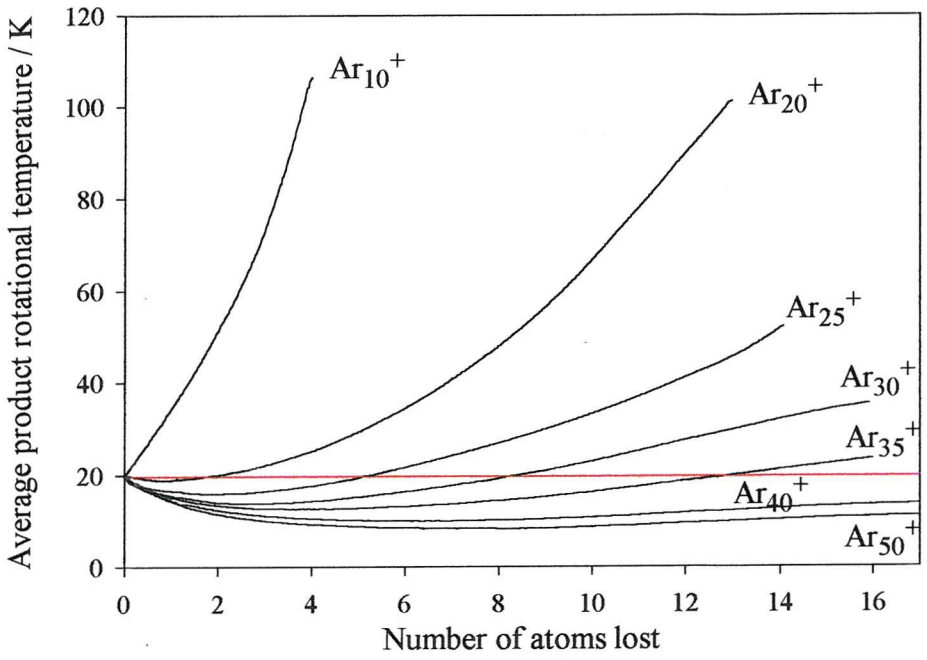

Figure 5.2: Calculated changes in the average product rotational temperature as a function of the number of atoms lost from cluster ions ranging in initial size from Ar_{10}^+ to Ar_{50}^+. Each cluster was given an initial temperature of 20 K. [141]

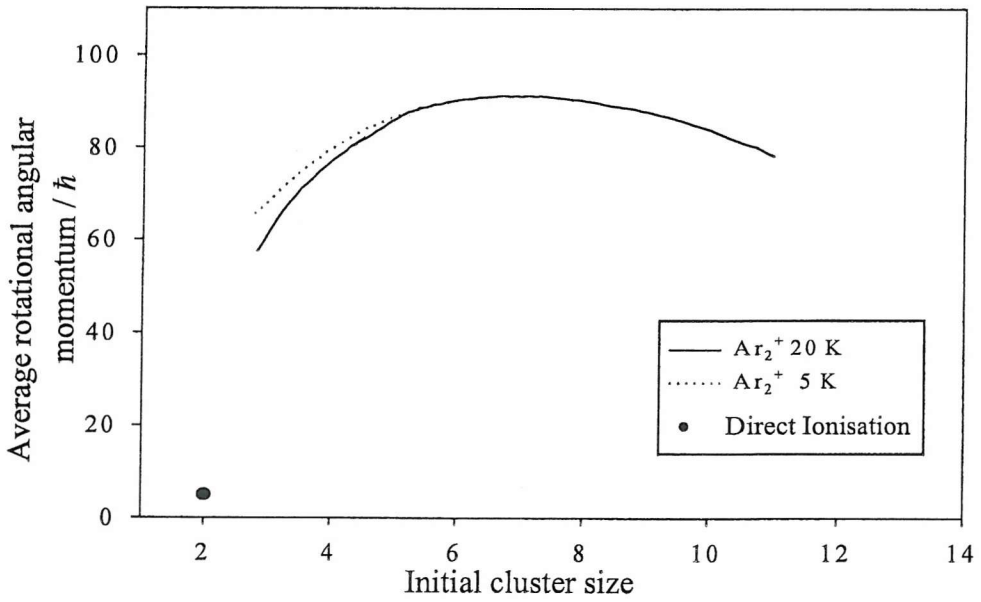

Figure 5.3 Average rotational temperature predicted for the product ion Ar_2^+ resulting from the decay of cluster ions in the range Ar_3^+–Ar_{14}^+ at two initial temperatures: — 20 K; ····· 5 K. Indicated by • is the average rotational angular momentum appropriate for the direct (vertical) ionisation of Ar_2. [141]

Experiments on the infrared photodissociation of Ar_2^+ [144] have produced kinetic energy spectra that show the presence of two such components; a structured component indicative of a low rotational temperature, and an unstructured feature that increases in prominence as the backing pressure is increased. More recently, Woodward *et al.* [143] studied the infrared photofragmentation of Ar_2^+ generated via the adiabatic expansion of argon in a beam. They found that the photodissociation signal from Ar_2^+ increased dramatically as the nozzle stagnation pressure was increased above ~1.7 bar (compare this value with P_L discussed in Section 5.3.1). This result is shown in Figure 5.4 (a). This large increase in photodissociation signal shows that the higher backing pressures populate a significantly larger proportion of Ar_2^+ in rotational / vibrational or electronic states near to the dissociation limit.

A similar experiment was carried out as part of the current investigation, since it gives direct evidence of the origin of the Ar_2^+ that reaches the end of the microwave interaction region. Although these results cannot be quantitatively compared with those of Woodward *et al.*, they may be compared qualitatively. The magnet was set to transmit Ar_2^+ and a large voltage of 3.5 kV was applied to the electric field lens. The total Ar^+ signal due to electric field dissociation was then monitored as a function of backing pressure (up to 3.5 bar – above this pressure the pumping efficiency is dramatically reduced and reliable results could not therefore be guaranteed). The results are shown in Figure 5.4 (b); each data point has been normalised with respect to the intensity of the parent Ar_2^+ ion signal. If the electric field dissociation signal had been derived only from dimers obtained by vertical ionisation then a straight line of slope zero would have been expected, *i.e.* as seen over the pressure range 0.5 – 1.5 bar. However, the substantial increase in Ar^+ signal above ~1.5 bar showed that higher backing pressures favoured the formation of Ar_2^+ in near-dissociation states. This is taken to be an indication that much of the Ar_2^+ detected at these higher pressures has been formed by the breakdown of larger clusters.

To account for such behaviour, it is proposed that following ionisation, argon cluster ions fragment to give dimer ions in excited vibrational / rotational levels in both the electronic ground and excited spin-orbit states.

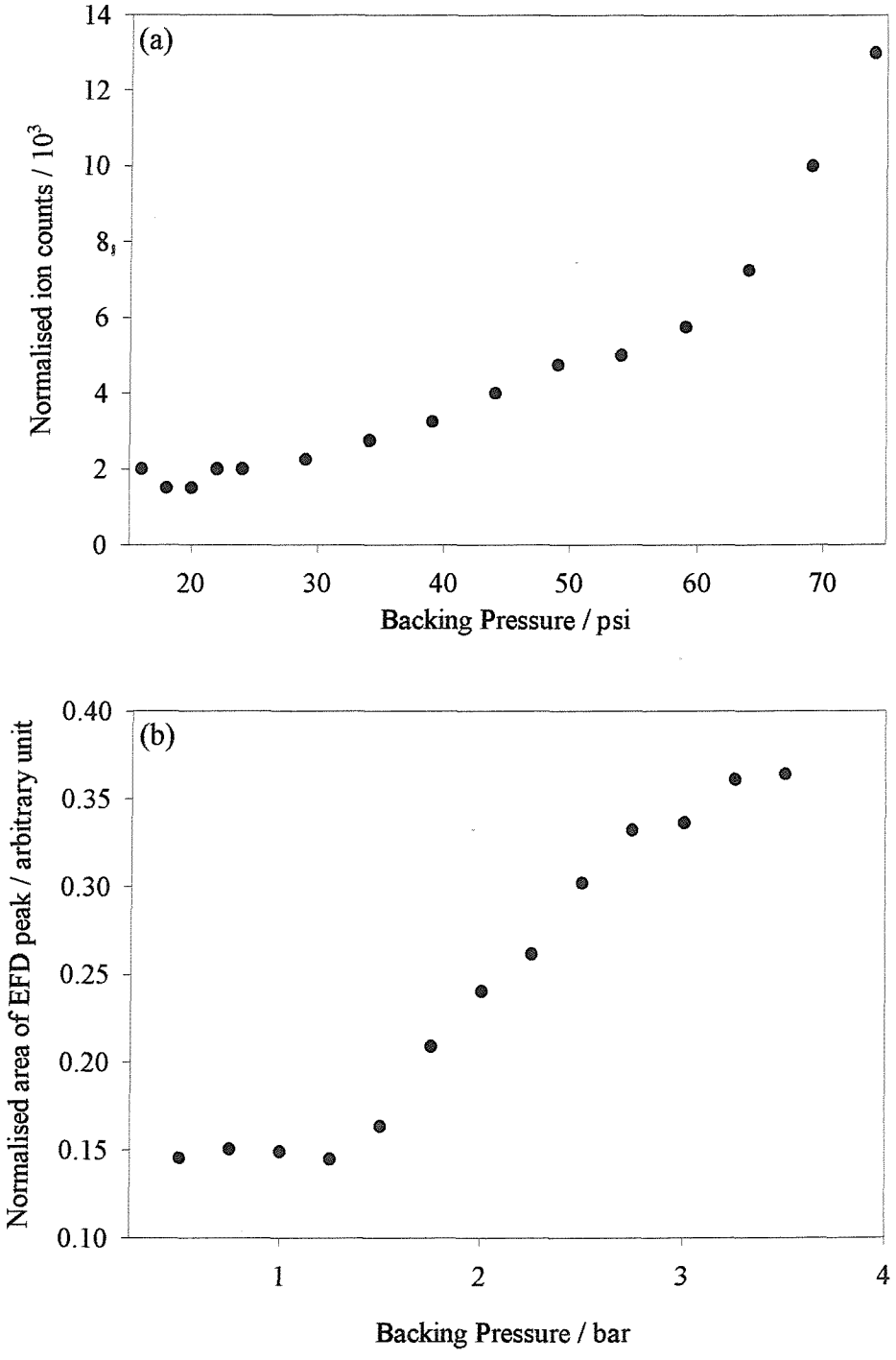

Figure 5.4: (a) Ar^+ photofragment intensity as a function of increasing nozzle stagnation pressure. Each data point has been normalised with respect to fluctuations in laser power and Ar_2^+ parent ion signal [143]. (b) Ar^+ electric field dissociation intensity as a function increasing nozzle stagnation pressure. Each data point has been normalised with respect to the change in Ar_2^+ parent ion signal.

This experimental result, combined with all the previous experimental and theoretical work discussed above, provides conclusive evidence that the Ar_2^+ being studied in the current investigation has been formed by the breakdown of larger clusters. If the predictions of Stace [141] are broadly correct, then it is expected that Ar_2^+ formed in this way will be rotationally hot and therefore resolved Zeeman spectra would not be expected from the current experimental set up. Even though a prediction of rotational temperature has been given by Stace [141], no experiment has yet succeeded in placing a rotational temperature on Ar_2^+ that is expelled from larger clusters. Study of the Zeeman spectra obtained in the current investigation may yield such information even if this is not apparent at first sight. This close inspection of the Zeeman spectra obtained is now discussed.

5.4 Simulations of Zeeman patterns

As for Ne_2^+, J must take values that are half integer ($J = 1/2, 3/2, 5/2....$). When considering the simulation of Zeeman patterns in a system such as Ar_2^+ it is important to note that there are only a limited number of types of Zeeman pattern possible when a field is applied to a TE_{10} mode. All $\Delta J = 0$ Zeeman patterns simply broaden with increasing field - unless the individual components are resolved, such transitions will not display any splittings. However, $\Delta J = \pm 1$ transitions produce two branches which, depending on the g-factors, may be arranged in one of three ways:

1) "back-to-back triangles" (Figure 5.5 (a)),
2) "tip-to-tip triangles" (Figure 5.5 (b)),
3) or the two branches may cross to varying amounts.

As discussed in Section 5.2, none of the near-dissociation transitions observed in Ar_2^+ displayed a resolved Zeeman pattern when subjected to an external magnetic field. There did, however, appear to be two common ways in which the transitions behaved in the presence of an external field. Either, they (1) simply appeared to broaden, or they (2) broadened at low fields and displayed a splitting into two at higher fields.

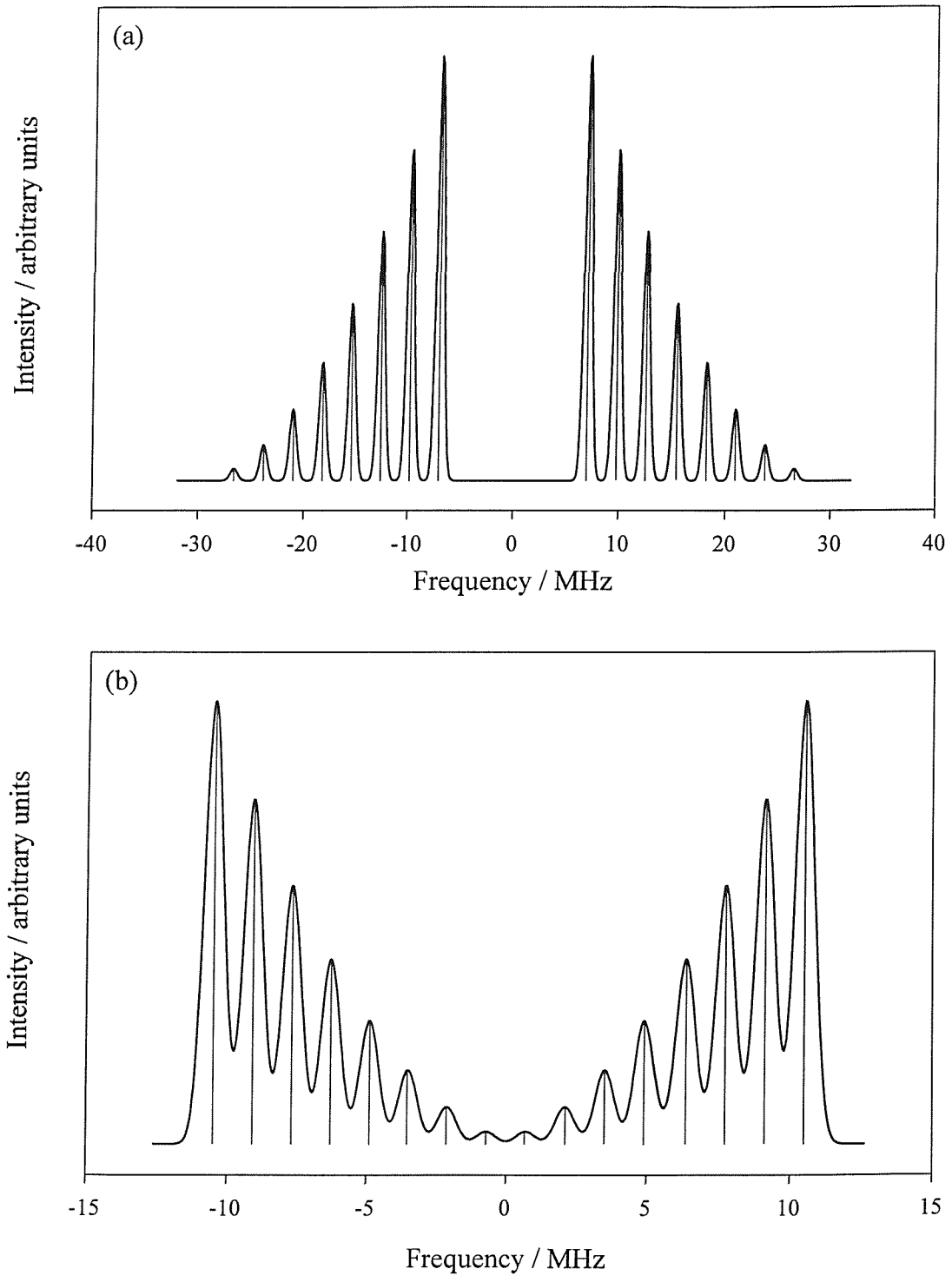

Figure 5.5: $\Delta J = 1$ transitions may produce Zeeman patterns whose individual components appear to form either (a) back-to-back triangles, or (b) tip-to-tip triangles, depending on the intensities of each component.

It was also noted that the rate of change of the broadening with increasing applied field appeared to be different for each of the transitions. Keeping these qualitative characteristics in mind, it seemed possible to investigate this further, with the aim of estimating the rotational quantum number, *J*. As mentioned in Section 5.2, the zero-field recordings of most of the transitions were either very poor or they were not observed single-photon. Unfortunately, it was possible to record Zeeman spectra at different fields of only *two* of the transitions in Ar_2^+: the transitions at 16187.0 MHz and 16952.5 MHz but only the latter could be studied in any detail. Whilst it was hoped that the transition at 16187.0 MHz would also be studied in detail, the signal-to-noise ratio was so poor that this was not possible. This is an incredibly disappointing situation, but a very clear indication of the experimental difficulties encountered in the study of Ar_2^+.

The transition at 16187.0 MHz simply broadened in the presence of an external field [(1) above], whereas the transition at 16952.5 MHz displayed the splitting into two at higher fields [(2) above]. The simulations for the transition at 16952.5 MHz were considerably more fruitful and are discussed below.

16952.5 MHz transition

It is worth noting that the 16952.5 MHz transition has a FWHM of ~2.0 MHz in zero applied field (*c.f.* the 'normal' linewidth observed in this apparatus of ~0.8 MHz). As previously mentioned, this observation is attributed to broadening from the Earth's magnetic field and other local residual fields, an observation also noted in a few of the Ne_2^+ transitions. The field inside the coil when no field is applied is estimated to be *ca.* 0.5 G, and this adjustment has been accounted for in the simulations.

To ensure that excessive microwave power levels did not add further width to the Zeeman spectra, power levels used when recording Zeeman spectra were those found to be optimal for that transition in zero applied field. Therefore, because the transition could not be exposed to high power levels, the Zeeman spectra needed long periods of signal-averaging (often > 30 scans). The signal-to-noise ratio was still fairly poor, even after so many scans, and thus it was not always clear which features were genuine and which were noise. A Savitsky-Golay smoothing filter [145] was

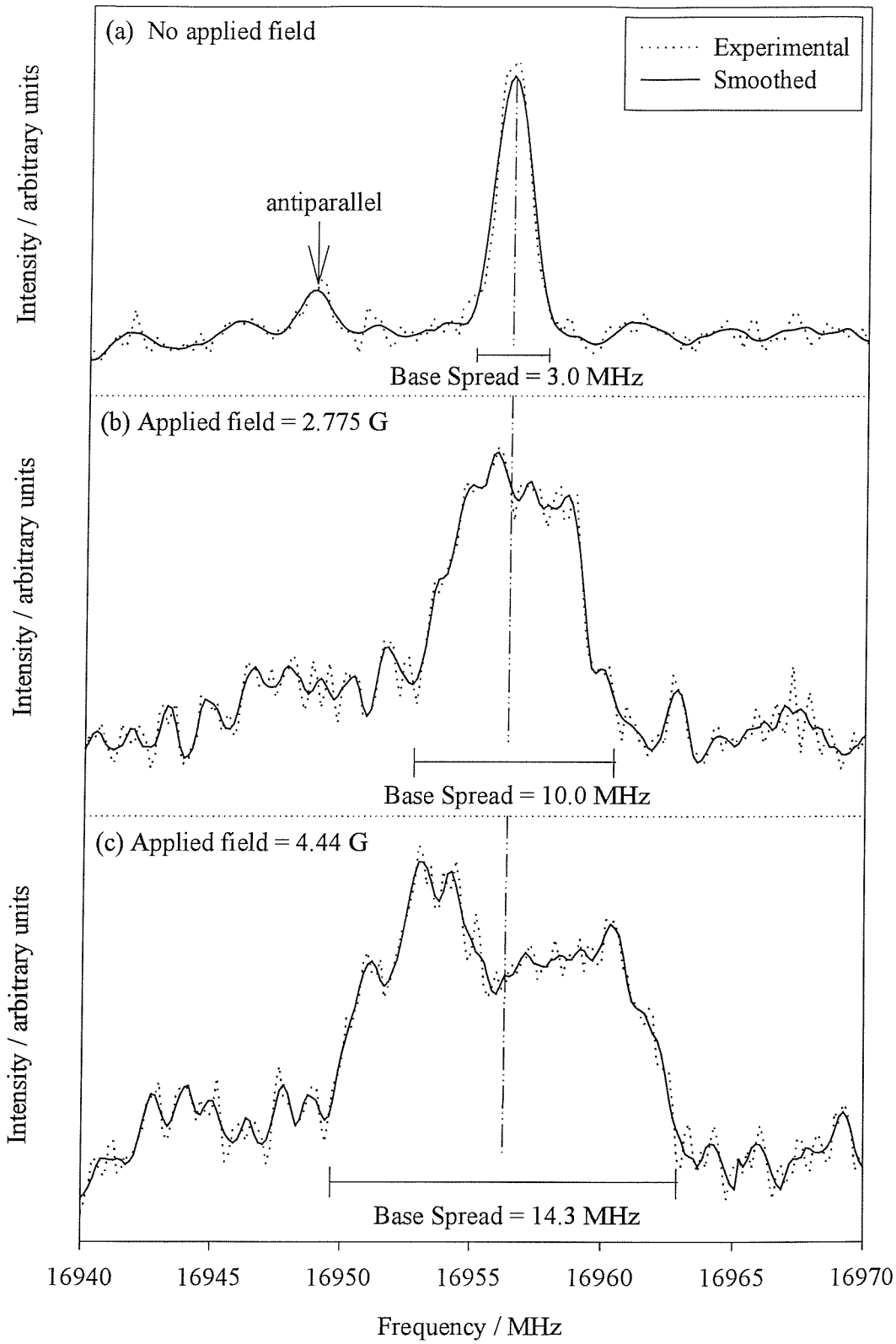

Figure 5.6: The effect of using a Savitsky-Golay smoothing filter [145] of window size 17 data points and polynomial of degree 6 on the 16952.2 MHz transition. The definition of "base spread" is also shown.

Measured field / G	Base spread / MHz	Zeeman spectrum structure
0.5	3.0	One broad unstructured feature
2.775	10.0	One broad unstructured feature
3.33	12.0	Two broad, joined features
4.44	14.3	Two broad, joined features
5.55	18.3	Two broad, joined features
8.33	25.5	Disappeared into noise

Table 5.6: To show how the 16952.5 MHz transition changes with applied magnetic field.

therefore employed. To determine the most appropriate combination of smoothing parameters, various sets were tried on a sample group of Ne_2^+ transitions, and the combination that reproduced the spectra most accurately was then used for the 16952.5 MHz transition in Ar_2^+. The most appropriate set of parameters was found to be a window size of 17 data points and polynomial of degree 6. The resulting smoothed Zeeman patterns obtained at three sample fields are shown in Figure 5.6.

It is possible to define key characteristics of the Zeeman spectra recorded at varying fields (Table 5.6), *e.g.* description of the *structure* of the Zeeman spectra. As with all recordings of spectra using this apparatus, intensity and radiation power levels are not useful comparative variables due to the indirect nature of detection. It is for this reason (although it is not immediately clear) that the attribute "base spread" (see Figure 5.6 for definition) was chosen as a comparative measure rather than the traditional full-width half-maximum (FWHM). This point will be discussed in detail later in this section.

Even though it is possible to apply external fields up to 44 G, it was found that at fields greater than *ca.* 8 G the Zeeman spectra disappeared into the noise and hence such recordings were deemed not to be useful. It should be noted that no peaks were resolved, even at the highest recorded fields.

Since the spectra at the higher fields clearly show more than just one unstructured feature, it was concluded that $\Delta J = \pm 1$. Since none of the recorded Zeeman spectra displayed resolved peaks, it was assumed, at least initially, that J was relatively high ($> 21/2$). The experience gained from the Ne_2^+ study suggests that it

may be safe to assume case (e) coupling for $J \geq 15/2$, and simulations were therefore performed between $J = 21/2$ and $J = 121/2$ with the appropriate case (e) g-factors. All allowed combinations of g-factors were used, strictly observing the selection rules $\Delta J = \pm 1$, $\Delta R = \pm 1$ and $g \leftrightarrow u$.

At a simulation field of 5.55 G, the simulations were consistently too narrow ($\approx$ 2 MHz) or too broad ($\approx$ 40 MHz) (*c.f.* experimental $\approx$ 18 MHz). Simulations were then performed allowing 10 % deviation from the pure case (e) g-factors, again for $21/2 \leq J \leq 121/2$. The study of Ne_2^+ showed that even when a case (e) description was more appropriate than Hund's case (c) the $\Delta R = \pm 1$ selection rule was not always strictly obeyed. Therefore simulations of the two $\Delta R = \pm 3$ transitions were also performed. Although some combinations of parameters produced simulated Zeeman patterns closer to those obtained experimentally they were still obviously incorrect. Allowing a 20 % tolerance either side of the pure case (e) g-factors produced some more promising simulations, but then the validity of such simulations was severely questioned.

BOUND calculations [146] then became available, and contrary to the work on Ne_2^+, they suggested that at high J Hund's case (c) is more appropriate than case (e) coupling. New simulations were therefore performed in a Hund's case (c) basis. Since the g-factors calculated for $\Omega = 3/2$ are the same for either g or u states (see Table 2.1) then any of these may be taken in combination with any of the calculated $\Omega = 1/2$ g-factors (assuming $\Delta J = \pm 1$ is preserved). It was soon found that assuming the lower J to be $\Omega = 1/2$ and the upper J to be $\Omega = 3/2$ produced simulations of approximately the same base spread as had been observed experimentally for the 16952.5 MHz transition.

It is interesting to note that for a given correct combination of J and g-factors the base spread varies very little for $J = 19/2$ to $J = 99/2$ and it may therefore seem impossible to progress further with this investigation of estimating J. It was quickly seen, however, that a lower bound could be put on the rotational quantum number by considering for what J values the pattern should still be resolved at 5.55 G. Figure 5.7 shows that with increasing J the Zeeman simulation becomes less resolved until at lower $J = 25/2$ it would not be expected to resolve the pattern experimentally. A lower bound of $J = 25/2$ was therefore concluded for this transition.

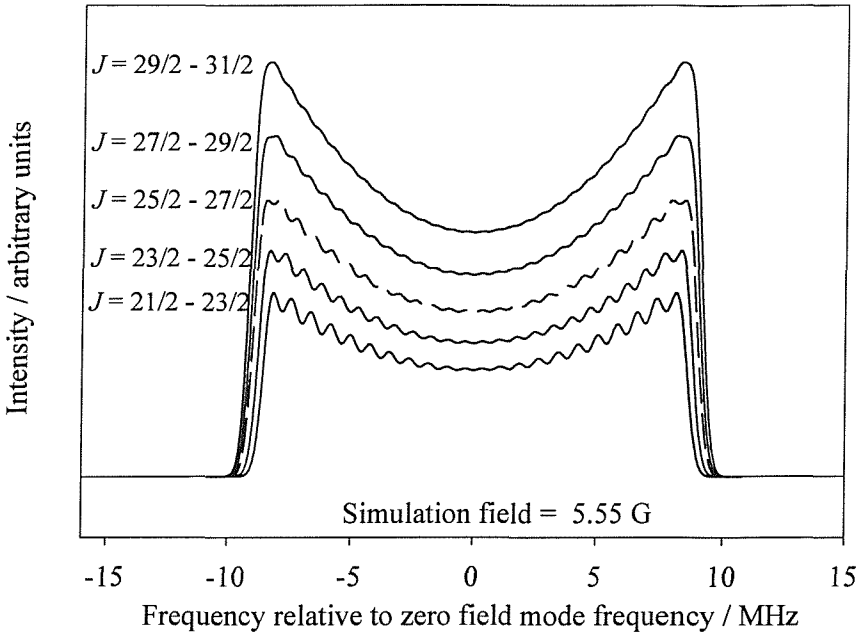

Figure 5.7: Simulations at 5.55 G for $\Delta J = \pm 1$ transitions using pure case (c) g-factors (see text for details). It can be seen that at this field only transitions with a lower $J =$ 25/2 (shown by a broken line) or less would be expected to resolve experimentally.

Although only relatively small, the variation of base spread with applied field was investigated as a function of J. It was found that there is enough change in the simulations to make meaningful measurements. The variation of base spread with applied field for simulations of different J is shown in Figure 5.8, along with the experimental results. The raw experimental results are shown as circles, and a linear least-squares fit through these points is also shown (in black). It may be seen that the simulated spectra clearly display the correct type of behaviour with changing field. The experimental least-squares line lies between the $J = 25/2$ and $J = 41/2$ simulation lines, suggesting these are the lower and upper bounds on J for this particular transition. Plotting the *slopes* of these lines against J places even narrower bounds on the value of J, and as Figure 5.9 shows, lower J for this transition is determined to be between $J = 25/2$ and $J = 29/2$. The error in this value originates from the deviation of the least-squares fit through the raw experimental results. The gradient of the least-squares fit is good to 3 %, enabling such a good determination of J to be given.

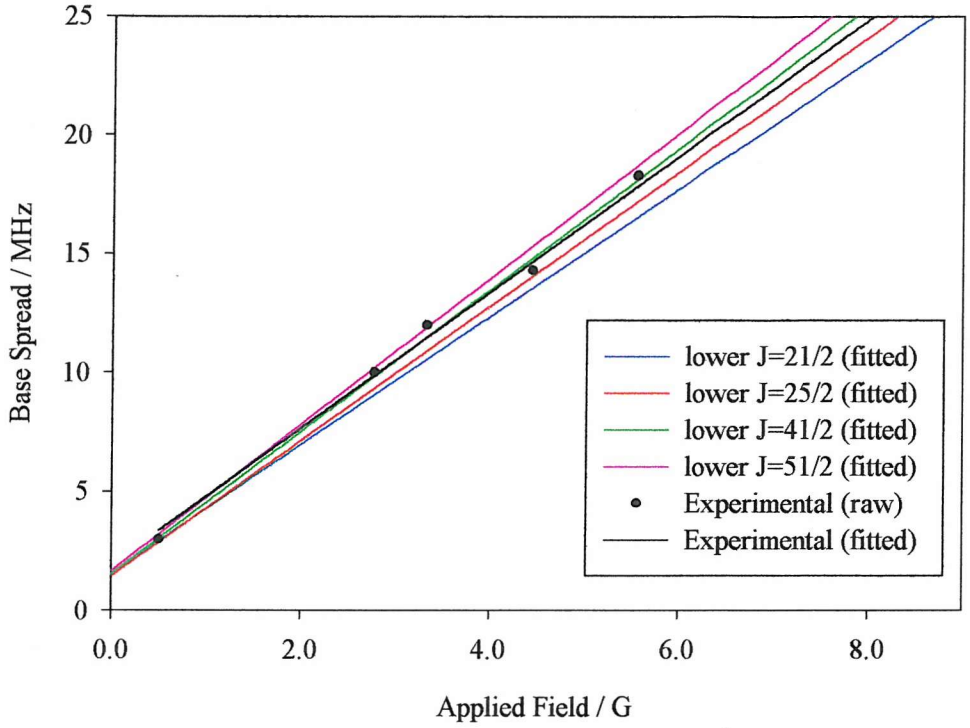

Figure 5.8: The variation of base spread with applied field for simulations of different J, along with the experimental results. The raw experimental results are shown as circles, and a linear least-squares fit through these points is also shown (in black).

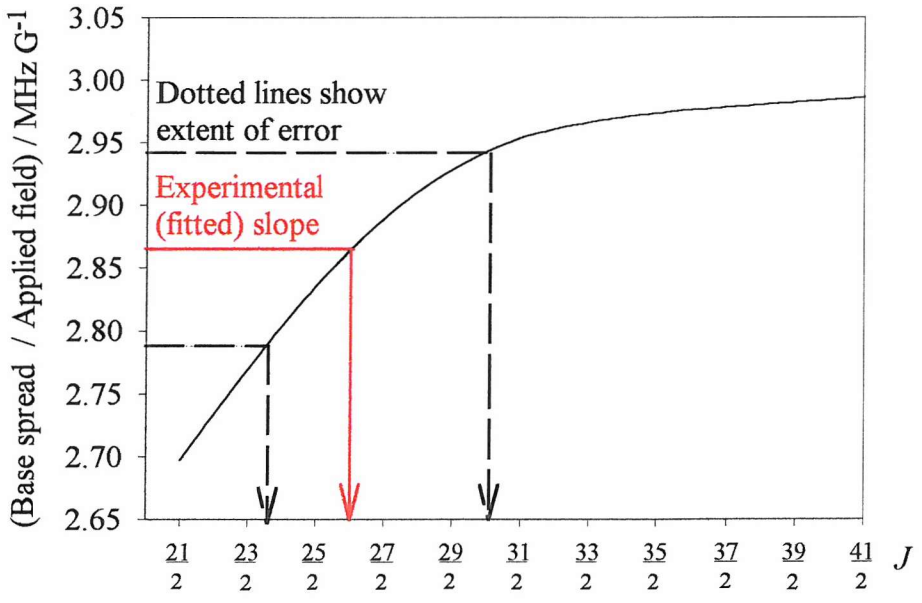

Figure 5.9: Plotting the *slopes* of the lines in Figure 5.8 against J places narrow bounds on the value of J. Lower J for this transition is determined to be between $J = 25/2$ and $J = 29/2$.

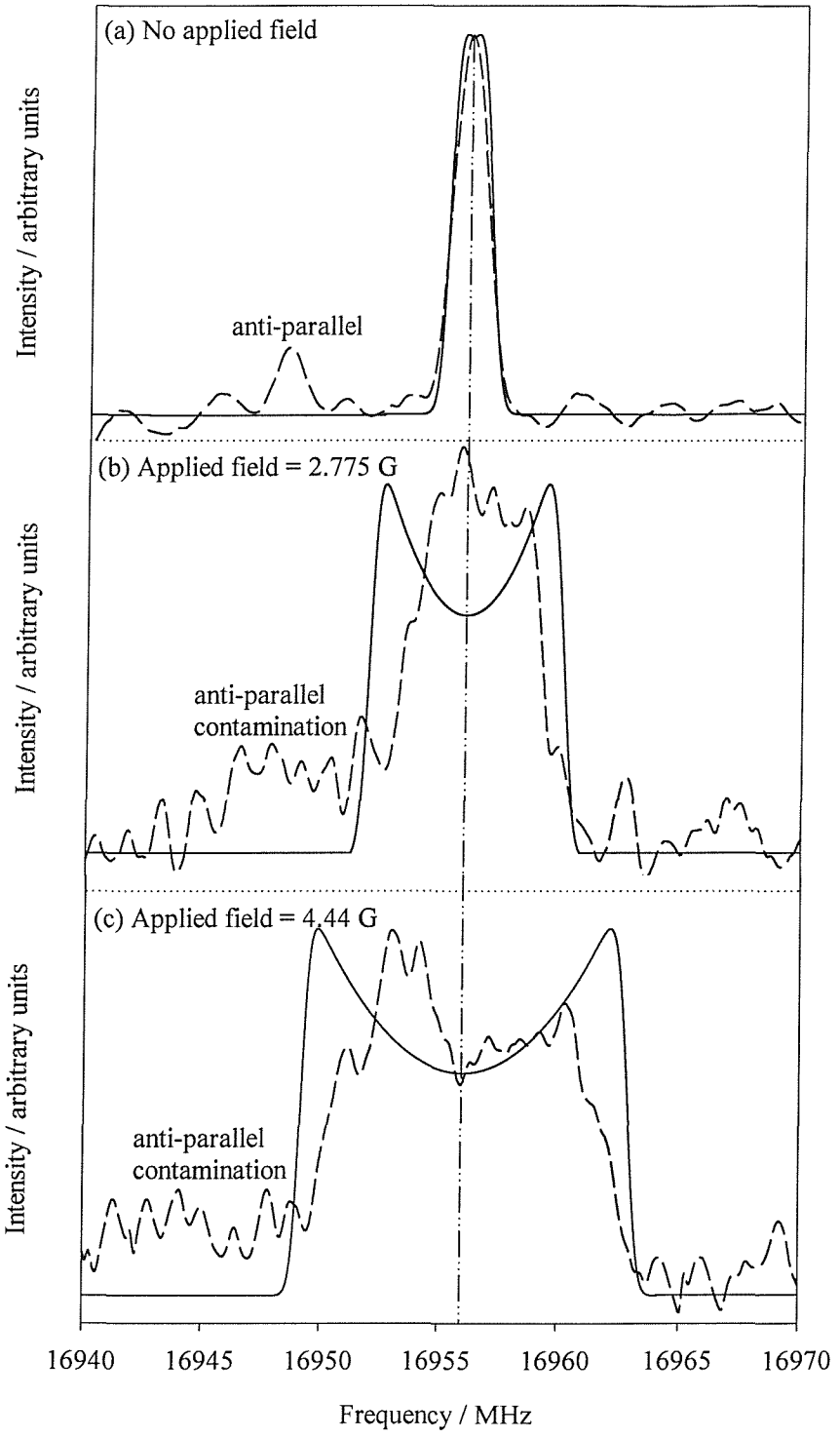

Figure 5.10: Experimental and simulated spectra of the 16952.5 MHz transition of Ar_2^+ at various fields: (a) zero applied field, (b) 2.775 G and (c) 4.44 G.

	level 1	level 2
J	27/2	29/2
Ω	1/2	3/2
g	0.097	0.013

Table 5.7: The assignment of the 16952.5 MHz transition of Ar_2^+.

The transition at 16952.5 MHz is therefore assigned as $\Delta J = \pm 1$, with lower $J = 27/2$ "$\pm$ 1", as shown in Table 5.7. Figure 5.10 compares the simulated spectra to the experimental spectra at three fields. It can be seen that the base spreads of the simulations at all fields are good, and the two-branch structure is recreated at high field. The anti-parallel contribution is not included in the simulations, but contamination is clearly seen in the experimental spectra.

Although the base spread and structure of the spectra are fairly well recreated in these simulations, there are very obvious problems with the simulations and these relate entirely to the *intensity* of the simulations. For example, the simulations at 2.775 G and 4.44 G (Figure 5.10 (b) and (c)) clearly have too much intensity at the extremes of the spectra, and conversely not enough intensity in the middle. This causes the shape of the simulations to be wrong, including the sides of the simulations being too "vertical" and the simulations predicting a resolvable two-branch structure at 2.775 G, even though experimentally only one was seen. It now becomes clear why "base-spread" was chosen as a key characteristic rather than the FWHM – choosing the latter would have caused great difficulties during the simulation process.

The question then arises of why the intensities in the simulations are so clearly incorrect. The best spectra to use as a comparison are those whose assignments are known, *i.e.* transitions in Ne_2^+ (Chapter 4). Figure 5.11 (a) shows the experimental recording of the 29354.2 MHz transition in Ne_2^+ (as previously displayed in Figure 3.7 (b)) and similarly, Figure 5.11 (b) shows the 27306.9 MHz transition. The assignments and g-factors for these transitions are known with 100 % certainty and the simulations of these transitions are also shown. It can be seen that the positions of the peaks in the simulations match the experimental spectra well. It is clear, however,

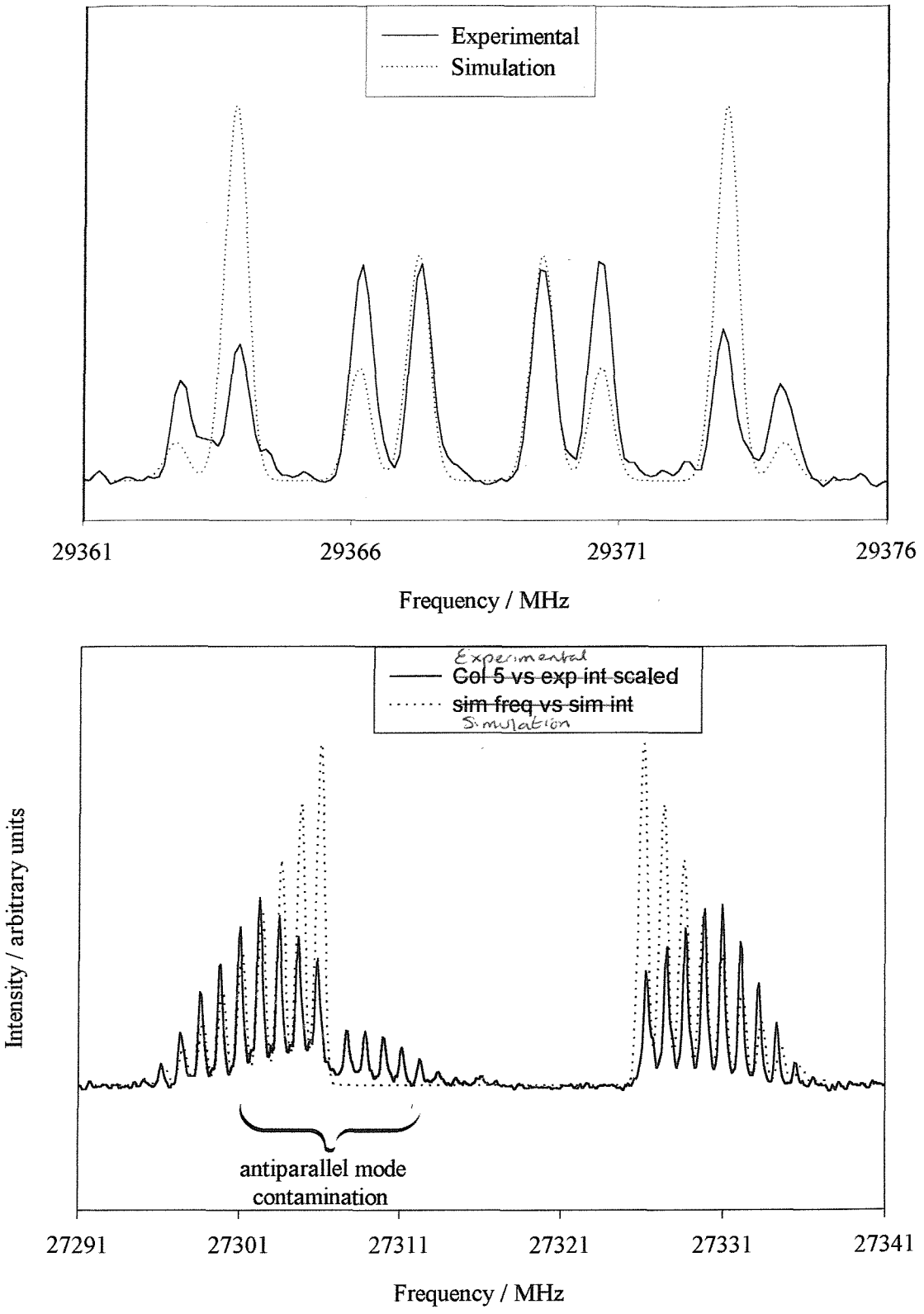

Figure 5.11: Experimental and simulated spectra of (a) the 29354.2 MHz transition and (b) the 27306.9 MHz transition, both in Ne_2^+. Although the frequencies of the peaks are correctly predicted by the simulations, the intensities are not.

that the experimental intensities do not agree with those simulated. In particular, it may be noted that it is the components expected to have the *highest* intensity that lose the most. This observation is also noted for many other transitions in Ne_2^+, and there is no reason why this phenomenon may not also be seen in Ar_2^+. Indeed, it has recently been found in a similar study of HeH_2^+ [37] that intensity predictions for Zeeman spectra cannot be relied upon. It has been suggested that an unknown experimental factor is involved, such as the time-dependence of the microwave perturbation. However, the key learning for the current discussion is that it is not unexpected that the peak intensities are incorrectly predicted by the simulations.

Unless even higher resolution scans of this transition's Zeeman spectra become available, it is unlikely that the current assignment could be confirmed. However, the simulations performed were fairly exhaustive, and the current assignment is the only one that provided predictions similar to the experimental spectra. It is therefore entirely reasonable to believe that the assignment is correct, despite the shortcomings of the intensity predictions.

5.6 Discussion and concluding remarks

Although 69 microwave transitions have been recorded in the near-dissociation spectrum of Ar_2^+, the assignment of these transitions has been impossible. Only one of these transitions has been assigned, using an unresolved Zeeman spectrum. Clearly, on this basis it has not been possible to construct potential energy curves as was possible for the study of Ne_2^+ (Chapter 4). Whilst the aim of this study was then altered to provide an estimate of the rotational temperature of Ar_2^+ formed in the apparatus, this too has not been possible since only one transition has been assigned. The assignment of the transition observed at 16952.5 MHz is $J = 27/2$ to $J = 29/2$, which is rotationally hotter than all of the assigned transitions of Ne_2^+. However, it is not *extremely* hot, as may be expected from the calculations of Stace [141], although this assignment does not necessarily suggest that Stace's calculations are incorrect. Indeed, perhaps the reason why it was not possible to record Zeeman spectra for the majority of the observed transitions is because they are so much hotter than any previously studied. Applying an external field splits the transition into so many

components that each component retains so little intensity that under the present experimental conditions, it would *never* be possible to record a Zeeman spectrum.

However, it *has* been possible to show (both experimentally and theoretically) that the Ar_2^+ studied was formed by the breakdown of larger ($n > 3$) clusters (Figure 5.4 (b) and the associated discussion). As has been shown by the resulting experimental difficulties, it is unlikely that the current experimental set up would ever yield spectra that would lead to the assignment of the transitions and ultimately to the construction of potential curves. It is therefore recommended for future work that efforts are concentrated on reducing the formation of clusters in the beam. This may be achieved by heating the nozzle, reducing the backing pressure (assuming that the beam current remains large enough to utilise) and using a smaller nozzle (*e.g.* 10 μm). This latter point assumes that the gas used is free from impurities, so as to ensure that the nozzle does not block as it did in the current investigation. This may not be possible, but perhaps investing in either high purity argon or a suitable filter may resolve this problem.

Further work on this investigation may also focus on reducing the line-width of peaks in spectra, so as to increase the possibility of recording resolved Zeeman patterns. This may not be possible, but it is worth investigating the effect of minimising local residual fields or increasing the length of the microwave interaction region so as to increase the interaction time. However, this would require large, expensive alterations to the apparatus and may not result in clearer spectra: by virtue of its lighter weight, Ne_2^+ spends less time in the microwave interaction region than Ar_2^+ and therefore it may be expected that the peaks would be broader. However, the converse of this is observed, and therefore it may be concluded that it is not the uncertainty principle that is the cause of broad peaks in Ar_2^+.

Further searches for transitions in Ar_2^+ could be made by extending the frequency range to > 140 GHz and to < 14.1 MHz. Although it is highly likely that more transitions will be found in these regions, it is unlikely that they will provide great amounts of information that would allow this investigation to progress further. Investing in further microwave multipliers would increase the likelihood of recording positive double resonance results, but it is questionable whether this would be a wise investment without addressing the causes of experimental difficulty.

Ultimately, it may not be possible to study fully the near-dissociation spectrum of Ar_2^+ in the current apparatus. It may be possible, however, to study larger argon clusters, such as the trimer, Ar_3^+, since it is known that this is currently formed in the beam. Such a study may be interesting and useful to the ongoing debate as to the core of argon clusters. Ar_3^+ is expected to have similar electronic states to those of Ar_2^+, since combining a completely symmetric $^1S_0$ Ar atom with Ar_2^+ does not generate any states with new symmetries. According to the supporting calculations of Wadt [147], Ar_3^+ will have the same dipole-allowed electronic transitions as Ar_2^+. A preliminary study of Ar_3^+ has yielded some near-dissociation transitions, but at the time of writing these have not been investigated.

Chapter 6 – Final conclusions

This thesis has reported the studies of the near-dissociation states of two rare-gas ion complexes: Ne_2^+ and Ar_2^+. As discussed in Chapters 2 and 3, a number of experimental tools have been utilised to allow this investigation to be completed. The merits and performance of these will now be reviewed.

Ne_2 produced in a supersonic molecular beam is subsequently ionised, leading to the formation of sufficient Ne_2^+ ions in near-dissociation states to allow spectroscopic investigation. This method has clearly been very successful in the study of Ne_2^+ (Chapter 4), however it has not been so successful in the study of Ar_2^+ (Chapter 5). Although this second molecular ion clearly has population in near-dissociation states to allow microwave transitions to be observed, there is clear evidence to suggest that these ions have *not* been produced via the intended route. Instead, due to the clustering nature of argon, near-dissociation states have been produced from larger clusters falling apart to give rotationally hot Ar_2^+. Section 5.6 suggests a number of ways in which the apparatus could be altered to overcome this problem. However, none of these suggestions are trivial and the question of high cost must surely be balanced against the possible knowledge gained.

This said, however, alternative modification of the apparatus may prove more fruitful for a number of other systems. Attempts have been made to study a number of other van der Waals molecules (*e.g.* RgCO, $RgCO_2$, RgN_2, RgH_2O) but the ionisation of none of these species has resulted in significant population of near-dissociation states. It is quite possible that the study of these ions fails due to small nascent beams rather than insufficient population of near-dissociation states. This is indeed the case for Kr_2^+: the large number of isotopes means that only a small percentage of the beam is the desired isotope, which prevents any particular isotopes being studied. Alternatively, a completely different method of producing ions could be envisaged. For example, laser ablation or plasma generation would enable the generation of a range of species that are not possible to study currently (*e.g.* ArOH as precursors for $ArOH^+$). It is questionable, however, whether these 'seeding sources' could be stable for sufficiently long periods of time.

The second section of the apparatus that could be changed in the future is the microwave interaction region. The current set-up clearly works well, but some difficulties are encountered. These are normally with regard to the frequency multipliers and double resonance experiments. The magic-T clearly has optimal ranges for frequency mixing, but a number of experiments are impossible due to either not being able to combine radiation from the two sextuplers (for example) or limitation in the range of the second synthesiser. The expense of such pieces of equipment are quite high, but time investment would be low and therefore investment in further microwave equipment is recommended, especially for the later stages of a study, when the linking of new levels becomes more difficult.

Employing higher frequency radiation would allow observation of transitions to more strongly bound levels and thus help tie down new vibrational stacks, that will help the coupled-channel calculations for Ne_2^+. This would, however, require the abandonment of the existing waveguide technology and careful thought would need to be given to potential losses versus gains.

An exciting challenge would be to investigate the use of multipass technology, to increase the effective length of the interaction region. It is not clear, however, how feasible it is to incorporate this into the existing apparatus.

The final part of the apparatus for which suggestions for upgrade are given is for the detection system. The current design of the electric field lens clearly works extremely well, indicated by the fantastic results presented for Ne_2^+ in Chapter 4. However, the depth to which it can probe the potential well is limited and investigating ways of providing a lens able to dissociate further down the well is an exciting possibility.

Alternatively, it is possible to create a lens that has greater state selectivity [59]. This would allow for easier investigation of weaker transitions, however it would be a hindrance for blind scanning.

Although the current data capture method is run by PC, updating the electron multiplier and associated electronics may improve the efficiency of signal detection.

The systems discussed in this thesis are both diatomic, as are the majority of the systems previously studied with this apparatus. However, one triatomic system

has also been studied to date: HeH_2^+. This presents a significant set of new challenges but also opens up the possibility of future work concentrating on systems larger than diatomics. As mentioned in Section 5.6, Ar_3^+ is a potential new system to investigate, although without modification to the molecular beam chamber this is likely to suffer similar problems as the study of Ar_2^+.

The current experimental apparatus provides the possibility of detailed information about the nature of long-range intermolecular forces and the resulting bond formation. However, as was seen in both Chapters 4 and 5, high quality theoretical work is imperative for interpretation of data.

Appendix

Microwave transitions observed in $Ne\cdots Ne^+$, and their assignments (where known). Level numbers are given with reference to Figure 4.5. [a] Where only a frequency is given, the transition is yet to be assigned, [b] When a frequency is known to an accuracy of only 1 MHz it is stated with no decimal place.

	g state		*u* state	
Frequency / MHz [a,b]	*J*	Level	*J*	Level
7204.8				
7440.0	7/2	49	9/2	64
8702.4	3/2	16	5/2	32
9448.7	5/2	30	5/2	32
10381.2	7/2	41	7/2	42
10961.8				
10997	9/2	58	11/2	74
11259.6	15/2	90	17/2	95
11491.0	9/2	57	7/2	42
11534.2	7/2	46	5/2	32
11603.9	3/2	10	3/2	11
11773.5	9/2	65	7/2	51
13841.3	1/2	3	3/2	12
13918.2	9/2	61	7/2	47
14036.2	5/2	30	7/2	48
14520.2	7/2	43	5/2	27
15590.9	3/2	10	1/2	2
16377.9	5/2	25	7/2	42
16875.0	7/2	49	5/2	35
17021.2	5/2	36	5/2	34

Appendix: (*Continued*)

	g state		*u* state	
Frequency / MHz [a,b]	*J*	Level	*J*	Level
17257.8	3/2	9	3/2	11
17270.7	9/2	66	11/2	79
17870.3	7/2	46	9/2	63
18186.1	7/2	41	5/2	26
18550.0	5/2	36	7/2	51
18586.3	7/2	49	7/2	52
19107.5	7/2	54	7/2	51
19446	7/2	49	9/2	63
19664.9	7/2	49	9/2	67
19804.4	9/2	65	11/2	80
20087.1	9/2	65	7/2	52
20495.5	9/2	58	9/2	59
20851.2	5/2	28	7/2	44
20913.3	5/2	24	3/2	11
21019.9	9/2	70	7/2	51
21148.0	9/2	58	7/2	44
21165.7	9/2	65	9/2	67
21238.9	11/2	81	11/2	79
21244.7	3/2	9	1/2	2
21315.0	17/2	94	15/2	91
21408.0	3/2	22	5/2	34
21517	5/2	39	5/2	34
21986.4	9/2	65	11/2	78
22239.5	3/2	22	3/2	20
22260.0				

Appendix: (*Continued*)

	g state		*u* state	
Frequency / MHz [a,b]	*J*	Level	*J*	Level
22342.8	5/2	36	3/2	19
22348.1	5/2	39	3/2	20
22561	3/2	21	3/2	19
22742.3	11/2	77	11/2	79
22765.9	7/2	43	9/2	59
23101.6				
23161.3	5/2	29	5/2	32
23167	7/2	50	5/2	38
23233.7	11/2	75	11/2	74
23418.6	7/2	43	7/2	44
23477.5				
23559.0	7/2	50	7/2	55
23868.2				
23909.6	7/2	50	9/2	71
24184.3	5/2	25	5/2	26
24434	13/2	85	11/2	74
25221.5				
25223.6				
25226.5	11/2	77	13/2	88
25644	9/2	61	11/2	76
25744.3	1/2	7	1/2	6
25781.7	7/2	49	5/2	32
26171.7	9/2	68	11/2	79
26683.3				
26692.5	7/2	45	9/2	63

Appendix: (*Continued*)

	g state		*u* state	
Frequency / MHz [a,b]	*J*	Level	*J*	Level
26881.5	11/2	77	13/2	87
27306.9	9/2	61	11/2	78
27694.6	7/2	49	9/2	69
28434.9	3/2	18	5/2	37
28672.3	3/2	13	5/2	27
28797	7/2	50	9/2	63
29178.0	7/2	49	7/2	53
29195.4	9/2	65	9/2	69
29354.2	3/2	10	5/2	26
29384.0				
29392.1	5/2	25	3/2	12
29613.7	7/2	49	5/2	37
29718.9	11/2	73	9/2	60
29749.3	5/2	28	5/2	27
29875.8	7/2	46	9/2	64
29989.7	5/2	33	7/2	55
30151.6	1/2	1	3/2	11
30546.3	7/2	50	7/2	48
30591.3	9/2	65	11/2	82
30678.9	9/2	65	7/2	53
30856.7	5/2	24	7/2	42
31339	3/2	18	5/2	38
31348.2	9/2	61	9/2	63
31600.7	9/2	57	11/2	74
31743.2	7/2	41	5/2	27

Appendix: (*Continued*)

	g state		*u* state	
Frequency / MHz [a,b]	*J*	Level	*J*	Level
32518.7	7/2	49	5/2	38
32812.1	1/2	3	1/2	2
32852.5	7/2	49	5/2	31
33085.5	13/2	84	15/2	92
33094.5				
33260.8	7/2	49	9/2	71
34138.6	1/2	1	1/2	2
34561.9	3/2	10	3/2	12
35374.4	9/2	65	7/2	47
36799.3	1/2	3	3/2	11
37419.8	9/2	58	9/2	60
37741.2	5/2	25	5/2	27
38098	5/2	28	3/2	12
38330.8				
38663.2	5/2	24	5/2	26
39576.0	5/2	28	3/2	15
39663.1				
39690.1	7/2	43	9/2	60
39988.3	7/2	41	9/2	59
40215.4	3/2	9	3/2	12
40476.2	19/2	99	17/2	96
40641.0	7/2	41	7/2	44
40907.6	13/2	84	11/2	76
41099.4	9/2	57	9/2	59
41300.0	7/2	45	9/2	60

Appendix: (*Continued*)

	g state		*u* state	
Frequency / MHz [a,b]	*J*	Level	*J*	Level
41710.0	5/2	30	3/2	19
41752.3	9/2	57	7/2	44
42087				
42229.5	3/2	13	5/2	26
42910.6	3/2	10	5/2	27
43047.2	13/2	84	13/2	86
43477.2				
43747.0	3/2	13	1/2	4
43871.0	5/2	24	3/2	12
44012.0				
44198.5				
44251.9				
45284	15/2	89	13/2	83
45576.8	1/2	5	3/2	15
45748.3	9/2	62	11/2	76
45983.2	5/2	28	7/2	47
46207.6	17/2	98	19/2	101
46639.5	5/2	25	7/2	44
48030.2	17/2	97	17/2	96
48053.9	9/2	61	11/2	79
48419.5	9/2	58	11/2	76
48564.5	3/2	9	5/2	27
48597.9	13/2	85	15/2	93
48816.2	11/2	77	13/2	86
49439.1	5/2	28	3/2	17

Appendix: (*Continued*)

	g state		*u* state	
Frequency / MHz [a,b]	*J*	Level	*J*	Level
49478				
50006.1	5/2	28	5/2	31
50018.2	5/2	36	7/2	48
50964.2				
51082.9	3/2	13	5/2	31
51112.5	5/2	28	7/2	42
51413.0	15/2	90	17/2	96
52220	5/2	24	5/2	27
53110	1/2	1	3/2	12
54759.1				
54766.8	5/2	29	7/2	44
55920.8				
55992.4	3/2	13	1/2	2
56912.6	7/2	41	9/2	60
57076.9	5/2	28	5/2	32
58000.7	17/2	98	19/2	100
58023.5	9/2	57	9/2	60
58153.6	3/2	13	5/2	32
58224.1	7/2	45	9/2	59
58973.5	3/2	14	5/2	27
59979.1	3/2	13	3/2	11
61055.9	5/2	28	3/2	11
61066.2	9/2	61	7/2	51
61117.9	5/2	24	7/2	44
61514.1				

Appendix: (*Continued*)

	g state		*u* state	
Frequency / MHz [a,b]	*J*	Level	*J*	Level
61664.2	5/2	28	7/2	48
63002.1				
63665.0	5/2	29	5/2	27
63832.8	1/2	3	3/2	15
65108.6	19/2	99	19/2	100
65767.3				
65949.2				
66469.7	7/2	45	5/2	27
66847.7				
67323	3/2	14	3/2	12
69023.5	9/2	57	11/2	76
69097.4				
69492.7	11/2	73	13/2	83
72014	5/2	29	3/2	12
73038.2				
74490.9	13/2	85	15/2	91
76493.7	19/2	99	21/2	102
76752.2				
76955.0				
78263.7				
78880.2	11/2	77	9/2	59
81351.5	17/2	94	19/2	100
82681.0				
83177.2	9/2	61	7/2	42
83204.7				

Appendix: (*Continued*)

	g state		*u* state	
Frequency / MHz [a,b]	*J*	Level	*J*	Level
83434.7	17/2	97	15/2	91
83721.5				
84257.3				
84815.6				
87125.9				
87620.0	7/2	41	9/2	56
88184.4	17/2	97	17/2	95
89338.0	5/2	28	3/2	19
89891.8				
90311.7				
90414.6	3/2	13	3/2	19
91233.8				
91720.3				
92633.7	3/2	13	1/2	6
92797.2	11/2	81	13/2	86
93131.0	5/2	28	7/2	51
93480.5				
93494				
93829.6	5/2	28	3/2	20
94807.8				
95738.3	3/2	13	5/2	34
96022.0	11/2	75	13/2	83
96789.3	7/2	50	9/2	60
97223.0	13/2	85	13/2	83
99592.7	5/2	25	7/2	40

Appendix: (*Continued*)

	g state		*u* state	
Frequency / MHz [a,b]	*J*	Level	*J*	Level
99733.2	5/2	28	5/2	35
100810.1	3/2	13	5/2	35
101444.5	5/2	28	7/2	52
101458.5				
104362.2	7/2	49	9/2	59
106166.9				
106964.8				
107255	3/2	10	5/2	23
108202.3				
108655.3				
109608.1				
111947.9				
112360.2	9/2	65	11/2	74
112424.5	5/2	25	5/2	23
113060.8	7/2	50	7/2	44
113594.9	1/2	3	3/2	19
113713.5	7/2	50	9/2	59
113787.0	3/2	18	5/2	27
115479.3				
115529.0	5/2	33	5/2	27
115813.7	1/2	3	1/2	6
116900.6	11/2	73	13/2	88
117002.6	3/2	10	3/2	8
117243.7				
118037.5	17/2	98	15/2	91

Appendix: (*Continued*)

	g state		*u* state	
Frequency / MHz [a,b]	*J*	Level	*J*	Level
118086.3	1/2	3	3/2	20
118240.0	9/2	66	7/2	44
118423.0	7/2	41	5/2	23
118698.0				
119534.5				
120429.6				
121237.1				
121451.7				
121563.9				
121881.3				
121884.3				
121958.8	7/2	50	5/2	27
122117.6	9/2	58	11/2	79
122172.4	5/2	25	3/2	8
122861.1	11/2	81	9/2	59
123866.0	13/2	85	11/2	72
123877.5	5/2	33	3/2	12
124572.8				
124904	7/2	41	9/2	63
125084	9/2	58	7/2	40
126054.1				
126164.4	7/2	49	5/2	26
130239.7				
130414.2				
130457.1				

Appendix: (*Continued*)

	g state		*u* state	
Frequency / MHz [a,b]	*J*	Level	*J*	Level
131059.2				
132424.1				
132470.0	9/2	65	7/2	42
139545.2				
144441.2				
144576.1				
149292.9				
153476.5				

Glossary

AM	amplitude modulated
aug-cc-pV5Z	augmented correlation-consistent polarised valance quintuple zeta
CW	continuous wave
D/A, A/D	digital-to-analogue, analogue-to-digital
DIM	diatomics-in-molecules
ESA	electrostatic analyser
FWHM	full width half maximum
MRCCI + Q	multireference contracted configuration interaction with Davidson-type corrections
MRD-CI	multireference double excitation configuration interaction
MR MBPT	multireference many-body perturbation theory
PC	IBM compatible personal computer
POL CI	polarisation configuration interaction
QCISD(t))	quadratic configuration interaction single and doubles with an additional noniterative treatment of the triple substitutions
RCCSD-T	partially restricted coupled cluster method restricted to single and double excitations
Rg	Rare gas, *i.e.* helium, neon, argon, krypton, xenon or radon
SCF	self-consistent field
TE	transverse electric
TM	transverse magnetic
UMP4	fourth order unrestricted Møller-Plesset perturbation theory
UV	ultra violet (electromagnetic radiation of wavelength 4 – 400 nm)

References

[1] K. K. Verma, M. E. Koch and W. C. Stwalley, *J. Chem. Phys.*, **78**, 3614, (1983).

[2] W. T. Zemke and W. C. Stwalley, *J. Phys. Chem.*, **97**, 2053, (1993).

[3] C. - C. Tsai, T. - J. Whang, J. T. Bahns and W. C. Stwalley, *J. Chem. Phys.*, **99**, 8480, (1993).

[4] B. Ji, C. - C. Tsai, L. Li, T. - J. Whang, A. M. Lyyra, H. Wang, J. T. Bahns, W. C. Stwalley and R. J. Le Roy, *J. Chem. Phys.*, **103**, 7240, (1995).

[5] H. Wang, P. L. Gould and W. C. Stwalley, *Z. Phys. D*, **36**, 317, (1996).

[6] H. Wang, P. L. Gould and W. C. Stwalley, *J. Chem. Phys.*, **106**, 7899, (1997).

[7] X. Wang, H. Wang, P. L. Gould, W. C. Stwalley, E. Tiesinga and P. S. Julienne, *Phys. Rev. A*, **57**, 4600, (1998).

[8] P. D. Lett, P. S. Julienne and W. D. Phillips, *Annu. Rev. Phys. Chem.*, **46**, 423, (1995).

[9] H. Knöckel, T. Johr, H. Richter and E. Tiemann, *Chem. Phys.*, **152**, 399, (1991).

[10] C. Amiot, J. Vergès and C. E. Fellows, *J. Chem. Phys.*, **103**, 3350, (1995).

[11] M. Masters, J. Huennekens, W. - T. Luh, L. Li, A. M. Lyyra, K. Sando, V. Zafiropulos and W. C. Stwalley, *J. Chem. Phys.*, **92**, 5801, (1990).

[12] S. Kasahara, M. Baba and H. Katô, *J. Chem. Phys.*, **94**, 7713, (1991).

[13] K. Ishikawa, N. Mukai and M. Tanimura, *J. Chem. Phys.*, **101**, 876, (1994).

[14] C. E. Fellows, *J. Chem. Phys.*, **94**, 5855, (1991).

[15] T. Gustavsson, C. Amiot and J. Vergès, *Mol. Phys.*, **64**, 279, (1998).

[16] M. Rafi, K. Ahmad, I. A. Khan, M. A. Baig and Z. Iqbal, *J. Phys. B*, **26**, 1631, (1993).

[17] K. Hussein, C. Effantin, J. D'Incan, J. Vergès and R. F. Barrow, *Chem. Phys. Lett.*, **124**, 105, (1986).

[18] M. Ligare, Z. Wu, N. D. Bhaskar and W. Happer, *J. Chem. Phys.*, **76**, 3480, (1982).

[19] F. Martin, S. Churassy, R. Bacis, R. W. Field and J. Vergès, *J. Chem. Phys.*, **79**, 3725, (1983).

[20] J. W. Tromp and R. J. Le Roy, *J. Mol. Spectrosc.*, **109**, 352, (1985).

[21] J. G. Ashmore and J. Tellinghuisen, *J. Mol. Spectrosc.*, **119**, 68, (1986).

[22] D. R. T. Appadoo, R. J. Le Roy, P. F. Bernath, S. Gerstenkorn, P. Luc, J. Vergès, J. Sinzelle, J. Chevillard and Y. D'Aignaux, *J. Chem. Phys.*, **104**, 903, (1996).

[23] C. M. Western, T. J. Slotterback, J. R. Johnson, D. W. Pratt and K. C. Janda, *J. Chem. Phys.*, **98**, 1826, (1993).

[24] *for example*, J. S. Pilgrim, C. S. Yeh, K. R. Berry and M. A. Duncan, *J. Chem. Phys.*, **100**, 7945, (1994).

[25] *for example*, S. I. Panov, J. M. Williamson and T. A. Miller, *J. Chem. Phys.*, **102**, 7359, (1995).

[26] N. Bjerre and S. R. Keiding, *Phys. Rev. Lett.*, **56**, 1459, (1986).

[27] A. Carrington, A. M. Shaw and S. M. Taylor, *J. Chem. Soc., Faraday Trans.*, **91**, 3725, (1995); A. Carrington, *Science*, **274**, 1327, (1996).

[28] A. Carrington, C. A. Leach, R. E. Moss, T. C. Steimle, M. R. Viant and Y. D. West, *J. Chem. Soc., Faraday Trans.*, **89**, 603, (1993).

[29] A. Carrington, I. R. McNab and C. A. Montgomerie, *Chem. Phys. Lett.*, **160**, 237, (1989); A. Carrington, C. A. Leach and M. R. Viant, *Chem. Phys. Lett.*, **206**, 77, (1993).

[30] R. E. Moss, *Mol. Phys.*, **80**, 1541, (1993); R. E. Moss, *J. Chem. Soc., Faraday Trans.*, **89**, 3851, (1993).

[31] A. Carrington, C. A. Leach, A. J. Marr, R. E. Moss, C. H. Pyne and T. C. Steimle, *J. Chem. Phys.*, **98**, 5290, (1993).

[32] A. Carrington, D. I. Gammie, A. M. Shaw and S. M. Taylor, *J. Chem. Soc., Faraday Trans.*, **91**, 1887, (1995).

[33] A. Carrington, C. H. Pyne and P. J. Knowles, *J. Chem. Phys.*, **102**, 5979, (1995).

[34] A. Carrington, C. A. Leach, A. J. Marr, A. M. Shaw, M. R. Viant, J. M. Hutson and M. M. Law, *J. Chem. Phys.*, **102**, 2379, (1995).

[35] A. Carrington, C. H. Pyne, A. M. Shaw, S. M. Taylor, J. M. Hutson and M. M. Law, *J. Chem. Phys.*, **105**, 8602, (1996).

[36] A. Carrington, D. I. Gammie, A. M. Shaw and S. M. Taylor, *Chem. Phys. Lett.*, **262**, 598, (1996).

[37] D. I. Gammie, Ph.D. Thesis, University of Southampton, (1999).

[38] A. Carrington, D. I. Gammie, A. M. Shaw, S. M. Taylor and J. M. Hutson, *Chem. Phys. Lett.*, **260**, 395, (1996); D. I. Gammie, Ph.D. Thesis, University of Southampton, (1999).

[39] R. A. Aziz, W. J. Meath and A. R. Allnatt, *Chem. Phys.*, **78**, 295, (1983).

[40] P. J. Knowles, *Private communication I*, (1995).

[41] R. J. Le Roy, University of Waterloo, Chem. Phys. Res. Rept. CP110 (1978).

[42] A. Carrington, *unpublished work.*

[43] A. Carrington, A. M. Shaw and S. M. Taylor, *Chem. Phys. Lett.*, **241**, 611, (1995).

[44] W. H. Wing, G. A. Ruff, W. E. Lamb and J. J. Spezski, *Phys. Rev. Lett.*, **36**, 1488, (1976).

[45] A. Carrington and P. J. Sarre, *Mol. Phys.*, **33**, 1495, (1977); A. Carrington, D. R. J. Milverton and P. J. Sarre, *Mol. Phys.*, **35**, 1505, (1978).

[46] A. Carrington, J. Buttenshaw and P. G. Roberts, *Mol. Phys.*, **38**, 1711, (1979).

[47] J. R. Hiskes, *Bull. Am. Phys. Soc.*, **5**, 340 (1960); J. R. Hiskes, *Phys. Rev.*, **122**, 1207 (1961).

[48] A. C. Riviere and D. R. Sweetman, *Phys. Rev. Lett.*, **5**, 560 (1960).

[49] A. Carrington, I. R. McNab and C. A. Montgomerie, *Chem. Phys. Lett.*, **151**, 258, (1988).

[50] F. Hund, *Z. Phys.*, **36**, 657, (1926).

[51] R. S. Mulliken, *Rev. Mod. Phys.*, **2**, 60, (1930).

[52] H. Lefebvre-Brion, *J. Chem. Phys.*, **93**, 5898, (1990).

[53] G. Herzberg. *Spectra of Diatomic Molecules*. Van Nostrand, New York, (1950).

[54] R. N. Zare. *Angular Momentum*. Wiley-Interscience, (1988).

[55] J. T. Hougen. The Calculation of Rotational Energy Levels and Rotational Intensities in Diatomic Molecules. N. B. S. Monograph 115, Washington DC, (1970).

[56] L. Veseth, *J. Phys. B.*, **6**, 1473, (1973).

[57] *for a detailed discussion of microwave waveguide and modes*, see J. A. Seeger. *Microwave Theory, Components and Devices*, page 51. Prentice-Hall, (1986).

[58] N. F. Ramsey. *Molecular Beams*, pages 118-120. Oxford Univ. Press, Oxford, (1956).

[59] A. J. Marr, Ph.D. Thesis, University of Southampton, (1994).

[60] E. Zamir, D. L. Huestis, D. C. Lorents and H. H. Nakano, in: *Electronic Transition Lasers II*, ed. L. E. Wilson, S. N. Suchard and J. I. Steinfeld. MIT, Cambridge, Mass., (1977).

[61] E. A. Mason and J. T. Vanderslice, *J. Chem. Phys.*, **30**, 599, (1959).

[62] M. S. B. Munson, J. L. Franklin and F. H. Field, *J. Phys. Chem.*, **67**, 1542, (1963).

[63] P. Kebarle, R. M. Haynes and S. K. Searles, *J. Chem. Phys.*, **47**, 1684, (1967).

[64] M. A. Biondi, *Phys. Rev.*, **129**, 1181, (1963).

[65] T. R. Connor and M. A. Biondi, *Phys. Rev.*, **140**, A778, (1965).

[66] L. Frommhold and M. A. Biondi, *Phys. Rev.*, **185**, 244, (1969).

[67] R. Ciurylo, A. Bielski, J. Domyslawska, J. Szudy and R. S. Trawinski, *J. Phys. B.*, **27**, 4181, (1994).

[68] G. Ramos, J. W. Sheldon, K. A. Hardy and J. R. Peterson, *Phys. Rev. A*, **56**, 1913, (1997).

[69] H. U. Mittman and H. P. Weise, *Z. Naturforsch. A.*, **29**, 400, (1974).

[70] L. C. Lee and G. P. Smith, *Phys. Rev. A*, **19**, 2329, (1979).

[71] W. R. Wadt, *J. Chem. Phys.*, **73**, 3915, (1980).

[72] D. J. Trevor, J. E. Pollard, W. D. Brewer, S. H. Southworth, C. M. Truesdale, D. A. Shirley and Y. T. Lee, *J. Chem. Phys.*, **80**, 6083, (1984).

[73] L. Broström, M. Larsson, S. Mannervik, R. T. Short and D. Sonnek, *J. Chem. Soc. Faraday Trans.*, **87**, 797, (1991).

[74] R. I. Hall, Y. Lu, Y. Morioka, T. Matsui, T. Tanaka, H. Yoshii, T. Hayaishi and K. Ito, *J. Phys. B*, **28**, 2435, (1995).

[75] S. B. Kim, D. J. Kane and J. G. Eden, *Phys. Rev. Lett.*, **68**, 1311, (1992).

[76] T. L. Gilbert and A. C. Wahl, *J. Chem. Phys.*, **55**, 5247, (1971).

[77] J. S. Cohen and B. Schneider, *J. Chem. Phys.*, **61**, 3230, (1974).

[78] H. H. Michels, R. H. Hobbs and L. A. Wright, *J. Chem. Phys.*, **69**, 5151, (1978).

[79] G. Frenking, W. Koch, D. Cremer, J. Gauss and J. F. Liebman, *J. Phys. Chem.*, **93**, 3410, (1989).

[80] G. E. López, *J. Comput. Chem.*, **16**, 758, (1995).

[81] J. Mášik, J. Urban, P. Mach and I. Hubac, *Int. J. Quant. Chem.*, **63**, 333, (1997).

[82] E. C. M. Chen, J. G. Dojahn and W. E. Wentworth, *J. Phys. Chem. A*, **101**, 3088, (1997).

[83] F. Y. Naumkin and D. J. Wales, *Mol. Phys.*, **93**, 633, (1998).

[84] C. E. Moore, Circ. 467, Natl. Bur. Stand. (U.S.), (1949).

[85] A. Carrington, D. I. Gammie, J. C. Page, A. M. Shaw and S. M. Taylor, *Phys. Chem. Chem. Phys.*, **1**, 29, (1999).

[86] K. Tang and J. P Toennies, *J. Chem. Phys.*, **80**, 3726, (1984).

[87] D. R. Lide, editor. *CRC Handbook of Physics and Chemistry*. CRC Press, 75th edition, (1994).

[88] J. M. Standard and P. R. Certain, *J. Chem. Phys.*, **83**, 3002, (1985).

[89] J. O. Hirschfleder, C. F. Curtiss and R. B. Bird. *Molecular Theory of Liquids and Gases*. Wiley, New York and London, (1954).

[90] E. S. Chang and H. Sakai, *J. Phys. B*, **15**, L649, (1982).

[91] A. J. Thakkar and V. H. Smith, Jr., *J. Phys. B*, **7**, L321, (1974).

[92] J. M. Hutson. BOUND computer program, version 5, distributed by Collaborative Computational Project No. 6 of the UK Engineering and Physical Sciences Research Council, 1993.

[93] M. M. Law and J. M. Hutson, *Comp. Phys. Commun.*, **102**, 252, (1997).

[94] M. Medved, P. W. Fowler and J. M. Hutson, *Mol. Phys.*, **98**, 453, (2000).

[95] M. Meuwly and J. M. Hutson, *J. Chem. Phys.*, **110**, 8338, (1999).

[96] R. G. Keesee and A. W. Castleman Jr., *Phys. Chem. Ref. Data*, **15**, 1011, (1986).

[97] K. Hiraoka and T. Mori, *J. Chem. Phys.*, **90**, 7143, (1989).

[98] *for example*, H. Haberland, *Surface Sci.*, **156**, 305, (1985).

[99] W. R. Wadt, *App. Phys. Letters*, **38**, 1030, (1981).

[100] H.-U. Böhmer and S. D. Peyerimhoff, *Z. Physik D.*, **3**, 195, (1986).

[101] J. Heßlich and P. J. Kuntz, *Z. Physik D*, **2**, 251, (1986).

[102] P. J. Kuntz and J. Valldorf, *Z. Physik. D*, **8**, 195, (1988).

[103] T. Ikegami, T. Kondow and S. Iwata, *J. Chem. Phys.*, **98**, 3038, (1993).

[104] N. E. Levinger, D. Ray, M. L. Alexander and W. C. Lineberger, *J. Chem. Phys.*, **89**, 5654, (1988).

[105] G. Ganteför, G. Bröker, E. Holub-Krappe and A. Ding, *J. Chem. Phys.*, **91**, 7972, (1989).

[106] Z. Y. Chen, C. R. Albertoni, M. Hasegawa, R. Kuhn and A. W. Castleman Jr., *J. Chem. Phys.*, **91**, 4019, (1989).

[107] I. A. Harris, R. S. Kidwell and J. A. Northby, *Phys. Rev. Lett.*, **53**, 2390, (1984).

[108] H. Haberland, B. von Issendorff, T. Kolar, H. Kornmeier, C. Ludewigt and A. Risch, *Phys. Rev. Lett.*, **67**, 3290, (1991).

[109] M. J. DeLuca and M. A. Johnson, *Chem. Phys. Lett.*, **162**, 445, (1989).

[110] *for example*, J. T. Moseley, R. P. Saxon, B. A. Huber, P. C. Cosby, R. Abouaf and M. Tadjeddine, *J. Chem. Phys.*, **67**, 1659, (1977).

[111] M. T. Bowers, W. E. Palke, K. Robins, C. Roehl and S. Walsh, *Chem. Phys. Lett.*, **180**, 235, (1991).

[112] J. T. Snodgrass, C. M. Roehl and M. T. Bowers, *Chem. Phys. Lett.*, **159**, 10, (1989).

[113] C. A. Woodward, J. E. Upham, A. J. Stace and J. N. Murrell, *J. Chem. Phys.*, **91**, 7612, (1989).

[114] P. J. Knowles, *Private communication II*, (1995).

[115] N. L. Doltsinis and P. J. Knowles, *Mol. Phys.*, **94**, 981, (1998).

[116] N. L. Doltsinis, P. J. Knowles and F. Y. Naumkin, *Mol. Phys.*, **96**, 749, (1999).

[117] D. C. Lorents, R. E. Olson and G. M. Conklin, *Chem. Phys. Lett.*, **20**, 589, (1972).

[118] C. Y. Ng, D. J. Trevor, B. H. Mahan and Y. T. Lee, *J. Chem. Phys.*, **66**, 446, (1977).

[119] P. M. Dehmer and J. L. Dehmer, *J. Chem. Phys.*, **69**, 125, (1978).

[120] K. Norwood, J. H. Guo and C. Y. Ng, *J. Chem. Phys.*, **90**, 2995, (1989).

[121] T. Pradeep, B. Niu and D. A. Shirley, *J. Chem. Phys.*, **98**, 5269, (1993).

[122] W. J. Stevens, M. Gardner, A. Karo and P. Julienne, *J. Chem. Phys.*, **67**, 2860, (1977).

[123] W. R. Wadt, *J. Chem. Phys.*, **68**, 402, (1978).

[124] B. J. Whitaker, C. A. Woodward, P. J. Knowles and A. J. Stace, *J. Chem. Phys.*, **93**, 376, (1990).

[125] A. van Deursen and J. Reuss, *Intern. J. Mass. Spectrom. Ion. Phys.*, **23**, 109, (1977).

[126] U. Buck and H. Meyer, *Surface Sci.*, **156**, 275, (1985).

[127] J. B. Anderson, in: *Gas dynamics, Molecular beams and low density gas dynamics*, Vol. 4, ed. P. P. Wegener. Dekker, New York, (1974) page 1.

[128] O. F. Hagena and W. Obert, *J. Chem. Phys.*, **56**, 1793, (1972).

[129] U. Buck, H. Meyer and H. Pauly, in: *Flow of real fluids*, Vol. 235, ed. G. E. A. Meier and F. Obermeier. Springer Lecture Notes in Physics, Springer, Berlin, (1985) page 170.

[130] E. L. Knuth, *J. Chem. Phys.*, **66**, 3515, (1977).

[131] H. D. Meyer, *Max-Planck-Institut für Strömungsforschung*. Internal Report 5, Göttingen (1978).

[132] O. F. Hagena, in: *Gas dynamics, Molecular beams and low density gas dynamics*, Vol. 4, ed. P. P. Wegener. Dekker, New York, (1974) page 129.

[133] O. F. Hagena, *Surface Science*, **106**, 101, (1981); O. F. Hagena and W. Obert, *J. Chem. Phys.*, **56**, 1793, (1972).

[134] M. Kappes and S. Leutwyler in: *Atomic and molecular beam methods*, Vol. 1, ed. G. Scoles. Oxford University Press, (1988) Chapter 15.

[135] T. D. Märk, *Intern. J. Mass. Spectrom. Ion Processes*, **79**, 1, (1987).

[136] U. Buck and H. Meyer, *J. Chem. Phys.*, **84**, 4854, (1986).

[137] U. Buck and H. Meyer, *Phys. Rev. Lett.*, **52**, 109, (1984).

[138] C. E. Klots, *J. Chem. Phys.*, **83**, 5854, (1985).

[139] C. E. Klots, *J. Phys. Chem.*, **92**, 5864, (1988).

[140] P. Scheier and T. D. Märk, *Phys. Rev. Lett.*, **59**, 1813, (1987).

[141] *A. J. Stace*, J. Chem. Phys., *93, 6502, (1990).*

[142] H. P. Godfried and I. F. Silvera, *Phys. Rev. A*, **27**, 3008, (1983).

[143] C. A. Woodward, B. J. Whitaker, P. J. Knowles and A. J. Stace, *J. Chem. Phys.*, **96**, 366 6, (1992).

[144] P. G. Lethbridge, C. A. Woodward, R. Hallett, J. E. Upham and A. J. Stace, *J. Phys. Chem.*, **93**, 5328, (1989).

[145] W. H. Press, S. A. Teukolsky, W. T. Vetterling and B. P. Flannery, *Numerical Recipes in Fortran, The Art of Scientific Computing*, (2nd edition), page 644. Cambridge University Press, (1992).

[146] A. M. Shaw, (1999), *unpublished work.*

[147] W. R. Wadt, *Appl. Phys. Letters*, **38**, 1030, (1981).